

Technische Universität München  
Fakultät für Physik  
Max-Planck-Institut für Plasmaphysik (IPP)

# **Characterization of Type-I ELM Induced Filaments in the Far Scrape-Off Layer of ASDEX Upgrade**

**Andreas Schmid**

Vollständiger Abdruck der von der Fakultät für Physik  
der Technischen Universität München  
zur Erlangung des akademischen Grades eines  
Doktors der Naturwissenschaften (Dr. rer. nat.)  
genehmigten Dissertation.

Vorsitzende: Univ.-Prof. Dr. K. Krischer

Prüfer der Dissertation: 1. Hon.-Prof. Dr. S. Günter

2. Univ.-Prof. Dr. R. Gross

Die Dissertation wurde am 03.01.2008 bei der  
Technischen Universität München eingereicht und  
durch die Fakultät für Physik am 18.03.2008 angenommen.

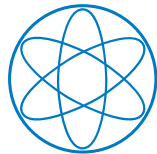


# Characterization of Type-I ELM Induced Filaments in the Far Scrape-Off Layer of ASDEX Upgrade

Dissertation  
von  
Andreas Schmid

durchgeführt am  
Max-Planck-Institut für Plasmaphysik

Physik-Department



Technische Universität München





## Parts of this dissertation were published in:

A. Schmid, A. Herrmann, H.W. Müller, and the ASDEX Upgrade Team: *Experimental observation of the radial propagation of ELM induced filaments in ASDEX Upgrade*, Plasma Physics and Controlled Fusion **50**(4), 045007, April 2008.

A. Schmid, A. Herrmann, V. Rohde, M. Maraschek, H.W. Müller, and the ASDEX Upgrade Team: *Magnetically driven filament probe*, Review of Scientific Instruments **78**(5), 053502, May 2007.

A. Schmid, A. Herrmann, A. Kirk, J. Neuhauser, S. Günter, H.W. Müller, M. Maraschek, V. Rohde, and the ASDEX Upgrade Team. *Characterization of type-I ELM induced filaments in ASDEX Upgrade*, 34th EPS Conference on Plasma Physics, Warsaw, Poland, July 2007.  
(*This contribution received a high commendation for the Itoh Project Prize 2007*)

A. Schmid, A. Herrmann, J. Neuhauser, S. Günter, T. Eich, M. Maraschek, V. Rohde, and the ASDEX Upgrade Team: *Filamentary structure of type-I ELMs*. DPG Frühjahrstagung, Augsburg, March 2007.

A. Herrmann, A. Schmid, A. Kallenbach, and the ASDEX Upgrade Team: *Filamentary heat load in ASDEX Upgrade*. ITPA SOL and Divertor Physics Meeting, Toledo, Spain, January 2008.

A. Herrmann, A. Kirk, A. Schmid, B. Koch, M. Laux, M. Maraschek, H.W. Müller, J. Neuhauser, M. Tsalas, V. Rohde, E. Wolfrum, and the ASDEX Upgrade Team: *The filamentary structure of ELMs in the scrape-off layer in ASDEX Upgrade*, 17th Plasma Surface Interactions in Controlled Fusion Devices (PSI), Hefei, China, May 2006 and Journal of Nuclear Materials **363-365** (2007), 528-533.

J. Neuhauser, V. Bobkov, G. D. Conway, R. Dux, T. Eich, M. Garcia-Munoz, A. Herrmann, L. Horton, A. Kallenbach, S. Kalvin, B. Koch, G. Kocsis, B. Kurzan, P. Lang, M. Maraschek, H. W. Müller, H. D. Murmann, R. Neu, M. Reich, V. Rohde, A. Schmid, W. Suttrop, M. Tsalas, E. Wolfrum, and the ASDEX Upgrade Team: *Structure and dynamics of spontaneous and induced ELMs on ASDEX Upgrade*, Chengdu, China, October 2006.

J. Neuhauser, V. Bobkov, G. D. Conway, R. Dux, T. Eich, M. Garcia-Munoz, A. Herrmann, L. D. Horton, A. Kallenbach, S. Kalvin, G. Kocsis, B. Kurzan, P. Lang, M. Maraschek, H. W. Müller, H. D. Murmann, R. Neu, A. G. Peeters, M. Reich, V. Rohde, A. Schmid, W. Suttrop, M. Tsalas, E. Wolfrum, and the ASDEX Upgrade Team: *Structure and dynamics of spontaneous and induced ELMs on ASDEX Upgrade*, Nuclear Fusion **48**(4), 045005, April 2008.

## Measurements have been carried out for:

B. Nold, *Turbulence at the transition from the edge to the scrape-off layer*. Diploma Thesis, Universität Stuttgart, 2007.

G. Antar, Filament Probe measurements for filament studies with ICRH, 2007.

V. Rohde, *Dust investigations in ASDEX Upgrade*. Dust in Fusion Plasmas, Satellite meeting of the 34th EPS Conference on Plasma Physics, Warsaw, Poland, July 2007.

H.W. Müller, *Parallel plasma flow and radial electric field in the scrape-off layer of ASDEX Upgrade*. 34th EPS Conference on Plasma Physics, Warsaw, Poland, July 2007.

G. Antar, *Comparing Turbulence in L and H-mode in the Scrape-off layer of the ASDEX Upgrade Tokamak*. 34th EPS Conference on Plasma Physics, Warsaw, Poland, July 2007.

F. Meo, Infrared thermography measurements for ECRH polarization tests, 2007.

L. Horton, Infrared thermography measurements of LFS startup in a tungsten covered machine, 2007.

B. Kurzan, *Thomson scattering analysis of large scale fluctuations in the ASDEX Upgrade edge*. 33rd EPS Conference on Plasma Physics, Rome, Italy, June 2006.

H.W. Müller, *Deuterium plasma flow in the scrape-off layer of ASDEX Upgrade*. 17th Plasma Surface Interactions in Controlled Fusion Devices (PSI), Hefei, China, May 2006 and Journal of Nuclear Materials **363-365** (2007), 605-610.

P. Lang, ELM triggering with biased Langmuir probes, 2006.

A. Kallenbach, *HFS/LFS limiter rampup studies in ASDEX Upgrade*. 7th ITPA SOL and Divertor Physics Meeting, Shanghai, China, January 2006.

M. Garcia-Munoz, *Fast response scintillator based detector for MHD induced energetic ion losses in ASDEX Upgrade*. PhD Thesis, LMU München, 2006.

H.W. Müller, *Plasma flow in the scrape-off layer of ASDEX Upgrade*. 32nd EPS Conference on Plasma Physics, Tarragona, Spain, June 2005.

## Abstract

Thermonuclear fusion in a magnetically confined plasma is a promising solution for the production of electricity in the future. High confinement (H-mode) operation in a tokamak type reactor is characterized by a transport barrier near the plasma edge. ELMs (edge localized modes) are periodic relaxations of this transport barrier and lead to a rapid expulsion of energy and particles from the plasma edge. The particles are released in form of coherent structures of enhanced density, which stretch along the magnetic field lines due to parallel transport. These so-called filaments propagate through the cold scrape-off layer towards the vacuum chamber walls, where they lead to a very localized deposition of energy on components that are not suited to receive high heat loads. Various models have been proposed for the radial propagation of filaments. Generally, these models are based on filament polarization due to particle drifts, and, consequently, a radial  $E \times B$  drift of the filament. The models differ with respect to the damping mechanisms and lead to opposed predictions on the scaling of the radial propagation velocity with filament size, i.e. whether bigger or smaller filaments move faster.

Therefore, this thesis focuses on the characterization of filaments and their propagation in the ASDEX Upgrade tokamak. The aim is to provide experimental measurements for understanding the filament formation process and their temporal evolution, and to provide a comprehensive database for an extrapolation to future fusion devices.

For this purpose, a new magnetically driven probe for filament measurements has been developed and installed in ASDEX Upgrade. The probe carries several Langmuir probes (electrical measurements that can give information on density and temperature), and a magnetic coil in between.

The Langmuir probes allow for measurements of the radial and poloidal/toroidal propagation of filaments as well as for measurements of filament size, density, and their radial (or temporal) evolution.

The analysis of the radial velocity shows that bigger filaments move faster, with radial velocities being in the range of a few km/s. This clearly excludes the sheath damping model, but agrees quite good with the polarization current model. This is important, as bigger filaments carry a higher energy content, and – if they move faster and thus have less time to lose their energy by parallel transport – deposit more heat on the plasma facing components. Poloidal rotation velocities have been found to be in the range of up to the pedestal rotation velocity, indicating that the filaments start off with a rotation equal to the plasma edge and then slow down on their way out.

The Langmuir measurements have allowed to measure size and density of filaments, as well as their temporal evolution: Filaments broaden with time due to diffusion, and lose particles parallel to the field lines with a rate similar to a free flow of particles along the field line. An extrapolation shows that they are formed with densities close to separatrix densities, indicating that filaments are formed near the separatrix.

The magnetic coil on the filament probe allows for measurements of currents in the filaments. A set of 7 coils, measuring 3 field components at different positions along the filament, has been used to measure the magnetic signature during an ELM.

The aim was, on the one hand, to study which role filaments play for the magnetic structure, and on the other hand if the parallel currents predicted by the sheath damped model could be verified.

Numerical calculations, based on information on filament velocity and size from the Langmuir measurements, have been set up to investigate if the magnetic signature dur-

ing an ELM can be explained by filaments. It has been found that the magnetic signal is reproduced by a bi-directional current distribution (which would be in agreement with the sheath damped model), but the required currents exceed the possible filament currents by at least one order of magnitude. No good temporal correlation between the density signal on the Langmuir measurements and the magnetic signal could be shown. Instead, it has been found that the magnetic signature is reproduced by mode structures which rotate in the pedestal region. These mode structures might be remnants of the peeling-ballooning modes, which lead to the splitting-off of filaments.

Infrared thermography has been used to investigate energy deposition on plasma facing components. Filament temperatures have been derived and the corresponding heat transport mechanisms have been studied. The energy content of a filament has been found to be much smaller than the total ELM energy loss, which might indicate that the filaments are, in a first stage, still connected to the core plasma and act as a conduit for losses from the core plasma to the scrape off layer.

The fraction of energy that is deposited in the divertor close to the separatrix depends on the time at which the filament detaches from the core plasma: In the initial stage, when the filament is still attached, the deposited energy can exceed the energy content of the filament by far. The filaments are expected to lose most of their energy in the very first period right after their formation, when fast (and thus energetic) particles are lost preferentially. As soon as the filament is detached, only its energy content remains to be deposited on the wall structures, with bigger filaments leading to higher energy deposition to the wall.



# Contents

<b>1</b>	<b>Introduction</b>	<b>1</b>
1.1	Motivation . . . . .	1
1.2	Magnetic Confinement . . . . .	2
1.3	Outline . . . . .	4
<b>2</b>	<b>Edge Localized Modes and Filaments</b>	<b>5</b>
2.1	Edge Localized Modes . . . . .	5
2.1.1	Overview on ELMs . . . . .	5
2.1.2	ELM Cycle . . . . .	7
2.1.3	H-mode Edge Profile . . . . .	9
2.2	Filaments . . . . .	10
2.2.1	Detection and Wall Impact of Filaments . . . . .	10
2.2.2	Filaments as Field Aligned Structures . . . . .	12
2.2.3	Important Filament Properties . . . . .	15
2.3	Theoretical Approach . . . . .	16
2.3.1	Linear Models . . . . .	18
2.3.2	Nonlinear Models . . . . .	18
<b>3</b>	<b>Radial Motion of Filaments</b>	<b>21</b>
3.1	Vertical Filament Polarization and Radial $\mathbf{E} \times \mathbf{B}$ Drift . . . . .	21
3.2	Parallel Currents and Sheath Damping . . . . .	23
3.2.1	Dependence on Filament Density . . . . .	26
3.2.2	Three-Field Braginskii Model . . . . .	27
3.2.3	Fragmentation of Filaments . . . . .	29
3.3	Diamagnetic Current . . . . .	30
<b>4</b>	<b>Experimental Setup</b>	<b>33</b>
4.1	Magnetically Driven Filament Probe . . . . .	33
4.1.1	Setup of the Filament Probe . . . . .	34
4.1.2	Magnetic Drive . . . . .	35
4.1.3	Heat Production of the Magnetic Drive . . . . .	37
4.1.4	Test of the Magnetic Drive . . . . .	39
4.1.5	Probe Head . . . . .	40
4.2	Midplane Manipulator . . . . .	43
4.3	Infrared Thermography . . . . .	45

<b>5</b>	<b>Filament Motion Measurements</b>	<b>49</b>
5.1	Radial Motion . . . . .	50
5.1.1	Diagnostic Setup . . . . .	50
5.1.2	Measuring Method . . . . .	51
5.1.3	Raw Data and Data Conversion . . . . .	53
5.1.4	Interpretation . . . . .	57
5.1.5	Evolution of Size and Density . . . . .	59
5.1.6	Radial Acceleration . . . . .	62
5.1.7	Summary on the Radial Propagation Velocity . . . . .	63
5.2	Filament Rotation . . . . .	64
5.2.1	Pin Mapping . . . . .	64
5.2.2	Data Evaluation . . . . .	66
5.3	On the Interpretation of Velocity Measurements . . . . .	69
5.4	Propagation in Limiter Shadowed Regions . . . . .	71
<b>6</b>	<b>Magnetic Signature of ELMs</b>	<b>75</b>
6.1	Numerical Simulation . . . . .	75
6.1.1	Technical Properties . . . . .	75
6.1.2	Characterization for Uni- and Bi-Directional Current . . . . .	78
6.2	Application to Measurements . . . . .	80
6.2.1	Filament-Based Model . . . . .	80
6.2.2	Mode-Based Model . . . . .	84
<b>7</b>	<b>Temperature of Filaments</b>	<b>89</b>
7.1	Heat Flux Measurements . . . . .	89
7.2	Heat Loss Mechanisms . . . . .	91
7.3	Triple-Probe Measurements . . . . .	93
7.4	Filament Detachment . . . . .	96
<b>8</b>	<b>Summary and Outlook</b>	<b>99</b>
8.1	Current View of an ELM Crash . . . . .	100
8.2	Outlook . . . . .	101
<b>A</b>	<b>ASDEX Upgrade</b>	<b>103</b>
<b>B</b>	<b>MAST</b>	<b>107</b>
<b>C</b>	<b>Sheath Physics</b>	<b>109</b>
C.1	Floating Walls . . . . .	109
C.2	Biased Walls . . . . .	110

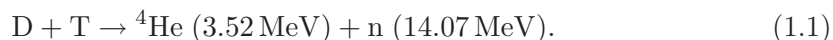
# Chapter 1

## Introduction

### 1.1 Motivation

In recent years, the link between climate change and the production of greenhouse gases by human activities became more and more evident, with a certainty of currently more than 90% [1]. Carbon dioxide is the most important anthropogenic greenhouse gas and is mainly produced by the use of fossil fuel, e.g. for the generation of electricity. Several steps have to be carried out in order to reduce the emission of greenhouse gases: In addition to saving energy and improving energy efficiency, effective mechanisms for a CO<sub>2</sub>-free production of electricity have to be developed.

In principle, nuclear reactions provide a CO<sub>2</sub>-free source of energy. The conversion of nuclei towards iron releases binding energy, namely by joining light nuclei to form a heavier nucleus (nuclear fusion) or by splitting a heavy nucleus into lighter nuclei (nuclear fission). An example for a nuclear fusion reaction is the fusion of deuterium and tritium



Deuterium and tritium are hydrogen isotopes and can be separated rather easily because of their high mass ratio. Deuterium is a naturally occurring hydrogen isotope with a natural abundance of 0.015% and thus is universally available. Tritium is an unstable isotope with a half-life time of 12 years and can be bred from lithium using the fusion-born fast neutrons:



The D-T-reaction has certain advantages over nuclear fission reactions: the source nuclei lithium and deuterium are practically abundant and the reaction does not bear the hazard of prompt critical chain reactions because the nuclei have to overcome the Coulomb barrier until the nuclear force joins the two nuclei together. Nuclear fusion reactions cannot take place if the nuclei do not have sufficient kinetic energy to overcome or to tunnel through the Coulomb barrier. Even at high energies, the interaction is dominated by Coulomb collisions that happen far more often than fusion reactions. This is why an accelerator driven fusion reaction (beam-beam or beam-target) will not be suitable for an efficient production of electric energy. In a thermal equilibrium, where the nuclei have their kinetic energy in form of a temperature, the Coulomb collisions will not result in a net loss of energy. The fusion rate for the thermonuclear D-T fusion

(1.1) reaches a maximum at  $T \approx 15 \text{ keV}^1$ . At these temperatures, atoms have already dissolved into ions and electrons and form a so-called plasma, often referred to as the fourth state of matter.

The aim is to operate a fusion reactor in an ignited state, which means that the fusion-born  $^4\text{He}$  particles serve to sustain the plasma at the optimum temperature so that no external heating is needed. The energy gain is given by

$$Q = \frac{P_{fus}}{P_{ext}}, \quad (1.4)$$

where  $P_{fus}$  is the fusion power and  $P_{ext}$  the externally applied power, and would become infinity in the ignited state.

$Q$  is the crucial parameter for a fusion reactor and has to be maximised. For the total efficiency of a fusion reactor,  $Q$  has to be multiplied with the efficiency of the conversion from neutron energy into electric energy, so that  $Q \approx 50$  has to be achieved in a nuclear power plant [2]. The Lawson criterion

$$nT\tau > 3 \cdot 10^{21} \text{ m}^{-3}\text{keVs}, \quad (1.5)$$

with plasma density  $n$ , temperature  $T$ , and confinement time  $\tau$  describes the parameter region required for ignition of a D-T reaction and can be derived from energy balance considerations. The temperature, however, is constrained by the fusion rate, which has its maximum in the temperature range of  $10 - 20 \text{ keV}$ . In inertial fusion [3], the plasma is confined by inertia, which gives small confinement time at high densities, whereas in magnetic fusion [4], the plasma is confined by magnetic fields, which yields a confinement time in the order of several seconds at low densities of  $10^{20} \text{ m}^{-3}$ .

## 1.2 Magnetic Confinement

A plasma consists of charged particles and hence can be confined by magnetic fields. In ideal magnetohydrodynamics (MHD) [5], a fluid description of the plasma, the stationary force balance is

$$\nabla p = \mathbf{j} \times \mathbf{B}. \quad (1.6)$$

This means, for example, that a cylindrical plasma column can be confined by an axial magnetic field. Bending the cylinder to a torus prevents losses at the ends, but induces radial particle drifts, which can be short-circuited with an additional poloidal field. The superposition of toroidal and poloidal magnetic field leads to a helical field with wound field lines. These wound field lines form a set of nested, toroidal flux surfaces. The last closed flux surface, the so-called separatrix, separates the magnetically confined plasma from the so-called scrape-off layer (SOL) plasma, where the field lines are terminated by material limiters.

A helically wound magnetic field can be generated either by external coils alone (stellarator), or by poloidal coils generating a toroidal magnetic field and a toroidal plasma current generating a poloidal magnetic field (tokamak). The tokamak requires an additional vertical field to hold the plasma current in place against the hoop-force, which pushes the plasma current radially outwards. Fig. 1.1 shows the basic layout of a tokamak together with the external magnetic field coils. Field lines on a given flux surface

---

<sup>1</sup>1 keV  $\simeq$  11600 K

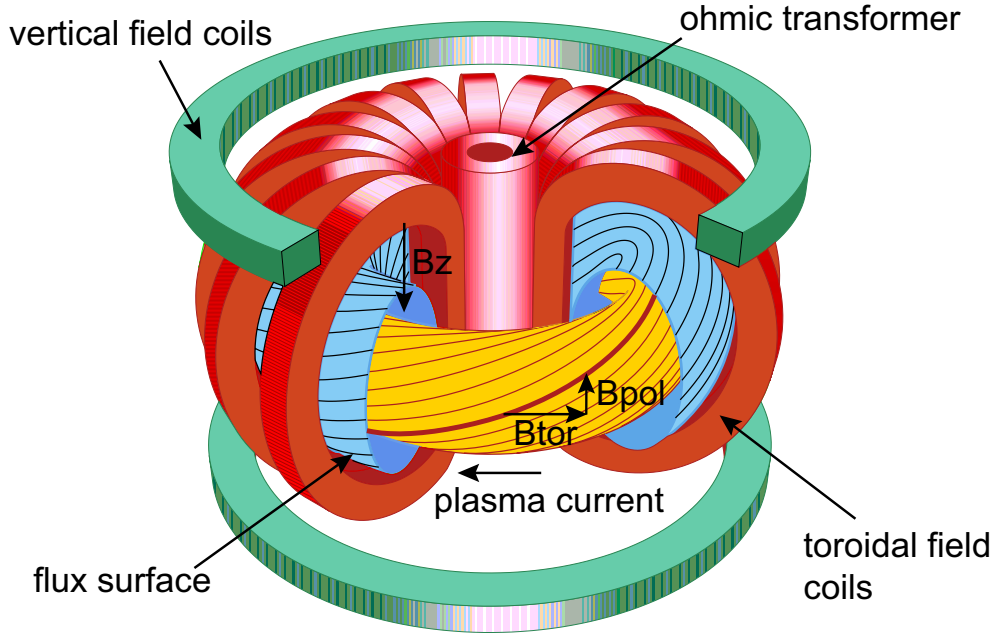


**Figure 1.1:** Schematic view of a tokamak and the 3 magnetic fields: Toroidal field, poloidal field and vertical field. The ratio of the 3 components is  $B_{tor} : B_{pol} : B_z \simeq 100 : 10 : 1$

close on themselves, if the safety factor

$$q \approx \frac{r B_{tor}}{R B_{pol}} = \frac{n}{m} \quad (1.7)$$

takes rational values, with  $m$  and  $n$  being the number of toroidal and poloidal turns, respectively.

For a given machine size, the fusion performance can only be increased by improvements in confinement. For that purpose, a diverted magnetic field configuration with 1 or 2 X-points (where the poloidal magnetic field is 0 and the field lines are essentially toroidal) is used in ASDEX Upgrade to separate the core plasma from the plasma-wall-interaction region (see appendix A for details on ASDEX Upgrade). This configuration, introduced in the ASDEX tokamak, has led to the discovery of the so-called H-mode (high confinement mode) [6, 7], in which edge turbulence is believed to be suppressed by sheared flows, which reduce the scale of turbulence and, hence, the transport across the last closed flux surface. H-mode leads to a rise of steep edge pressure gradients that enclose a density pedestal in the plasma core, and to an improvement in confinement by a factor of about 2.

Unfortunately, there is a severe drawback connected with H-mode operation: the high pressure gradients at the plasma edge give rise to edge instabilities, the so-called edge localised modes (ELMs). ELMs are repetitive instabilities that lead to a temporal loss in plasma confinement and, consequently, to a fast expulsion of energy and particles from the plasma edge. However, total plasma performance of this ELMy H-mode is still by a factor of 2 better than low confinement operation. ELMy H-mode has therefore been chosen as the standard operation scenario for ITER and is expected to deliver  $Q \simeq 10$ .

The burst-like energy release due to ELMs is of no great concern in present day machines, but extrapolation to future devices (e.g. ITER, DEMO) shows that the energy release by ELMs might easily exceed the heat load limits of divertor and first wall materials, and lead to destruction or strongly reduced lifetime of plasma facing components.

In recent years, a lot of work has been done on ELMs and their extrapolation to ITER. This has led to the discovery of so-called filamentary transport of energy and particles within ELMs. Filaments are coherent structures of enhanced density and temperature that are generated during an ELM and travel radially outwards to the plasma facing components. They provide an efficient mechanism to carry energy from the core to the wall structures and lead to a localised deposition.

Details of filament properties are presently in the focus of experimental observation. The knowledge of these quantities allows a direct comparison with theoretical models of the ELM evolution, and filamentary energy and particle transport in the SOL.

### 1.3 Outline

The aim of the work presented here is the characterization of type-I ELM induced filaments on the ASDEX Upgrade tokamak. This is of particular interest for understanding the filaments as well as for providing input for an extrapolation to ITER and other next step fusion devices.

In chapter 2, introductory remarks will be presented to give an overview on ELMs and to describe the environment that leads to the formation of filaments and influences their evolution. The common knowledge on filaments at the start of this thesis is reviewed in terms of experimental findings as well as theoretical models that describe the filament formation process.

The mechanisms that lead to the radial motion of filaments are presented in chapter 3 together with damping mechanisms that have been proposed, but which predict totally different velocity scalings.

Chapter 4 describes the experimental setup that has been developed for the characterization of filaments in ASDEX Upgrade: A magnetically driven filament probe that allows for measurements of radial and poloidal/toroidal propagation velocities and measurements of the magnetic signature of ELMs and filaments, different probe heads for a second manipulator that has been used to extend the filament probe measurements, and infrared thermography, which has been used for heat flux measurements.

In chapter 5, the measurements of radial and poloidal/toroidal dynamics of filaments are presented together with data on the size, density and radial evolution of filaments. Chapter 6 shows the measurements of the magnetic signature during ELMs, and investigates if the magnetic signature can be explained by filaments.

Chapter 7 presents heat flux measurements and calculations of filament temperatures and studies the question whether filaments are connected to the core plasma.

The results are summarized in chapter 8, and an outlook to future work with regards to filaments is presented.

## Chapter 2

# Edge Localized Modes and Filaments

### 2.1 Edge Localized Modes

#### 2.1.1 Overview on ELMs

H-mode [6, 7] is an operation regime that provides enhanced confinement and leads to the build-up of steep density, temperature and hence pressure gradients at the plasma edge by suppression of edge turbulence. These gradients give rise to specific MHD instabilities, the so-called edge localized modes (ELMs) [8, 9, 10]. ELMs expel energy and particles from the plasma edge and cause burst-like heat fluxes to the plasma facing components. The heat fluxes might easily exceed the material limits and pose a severe threat for next step fusion devices and in particular for ITER.

ELMs appear periodically and have a burst-like structure: the ELM cycle starts with a quiet phase, in which radial transport across the separatrix is small so that the high H-mode edge gradients can build up. The ELM itself happens within  $< 1$  ms, which is far less than the typical ELM cycle time, so that ELMs appear as sharp separated bursts.

A transition from L- to H-mode occurs, if the heating power exceeds a certain power threshold, e.g.

$$P_{th5} = 2.34 n^{0.67} B_{tor}^{0.62} a^{1.02} R^{0.71}, \quad (2.1)$$

where  $P_{th5}$  is the power threshold in MW,  $n$  the plasma density in  $10^{20} \text{ m}^{-3}$ ,  $B_{tor}$  the toroidal magnetic field in T, and  $a$  and  $R$  the minor and major radius in m [11]. Several scaling laws have been proposed, based on different data and parameter sets, but all of them scale with  $n$  and  $B$ . ELM-free H-mode operation will lead to a rise in density, and, consequently, to a rise in the power threshold so that the plasma drops back into L-mode (if the other parameters are not adjusted accordingly). ELMy H-mode, however, leads to stationary H-mode conditions on time scales far bigger than the ELM cycle time [8]. Up to now, no first-principles theory on ELMs has been found due to the complexity of the ELM phenomenon. Therefore, a phenomenological classification based on the ELM frequency has been introduced a decade ago after a comparison of ELM occurrences on various tokamaks [9]:

- Type-I ELMs: repetition frequency increases with  $P_{sep}$ , the energy flux through

the separatrix

$$\frac{df_{ELM}}{dP_{sep}} > 0 \quad (2.2)$$

- Type-III ELMs: repetition frequency decreases with  $P_{sep}$

$$\frac{df_{ELM}}{dP_{sep}} < 0 \quad (2.3)$$

Apart from these two types, several other ELM types have been found: compound ELMs (with a subsequent L-mode phase), dithering cycles (a series of L-H-L transitions), type-II ELMs, etc [9]. A clear distinction between the different ELM types may sometimes not be easily possible. The occurrence of magnetic precursors has also been used for the characterization of ELMs, see e.g. [12].

Typical ELM frequencies at ASDEX Upgrade are in the range of 10 – 200 Hz for type-I ELMs, and 200 Hz-2 kHz for type-III ELMs. In this thesis, we will mainly focus on type-I ELMs, as the type-I ELMy H-mode provides the highest fusion rate, even though type-I ELMs have the highest energy loss per ELM. In ASDEX Upgrade, the loss per type-I ELM is about 10 – 20 kJ, which is about 5% of the plasma stored energy  $W_{MHD}$ , and results in a power loss of about 20% of the applied heating power [13]. The resulting heat flux can reach values of up to 20 MW/m<sup>2</sup> during an ELM, compared to 5 MW/m<sup>2</sup> in between ELMs [8].

Fig. 2.1 shows a comparison of the ratio of ELM energy loss to the total plasma stored energy,  $\Delta W_{ELM}/W_{MHD}$ , and the normalized ELM frequency  $f_{ELM} \cdot \tau_E$  (with the energy confinement time  $\tau_E$ ) on ASDEX Upgrade and JET [13, 14, 15]. The data points can

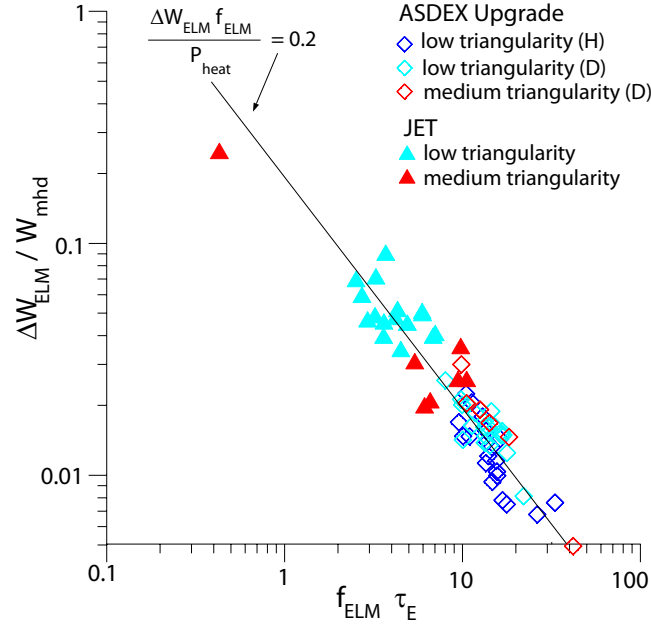


**Figure 2.1:** Dependence of the ELM size on the ELM frequency [13] for different plasma shapes on ASDEX Upgrade and JET. The ELM size is expected to increase with confinement, so that very large ELMs are expected for ITER.



be approximated by

$$\frac{\Delta W_{ELM}}{W_{MHD}} = \frac{0.2}{f_{ELM} \tau_E}. \quad (2.4)$$

i.e. the ELM transported power is constant,

$$\Delta W_{ELM} \cdot f_{ELM} = 0.2 \cdot P_{heat}, \quad (2.5)$$

It is important to note that the data points are separated along that line: JET has higher ELM losses at lower normalized ELM frequency. The ELM frequency decreases faster than the confinement time rises,  $f_{ELM} \propto \tau_E^{-1.7}$ . This predicts very large ELMs for next step fusion devices and for ITER [13, 14, 16].

For ITER, the acceptable loss per ELM has been estimated to be 5 – 10 MJ, whereas the expected ELM size could reach 13 – 22 MJ [17], which is about 10-20% of the total plasma energy ( $W_{MHD} \approx 112$  MJ). Reducing the ELM size is thus connected to a reduction in confinement, e.g. in JET, so-called minimum ELMs have been found when the recovery of the pedestal has been artificially slowed down by enhancing losses in the inter-ELM period (by fluctuations, bulk radiation, etc). A review on ELM control can be found in [18]. According to eq. (2.5), these ELM tailoring methods will always reduce confinement and thus net fusion power for given machine size. Furthermore, they add additional complexity to the fusion reactor, which will become important when the question of complexity and reliability of a fusion power plant arises.

### 2.1.2 ELM Cycle

In order to study the ELM mechanism, it is convenient to investigate the regimes in which the different ELM types occur. Fig. 2.2 shows the occurrences of different ELM

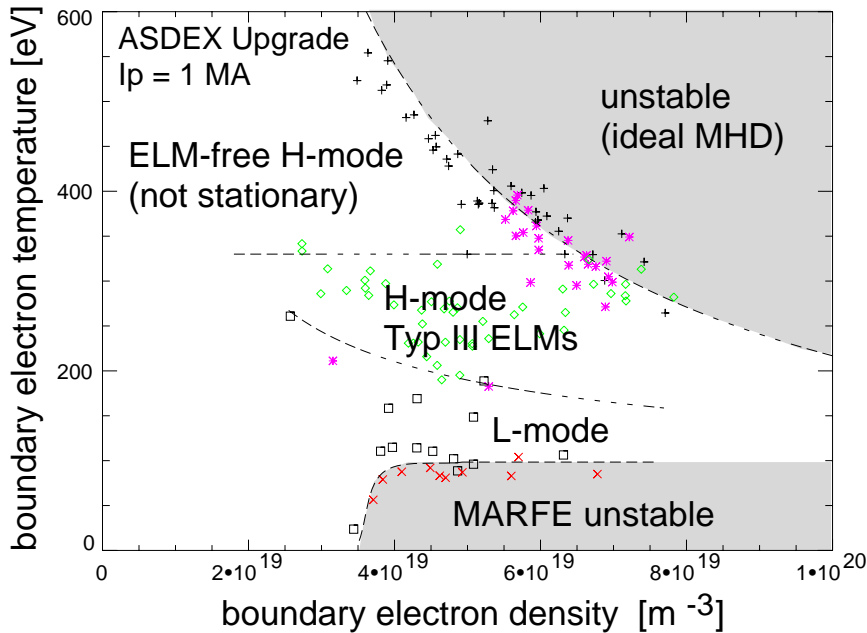


**Figure 2.2:** Edge operational diagram showing regime boundaries and experimental results of ASDEX Upgrade. From [10]

types for ASDEX Upgrade.

The ELM types separate and show clear regime boundaries: type-I ELMs appear close to the ideal ballooning limit, which clamps the pressure gradient to a critical value, [19],

$$\frac{p}{\lambda_p} = \frac{\pi^2 R B^2}{\mu_0 L_c} \quad (2.6)$$

before the ELM sets in. In this equation,  $\lambda_p$  is the length scale for the pressure gradient and  $L_c$  the connection length to the X-points. Type-III ELMs occur below a critical edge temperature (dashed line), which might point towards a resistive phenomenon. Together with consistent observations of medium toroidal mode numbers  $n$  involved in ELM precursor oscillations, this has led to an ELM model based on a coupling of current-driven peeling and pressure-driven ballooning modes [10]. Fig. 2.3 gives a schematic view of the ELM cycle: At the beginning of the ELM cycle, the pressure

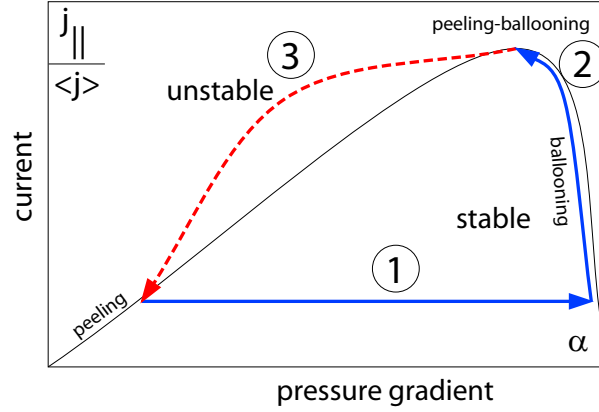


**Figure 2.3:** Type-I ELM cycle. The pressure gradient rises and (1), on the slower resistive timescale, causes the edge current  $j_{\parallel}$  to rise (2), finally triggering the ELM (3). From [10]

gradient  $\alpha$  rises. In a toroidal device, a pressure gradient drives a parallel current by neoclassical processes, the so-called bootstrap current. This current cannot build up as fast as the pressure gradient since the transport timescale is faster than the resistive time scale, so that first of all a region of stability boundary with predominant ballooning character is encountered. The slowly rising edge current finally leads to instability with strong peeling mode character and radially extended eigenmodes, which finally cause the ELM (or ELM crash). From double null discharges (i.e. discharges with 2 active X-points), one can see that the outer midplane is the primary source for the release of energy during the ELM, as virtually no power deposition can be seen on the high field side divertor plates [20].

Quantitative models in the peeling ballooning framework will be described in sec. 2.3. A general review on ELMs themselves can be found in [21].

### 2.1.3 H-mode Edge Profile

Fig. 2.4 shows typical H-mode profiles of  $T_e$ ,  $n_e$ , and  $p_e$  in the ASDEX Upgrade mid-

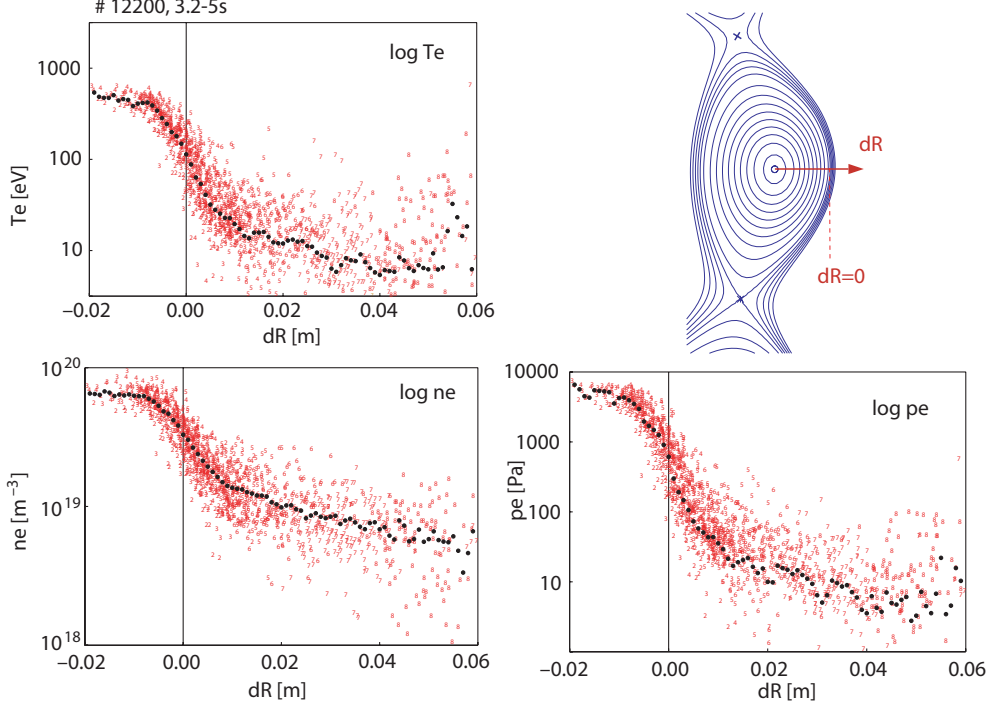


**Figure 2.4:** Typical midplane profiles during an ELMy H-mode discharge [22].  $dR = 0$  denotes the separatrix position, i.e. the border between open and closed field lines. The profiles show the four typical H-mode edge regions (radially outwards): the H-mode pedestal, the steep gradient zone around the separatrix, the hot scrape-off layer (SOL) and the cold SOL wing, where enhanced radial transport occurs.

plane from a type-I ELMy H-mode discharge. The profiles have been measured with the YAG laser Thomson scattering system, which measures  $T_e$  and  $n_e$  simultaneously. The profiles clearly show four distinctive regions of the H-mode plasma edge: the innermost part shows the outer part of the H-mode pedestal, a region of high temperature and density that spreads over the whole core plasma and determines the achievable plasma performance. Around the separatrix, which separates the closed field lines from the open field lines, is the steep gradient region. For type-I ELMy H-mode, this gradient is determined by the ideal ballooning limit (2.6). The steep gradient region evolves further into the hot SOL with increased scatter and further outside into the cold SOL wing with  $T_e < 20$  eV.

The cold SOL shows a pronounced profile flattening due to a higher ratio of radial to parallel transport (see sec. 7.2). Filamentary transport is one possible mechanism to explain the large scatter in the profiles, as the filaments are structures of enhanced density and temperature, and to explain the enhanced radial transport, as the filaments drift radially because of an  $\mathbf{E} \times \mathbf{B}$ -drift (see sec. 3). In experiments with a large gap between the separatrix and the first wall, such as the spherical tokamak MAST (see appendix B), filamentary transport has been found to reach regions up to 20 cm away from the separatrix [23].

Additional scatter in the profiles may come not only from individual filaments, but also from the stochasticity of ELMs. Standard deviations for ELM frequency, energy loss, particle loss, and pedestal temperature drop have been found to be in the order of 10-15% in JET [16]. For the following, one has to keep in mind that values derived from an individual ELM may only describe that particular ELM, but for a general description of ELMs can only provide an order of magnitude. A statistical analysis will be necessary to derive general properties of ELMs and filaments.

## 2.2 Filaments

### 2.2.1 Detection and Wall Impact of Filaments

Up to 2003, the investigation of ELMs was mainly focused on the energy deposition in the divertor, as the high heat fluxes due to type-I ELMs pose a severe threat for the divertor or at least tend to drastically reduce divertor live time [13, 24]. The rise in surface temperature due to a heat-flux  $q_h$  is

$$\Delta T(t) = \frac{2}{\sqrt{\pi \kappa \varrho c}} q_h \sqrt{t} \quad (2.7)$$

where  $\kappa$  [ $W/mK$ ] is the thermal conductivity and  $\varrho c$  is the product of density and specific heat, the critical parameter being the product of heat flux and the square root of the deposition time,  $q_h \sqrt{t}$  [13]. According to this, a longer deposition time will result in a reduced heat load for a given ELM energy loss. The extrapolation to ITER predicts an ELM energy loss of 10 – 15 MJ per ELM, which is deposited in the divertor on an area of  $5 \text{ m}^2$  in  $240 \mu\text{s}$ , resulting in values in the order of  $200 \text{ MJ/m}^2\text{s}^{0.5}$  in the divertor. Tungsten melting takes place at  $40 \text{ MJ/m}^2\text{s}^{0.5}$  and carbon ablation at  $20 \text{ MJ/m}^2\text{s}^{0.5}$ , so that the ITER predictions are at best marginally acceptable if not unacceptable [13, 25]. A review on the choice of first wall materials has been given in [26].

In addition to divertor heat load, recent studies have found that there is a non-negligible energy deposition outside the divertor during ELMs [25, 27]: the fraction of energy in the divertor accounts for only about 60% of the total ELM loss in JET and ASDEX Upgrade, whereas about 15% are transported to the wall (see fig. 2.5). The local heat load at the wall will result in surface temperatures up to the sublimation limit of carbon and cause a significant erosion of material in next step fusion devices and in ITER [29]. The occurring of losses in the outer midplane has been connected to the discovery of filamentary substructures within the ELM, which travel through the SOL and carry hot particles from the edge to the wall. An open question remains in this context, if single filaments can already cause significant erosion, or if this requires the impact of several filaments.

Filaments have first been found by infrared thermography in the upper divertor of ASDEX Upgrade, where they show a spiral-like deposition pattern [20]. Afterwards, they have been shown with various diagnostics, for example with Langmuir probes [30, 31], where they appear as prominent spikes in the ion saturation current. Fig. 2.6 shows such Langmuir time traces from probes at the outer midplane of ASDEX Upgrade, together with visible  $D_\alpha$  emission caused by de-excitation of neutrals in the SOL, the heat flux to the midplane probe, and the magnetic signature during the ELM at the midplane probe.

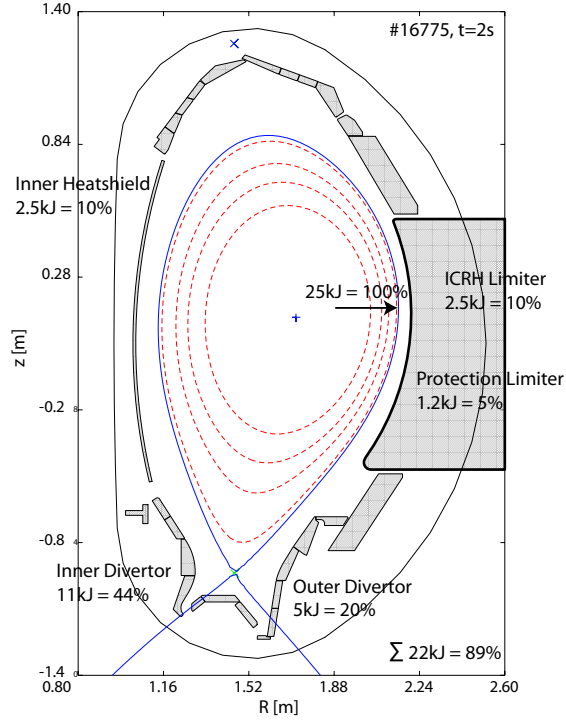


**Figure 2.5:** Distribution of the energy deposition in the ASDEX Upgrade vessel during type-I ELMs. Localized deposition of the radially transported energy threatens plasma facing components that are not designed to withstand high heat loads. From [28].

Filaments have also been shown by infrared thermography on the low field side protection limiters [27], and as two-dimensional structures with the vertical Thomson scattering system [32]. Filaments have even been found in a recent analysis of data from the ASDEX tokamak [33].

The MAST tokamak is particularly suited for filament imaging due to a large plasma-wall distance. Its large cylindric vessel allows for a large field of view for both visible and infrared cameras [34, 35]. See appendix B for details on the MAST tokamak. In addition, the edge parameters (density, temperature) in MAST are so that a filament travelling through the SOL produces a high level of  $D_\alpha$  radiation, which can easily be detected by visible imaging. Because of the higher edge temperatures and the lower edge densities in ASDEX Upgrade, filaments become visible only when they touch the wall. A radial Thomson scattering system in MAST gives radial density profiles as filaments move past the line of sight [35]. With Langmuir probes, filaments have been found at distances up to 20 cm from the plasma edge with a density in the order of 10% of their peak value near the separatrix [35]. This means that the filaments lose energy during their journey through the SOL by transport parallel to the field lines. First models have been developed in order to describe the competition between parallel and radial transport in a filament, resulting in filaments being represented by a Gaussian wave packet [36, 37]. The filaments seem to broaden with time, to travel radially outwards and to decay exponentially. The filament is predicted to cool rapidly since the fastest particles are removed preferentially, quickly reducing the average energy per particle.

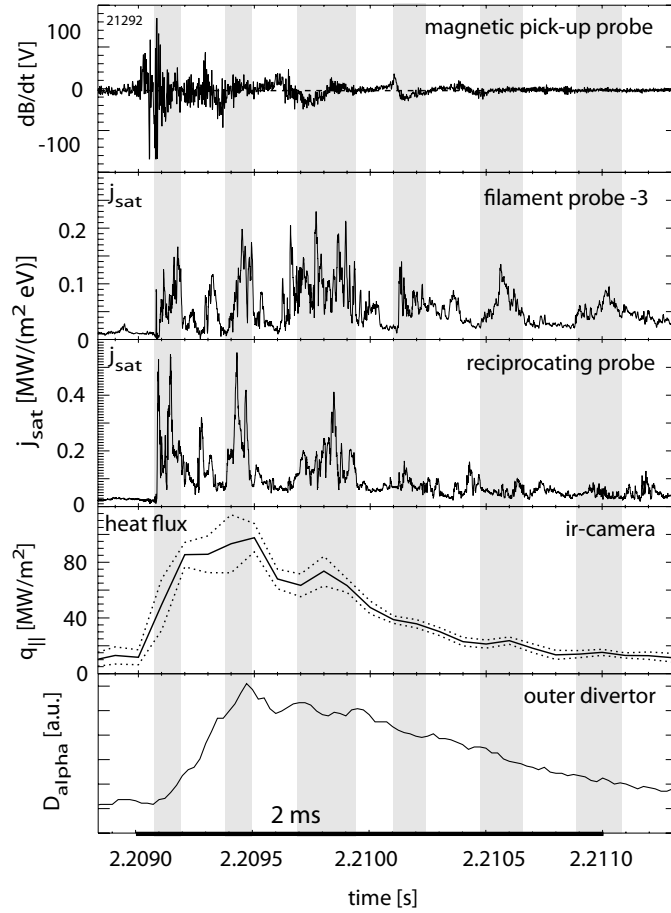


**Figure 2.6:** Visible  $D_\alpha$  emission during an ELM compared with fast Langmuir probe measurements in the outer midplane, fast magnetic measurements, and the heat flux to the outer midplane probe on ASDEX Upgrade (from top to bottom). Filaments appear as prominent peaks in the ion saturation current and the heat flux.

However, these calculations have been carried out in the filament frame of reference, neglecting the motion of the filament itself.

In recent years, studies have been carried out on the role of filamentary structures in inter-ELM and L-mode turbulence [38]. In [39], it has been found that inter-ELM filaments have a structure similar to ELM-induced filaments, but do typically not detach from the plasma.

### 2.2.2 Filaments as Field Aligned Structures

It has already been described above that filaments appear as sharp bursts on local measurements such as Langmuir probes,  $D_\alpha$  lines of sight, etc. This means, that filaments are localized structures of enhanced density and temperature that move past the probe or the line of sight of the diagnostic. They are stretched along the magnetic field lines due to high parallel transport. 2D diagnostics such as visible imaging and infrared thermography ultimately reveal that filaments are field aligned structures: infrared thermography shows the interaction of the filament with the wall, visible imaging shows the re-excitation of neutrals in the colder edge region. Fig. 2.7 shows two images

during type-I ELMs from visible imaging on MAST (right), and from the interaction with the low field side protection limiters as seen by infrared thermography on ASDEX Upgrade (left).

The corresponding 3D structure is shown schematically in fig. 2.8, based on the

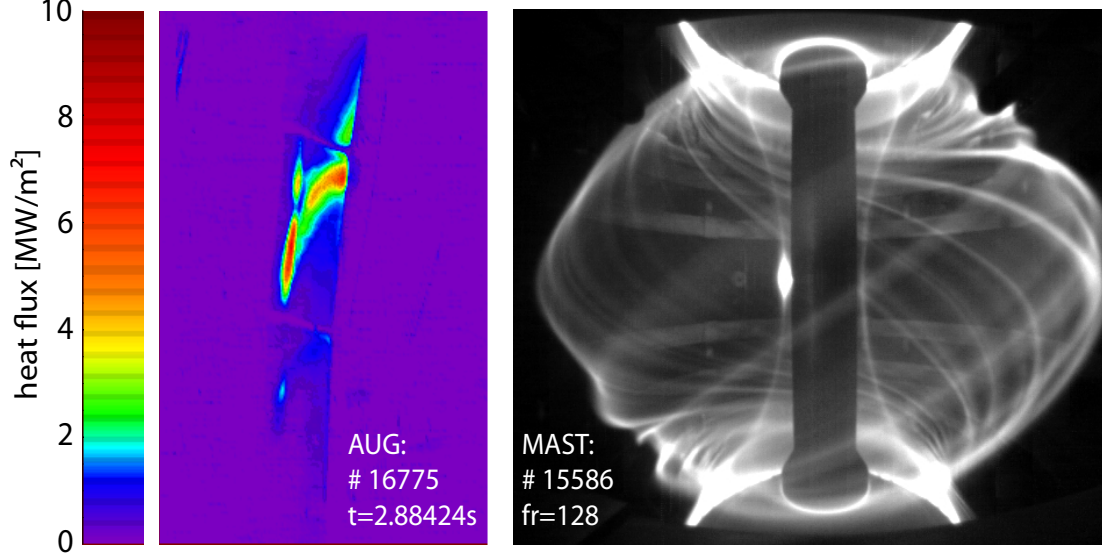


**Figure 2.7:** Fast 2D visible imaging on MAST (right) and interaction of a filament with a low field side limiter on ASDEX Upgrade (left). Filaments are clearly visible on the visible imaging if the plasma rotation velocity is sufficiently slow ( $v_{ped} < 10$  km/s). At higher pedestal rotation velocities, the filaments merge together due to finite exposure time, which provides the first evidence that filaments rotate with the plasma edge. Filaments always follow the field lines, i.e., filaments can be seen as density highlighted field lines.

equilibrium reconstruction of a typical ASDEX Upgrade discharge. The filament is indicated by the red line, compared to the unperturbed field line in blue. The filament winds around the torus, following a magnetic field line with the local field line inclination angle, which is in the order of  $10^\circ$  for typical ASDEX Upgrade discharges. The radial displacement has been approximated by a linear displacement with regards to the poloidal height  $z$  on top of the plasma shape (similar to a violin string that has been excited with a violin bow). The filament in fig. 2.8 is connected to the core plasma and winds a bit more than 1 time around the torus. The true length depends on where the filament is connected to the core plasma.

The alignment to the magnetic field has certain implications on the motion of such a filament: Filaments can only move perpendicular to the magnetic field, which means that they can either rotate<sup>1</sup> poloidally/toroidally or move radially. However, in a torus, it is impossible to distinguish between poloidal and toroidal motion. From a mathematical point of view, rotations in both directions are equivalent, so that a poloidal motion can be described as a toroidal motion and vice versa:

$$\frac{v_{pol}}{v_{tor}} = \frac{B_{pol}}{B_{tor}} = \tan \alpha, \quad (2.8)$$

<sup>1</sup>Rotation refers to the rotation of the filament around the symmetry axes of the torus (poloidal, toroidal). To indicate a rotation of the filament around its own axis, the term vorticity will be used.



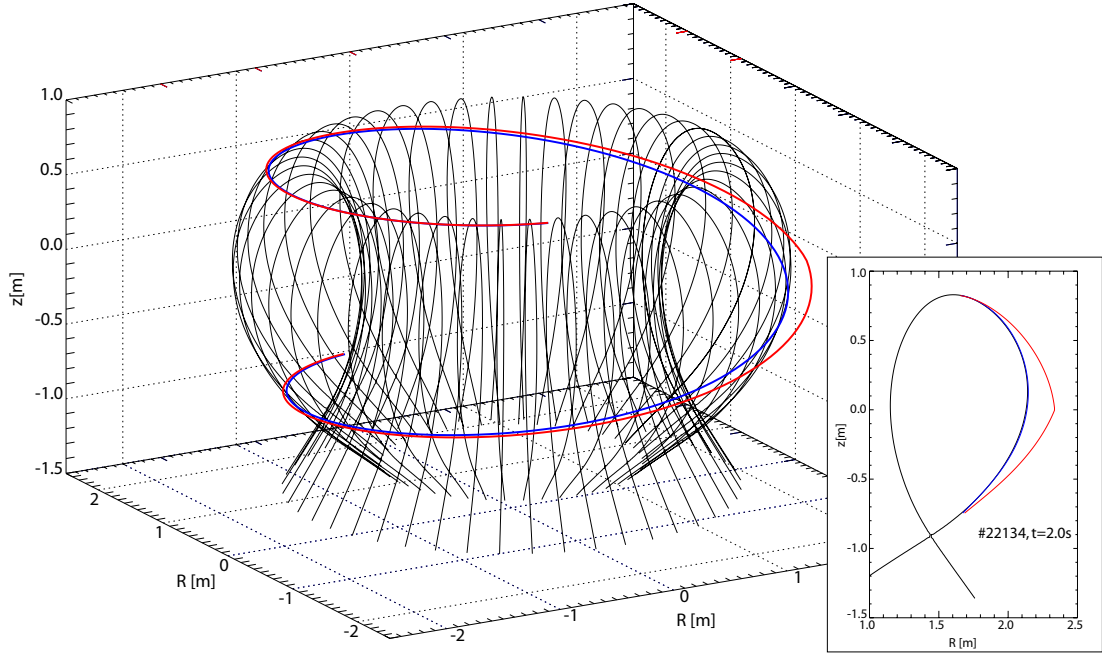


**Figure 2.8:** 3D scheme of a filament as it winds around the torus, following the magnetic field lines (original field line in blue, displaced field line in red). For the illustration, a linear displacement proportional  $z$  has been chosen, with the filament being attached to the core plasma near the upper top and the lower X-point and the maximum displacement in the midplane. The displacement has been exaggerated to make the effect more visible.

with the field line inclination angle  $\alpha$ . In ASDEX Upgrade, the typical field line inclination angle is between  $7^\circ$  and  $12^\circ$ , corresponding to  $q$ -values between 3.5 and 7. Hence, the resulting conversion factor is  $v_{tor}/v_{pol} \approx 8 - 4$ . In MAST, the field line inclination is in the order of  $45^\circ$ . If in the following we refer to a poloidal or toroidal rotation velocity, this will always mean a motion mapped completely in poloidal or toroidal direction, but no composition of both velocities.

Fig. 2.9 shows a CAD view of the ASDEX Upgrade vessel. The blue line marks a filament with an inclination angle in the order of  $10^\circ$  as given by the magnetic field. The filament will move poloidally/toroidally as well as radially with velocities in the order of few km/s. If we assume that the filament lives long enough to move for a distance much larger than the filament size, it will pass by several probes installed in the ASDEX Upgrade vessel. Fig. 2.9 shows two probes: the new filament probe (red), which has been developed in the course of this thesis (see sec. 4.1 for details), and a midplane manipulator probe (green), which has already been used in [40] (see sec. 4.2 for details). Both probes lie along the same field line, so that the measurements can be directly correlated.

Fig. 2.10 shows a filament in front of the filament probe in the poloidal cross section. As a poloidal cut through a filament has a more or less elliptic shape, with the larger axis being in poloidal direction, the filaments are often referred to as blobs in literature. Fig. 2.10 also shows that in a poloidal plane, i.e. at a fixed toroidal position, the filament motion appears to be essentially poloidal and radial in direction, hence the above



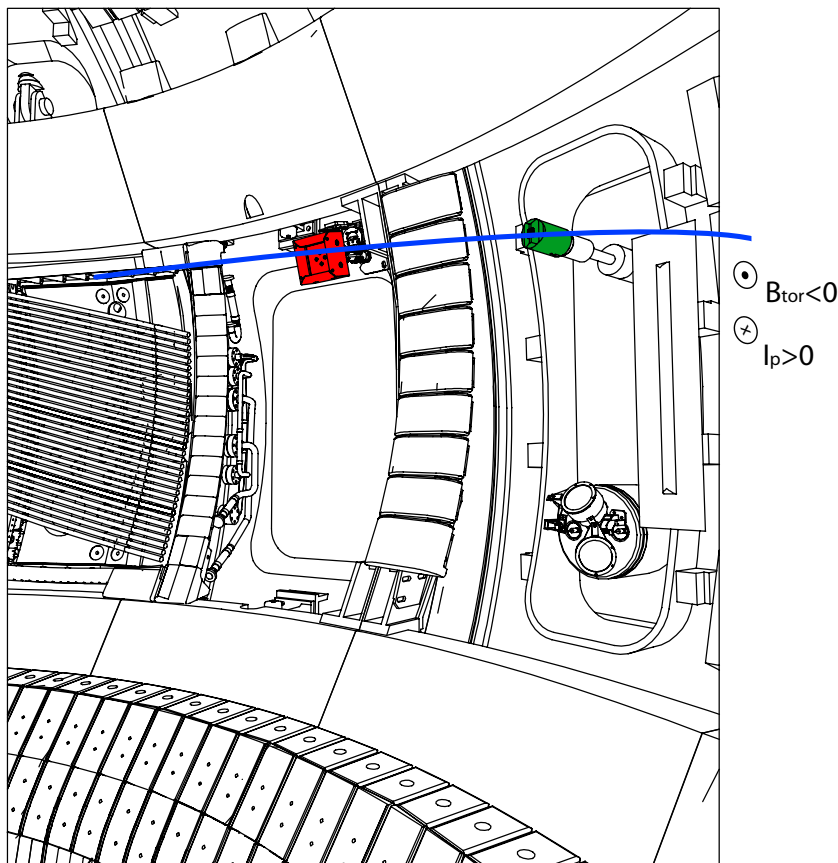


**Figure 2.9:** CAD view of one part of the ASDEX Upgrade vessel. The blue line shows the filament as a field aligned structure. The filament can move perpendicular to the magnetic field, i.e in poloidal/toroidal and radial direction simultaneously. The filament dynamics can be measured with two probes: the new filament probe (red, described in sec. 4.1) and various midplane manipulator probes (green, described in sec. 4.2).

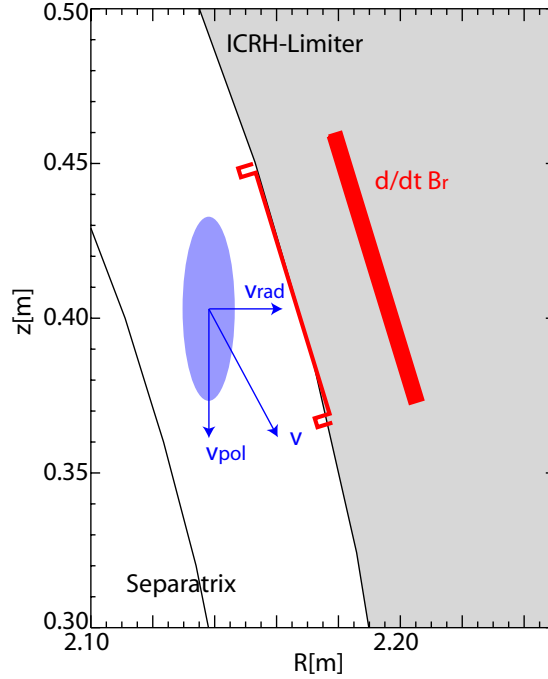
convention on poloidal and toroidal velocities.

Fig. 2.11 shows the twisting of a filament as it moves radially outwards from a starting position inside the separatrix ( $R = 2.00$  m) to a position in front of the filament probe ( $R = 2.18$  m). A significant change of the inclination angle can be found only inside the separatrix ( $R = 2.12$  m), but not outside the separatrix, where the inclination angle is roughly constant. Therefore, in ASDEX Upgrade, it is not possible to determine the radial position of a filament from visible imaging by fitting a field line to the filament, as is typically done on MAST [41, 42].

### 2.2.3 Important Filament Properties

Summarizing the present experimental results into a simple physical picture, the fraction of energy carried towards the wall by filamentary transport seems to depend strongly on several factors:

- How much energy each filament carries (deposited energy) and its size (wetted area),



**Figure 2.10:** Filament motion in the poloidal plane. The filament takes an elliptic shape often referred to as a blob when watched in a poloidal plane. The motion of such a blob can be described by radial and poloidal velocity components. The red structure shows the position of the Langmuir pins on the filament probe, and the magnetic pick-up coil, which is used to measure the radial component of the magnetic field of the impinging filaments.

- the velocity ratio  $v_{rad}/v_{pol}$  (with constant transport coefficients in parallel and radial direction, a radially faster filament will carry more energy to the wall),
- the gap between the separatrix and the limiter (a bigger gap leaves more time for energy loss along the field line and thus more energy is transported towards the divertor),
- and the uniformity of the interaction region (shaded areas will have a reduced heat load, whereas protruding structures will suffer from an enhanced heat load).
- The consequences for plasma facing components depend on the deposition time and the localization of the deposition and might easily exceed critical limits in future fusion devices.

A detailed extrapolation of filaments to future devices is at present not available. This thesis will therefore focus on measuring the filament properties in detail in order to give a starting point for an extrapolation to future fusion devices and a basis to understand the mechanism behind ELMs.

## 2.3 Theoretical Approach

Type-I ELMs have early been regarded as an ideal MHD instability due to the fast rise at the beginning of the ELM crash. Various studies have been carried out on ballooning

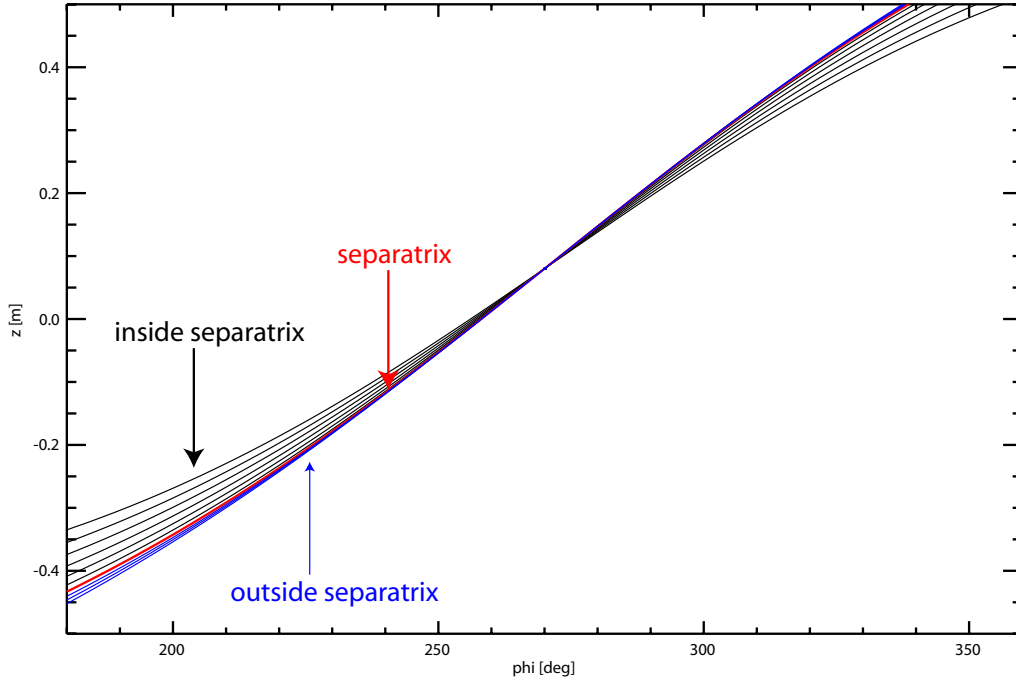


**Figure 2.11:** Twisting of a filament on its way radially outwards from  $R = 2.00$  m to  $2.18$  m with a  $2$  cm-spacing. The varying field line inclination angle forces the filament to become steeper with distance to follow the magnetic field lines. The red lines show the filament at the separatrix position, black lines are inside, and blue lines are outside the separatrix.

modes as well as on peeling modes, after the role of edge current and edge pressure gradient in the ELM cycle has early been recognised in the experiments. Later on, this has been extended to combined peeling-ballooning models, as, for typical H-Mode edge parameters, the limiting instability seems to be an intermediate- $n$  ( $n = 3 - 30$ ) coupled peeling-ballooning mode [43] (see also sec. 2.1.2). Pure ballooning-modes can be limiting at high collisionality ( $\nu^* \propto n/T^2$ ), and pure peeling-modes at low collisionality. A comprehensive review on the historic evolution towards current models of peeling ballooning modes in ideal or resistive MHD is given in [44, 43] together with an extensive collection of reference articles. The basic features are:

- Ballooning modes are characterized by the competition between the local destabilising pressure gradient in the bad-curvature region (which is at the low field side of a tokamak), and the stabilising field line bending that renders modes with  $n = \infty$  most unstable. Ballooning modes have a characteristic structure with large amplitudes on the low field side and small amplitudes at the high field side.
- Peeling or kink modes are driven by the edge current gradient, stabilised by the pressure gradient (due to favourable average curvature), and are most unstable for low- $n$  modes, e.g. the  $n = 1$  mode. The stability critically depends on the presence of a rational surface just outside the separatrix [44, 45]
- The peeling ballooning mode is driven by edge pressure gradient and edge current density and connects stability limits from both peeling and ballooning modes with

a stability limit for finite toroidal mode numbers.

An illustration of a high- $n$  ballooning mode, a low- $n$  peeling (or kink) mode, and a  $n = 20$  peeling-ballooning mode is given in fig. 2.12.

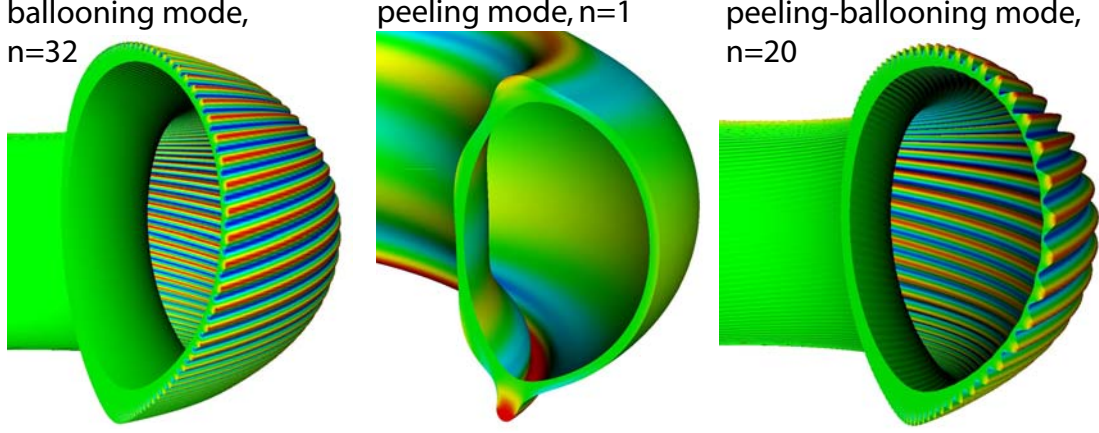


**Figure 2.12:** Mode structure of a  $n = 32$  ballooning mode, a  $n = 1$  peeling or kink mode, and a  $n = 20$  peeling-ballooning mode. From [44].

### 2.3.1 Linear Models

Several linear 2D MHD codes which can calculate the stability of the plasma edge in H-mode plasmas exist, e.g. ELITE [46, 47, 48], MISHKA [49], or GATO. The latter has, for example, been used for studying the role of the bootstrap current on the stability in real ASDEX Upgrade geometry [50].

The linear codes deliver stability limits on edge current density and pressure gradient that are in quite good agreement with experimental results [51]. It is generally found that the discharges are stable well before ELMs occur and then approach the peeling stability boundary just before ELMs are observed. The linear models, therefore, are successful in explaining the onset of type-I ELMs and the associated edge constraints. But even though these limits are well described by linear codes, the evolution is not described correctly: Real modes evolve slowly through the stability boundary, but then grow explosively on an extremely short timescale, which can not be understood by linear codes which would predict a slower evolution and lower growth rates. Nonlinear codes therefore have become necessary in order to describe the rapid evolution of the ELM instability.

### 2.3.2 Nonlinear Models

The theory for the early nonlinear evolution of ballooning modes in tokamak geometry was first developed by [52, 53]. The models have originally been based on considerations on solar flares and have then been adapted to tokamaks. A recent overview on the relationship between solar flares and ELM filaments is given in [54].

In the nonlinear models, the linear equation for the ballooning mode evolution is extended by adding second order terms to represent a nonlinear drive due to weakening of the stabilising field line bending as the flux tube expands, and by adding third order

terms that account for the evolution of the pressure gradient. The first terms give rise to an explosive evolution of the mode, whereas the latter drive the mode radially outwards, so that, finally, a localized flux tube is expelled from the plasma in an explosive manner.

JOKEK [55] is a nonlinear, resistive, reduced MHD code that correctly includes the tokamak separatrix geometry (with closed field lines inside and open field lines outside the separatrix) in order to improve modelling of the peeling mode part. The ideal peeling mode is usually stabilised when its rational surface lies inside the separatrix. As  $q \rightarrow \infty$  at the separatrix, modes inside the separatrix are usually stabilised in ideal MHD. Allowing for a finite resistivity lessens the stabilising effect of the separatrix. The resistive counterpart of the peeling mode, the peeling tearing mode, can therefore be driven unstable and takes over the role of the peeling mode in these calculations. Taking the correct separatrix geometry into account is only one part of the problem, as these codes do still rely on rational surfaces to calculate the peeling instability. As  $q \rightarrow \infty$  at the separatrix, the distances between different rational surfaces get to dimensions of gyro-radii, so that finite gyro-radii effects have to be taken into account (see below).

The BOUT code [56, 57, 58] is a 3D electromagnetic, reduced 2-fluid Braginskii simulation code that calculates over a region around the separatrix, including the pedestal region and the SOL. The interaction of a low- $n$  peeling mode (which is driven by the nonlinear interaction of medium- $n$  ballooning modes) with the dominant ballooning mode leads to the growth of one of the lobes of the ballooning mode. This occurs at the toroidal position where the low- $n$  mode and the high- $n$  ballooning mode reinforce each other. An explosive behaviour is observed, which results in the ejection of a filament. In the early stage of the BOUT simulation, the growth rates are similar to those from the linear calculations. In the following, however, the mode grows explosively with  $1/(t - t_0)^r$  with the starting time  $t_0$  and  $r = 0.5$  in comparison to  $r \approx 1.1$  as expected from linear theory. In [58], it has furthermore been studied whether one or several filaments are predicted: If the calculations are initialised with a broad band of toroidal mode numbers at random phase, the multiple modes grow linearly but with nonlinear coupling of nearest neighbours, strongly driving the lowest- $n$  mode (e.g.  $n = 1$ ). At the point of maximum resonance between the dominant linear mode (e.g.  $n = 20$ ) and the strongly driven lowest- $n$  mode, one single filament is ejected. If the calculations are initialised with a single  $n = 20$  mode, only harmonics are present at significant amplitude, even in the nonlinear phase. The radial burst occurs with the same symmetry as the mode structure, and a full set of 20 filaments is ejected into the SOL. Which of these cases happens in the experiment depends on the flatness of the growth rate spectrum and the rate at which the edge profiles are driven across the marginal point.

The behaviour in later stages, in particular the energy loss and the way how the plasma recovers to produce a complete ELM cycle, is difficult to predict. We will refer to this point again in sec. 7.4.

More recent reviews on non-linear codes and applications thereof can be found in [59, 43]. A somewhat different approach has recently been started by using the GEM code [60] for ELM studies [61]. GEM is a gyrofluid electromagnetic code that calculates the moments of the distribution function of the gyrocenters in a 6-moment gyrofluid model, i.e. it does not calculate the entire distribution function, but the moments derived from the distribution functions, including finite gyroradius effects to arbitrary order. The code has been designed for turbulence studies in core and edge and includes a lot of physics,

which makes it interesting to apply the code to ELM studies. The equilibrium is typically sustained in a self-consistent way, but for ELM studies an H-mode pedestal has been introduced artificially. The calculations show a rapid crash within  $20\ \mu\text{s}$ , resulting in blob-like structures that are expelled in the SOL as shown in fig. 2.13.

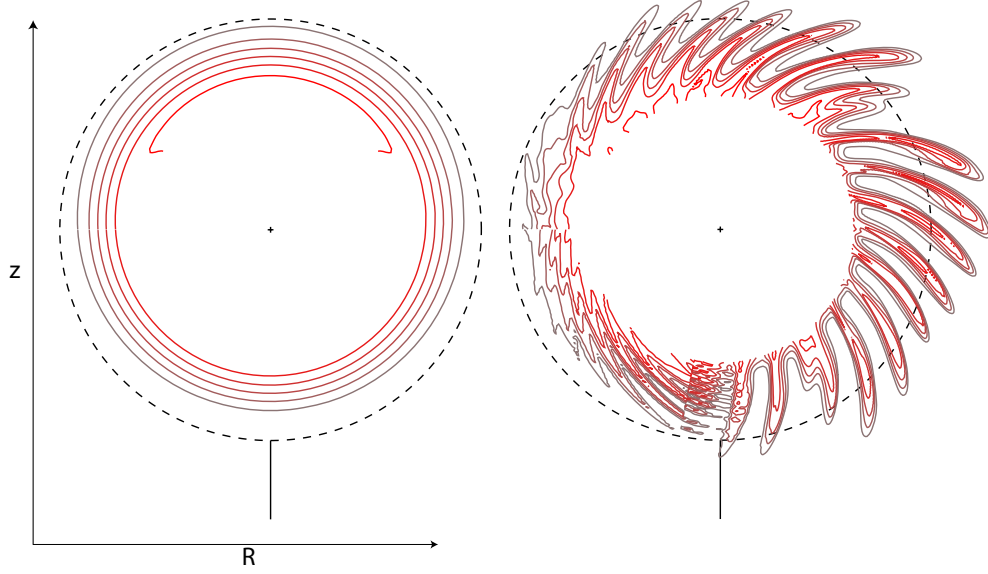


**Figure 2.13:** Numerical simulation of an ELM crash with the gyrofluid code GEM [61]. Left: Initial profile, right: during the ELM crash. The ELM crash leads to the formation of fingers at the low field side, which are ejected in the scrape-off layer. Note that the radial extent of the edge region has been exaggerated in these images.

## Chapter 3

# Radial Motion of Filaments and Field Aligned Structures

In this chapter, we will describe the radial motion of filaments with simple, analytical models based on the polarization of the filaments due to particle drifts.

### 3.1 Vertical Filament Polarization and Radial $\mathbf{E} \times \mathbf{B}$ Drift

Charged particles in a magnetic field gyrate around magnetic field lines. Additional forces can cause the guiding center of the particle motion to move perpendicular to the magnetic field [45]. In a tokamak, we have a radially varying toroidal magnetic field,  $B_{tor} \propto 1/R$ , which leads to varying particle gyro-radii  $\rho = mv_{\perp}/eB$ . This causes an effective particle drift, the so called  $\nabla B$ -drift

$$\mathbf{v}_{\nabla B} = \frac{mv_{\perp}^2}{2q_{el}B^3} \mathbf{B} \times \nabla \mathbf{B} \simeq v_{i,th} \frac{\rho_i}{R} \hat{\mathbf{z}}. \quad (3.1)$$

The latter holds for a toroidal geometry with the approximation  $v_{\perp}^2 \simeq v_{i,th} v_{\perp}$  and with the ion thermal velocity  $v_{i,th} = \sqrt{kT_i/m_i}$ .

Due to  $\nabla \cdot \mathbf{B} = 0$ , a varying magnetic field is inseparably connected to a curvature of the magnetic field lines, which causes the so-called curvature drift

$$\mathbf{v}_{curv} = \frac{mv_{\parallel}^2}{q_{el}B^3} \mathbf{B} \times \nabla \mathbf{B}. \quad (3.2)$$

Both drifts lead to a charge separation as ions and electrons drift in opposite directions: For  $B < 0$ , the ions drift downwards to the lower divertor, whereas electrons drift upwards (see appendix A for details on sign conventions). This leads to a polarization current density

$$\mathbf{j}_{plr} = \frac{nm}{B^3} \left( v_{\parallel}^2 + \frac{1}{2} v_{\perp}^2 \right) \mathbf{B} \times \nabla \mathbf{B} \quad (3.3)$$

in poloidal direction, and hence to a poloidal electric field  $E_{pol}$  as indicated in fig. 3.1. Usual quasi neutrality cannot be directly re-established as poloidal currents are hindered by the magnetic field: currents can only run force-free parallel to the magnetic field. That consideration leaves us directly with the idea of parallel currents that flow force free along the field lines. Such currents could be bridged somewhere near the end



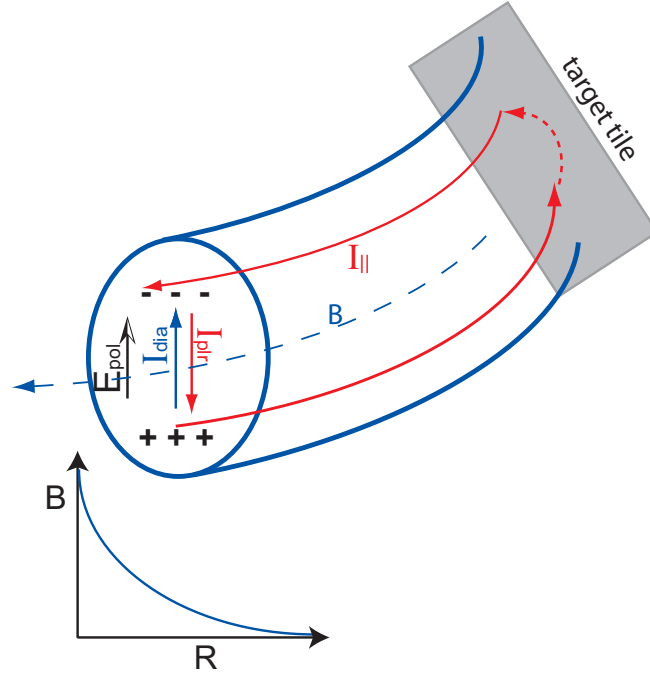


**Figure 3.1:** Filament polarization due to charge dependent drifts in a radially varying toroidal magnetic field. The curvature drift drives a poloidal polarization current  $I_{plr}$  which, in the presence of wall contact, can be partially short circuited by parallel currents  $I_{\parallel}$ . A diamagnetic current  $I_{dia}$  due to diamagnetic drift could also balance the polarization current. The resulting poloidal electric field drives a radial motion of the filament due to  $\mathbf{E} \times \mathbf{B}$ -drift.

of the filament, for example by interaction with target tiles. Several theories for filament propagation based on parallel currents have been proposed. They will be described in section 3.2.

Even though particle motion perpendicular to  $\mathbf{B}$  is hindered, there could be a poloidal current through drifts. Diamagnetic drift is a mechanism that provides a poloidal current, the so-called diamagnetic current. It is based on a pressure gradient perpendicular to the magnetic field and results in a mostly poloidal drift:

$$\mathbf{v}_{dia} = -\frac{\mathbf{B} \times \nabla p}{q_{el} n B^2}. \quad (3.4)$$

The associated diamagnetic current density is

$$\mathbf{j}_{dia} = \frac{\mathbf{B} \times \nabla p}{B^2}. \quad (3.5)$$

The continuity equation can be written as [62]

$$\nabla \cdot \mathbf{j}_{plr} + \nabla \cdot \mathbf{j}_{\parallel} + \nabla \cdot \mathbf{j}_{dia} = 0 \quad (3.6)$$

and says basically that the polarization current  $\mathbf{I}_{plr}$  from eq. (3.3) can be balanced by both the diamagnetic current  $\mathbf{I}_{dia}$ , eq. (3.5), and the parallel current  $\mathbf{I}_{\parallel}$ , which will be derived in sec. 3.2. A model for the radial propagation of filaments based on the



polarization current is described in sec. 3.3.

Similar problems have already been treated in the area of pellet fuelling several years ago [63, 64]. Small cryogenic deuterium pellets are injected into the plasma for fuelling and artificial ELM triggering. A plasma cloud forms and propagates radially in the core plasma due to  $\mathbf{E} \times \mathbf{B}$ -drift as we will see in sec. 3.2. The currents are somewhat different in that case as the pellet cloud moves in the region of closed field lines, whereas filaments move in the region of open field lines and possibly touch the target walls.

## 3.2 Parallel Currents and Sheath Damping

When a filament has detached from the plasma core and connects to target tiles, currents of ions and electrons flowing parallel to the magnetic field can bridge over the target tiles (see fig. 3.1).

Plasma sheaths with finite resistivity form at the tiles according to Debye theory [45, 65] but do not provide a complete short circuit even if we neglect any resistivity of the target tiles. Details on sheath formation, sheath properties and the occurring resistivities are given in Appendix C.

The current  $I_{\parallel}$  adds up along the field line as the charge separating drifts (3.1) and (3.2) happen all along the filament.  $I_{\parallel}$  will therefore be 0 at the midplane and obtain its maximum value close to the sheaths as shown in fig. 3.2.

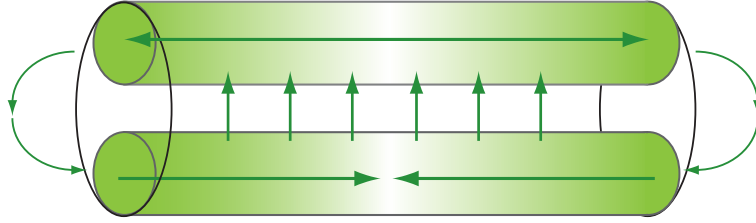


**Figure 3.2:** Current distribution along the filament. As charge polarization happens all along the filament, the current accumulates and takes a minimum near the midplane and a maximum close to the target tiles.

The poloidal voltage between the upper and lower part of the filament is determined by the sheath resistivity and the parallel current,

$$U_{pol} = R_{sheath} I_{\parallel}. \quad (3.7)$$

The sheath physics of Langmuir single probes in a magnetic field is similar to double probes without magnetic field [66, 40, 67]: A voltage  $\phi$  between 2 connected electrodes results in a parallel current  $I_{\parallel}$

$$I_{\parallel}(\phi) = \frac{A_1 + A_2}{2} j_{i,sat} \left[ \tanh \left( \frac{e\phi}{kT_e} - 0.5 \ln \frac{A_1}{A_2} \right) - \frac{A_1 - A_2}{A_1 + A_2} \right] \quad (3.8)$$

$$= A j_{i,sat} \tanh \frac{e\phi}{2kT_e} \quad (3.9)$$

with  $A = A_1 = A_2$  for identical probe size and  $j_{i,sat} = en_i c_s$ . The resulting characteristic is shown in fig. 3.3.

The maximum current  $A j_{i,sat} = I_{\parallel,sat}$  can only be obtained for  $|e\phi| \gg kT_e$ , where

$j_{\parallel} = j_{sat}$ . This means, that all the ions in the filament will still flow to the target plates, whereas electrons will only go to the more positive electrode. The total ion and electron flux from the plasma to both electrodes must of course be equal to sustain quasi-neutrality. In the limit  $|e\phi| \ll kT_e$ , the potential is smaller than the average

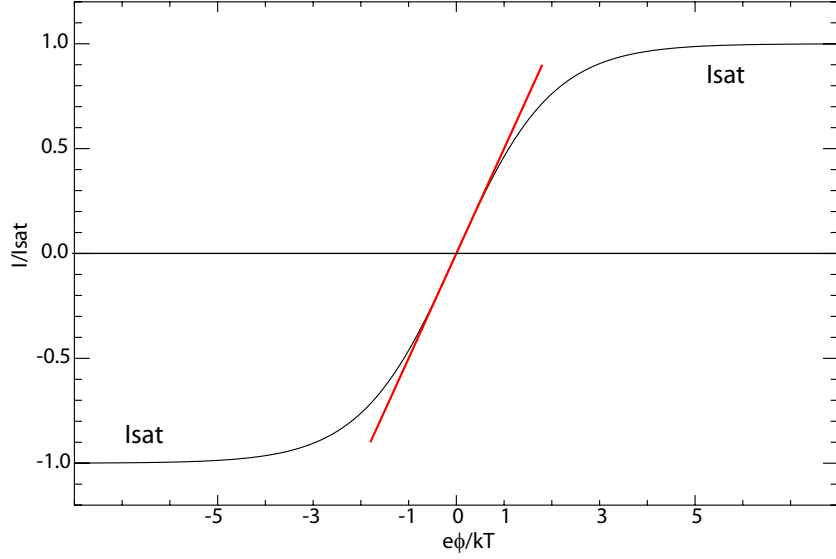


**Figure 3.3:** Current-Voltage-Characteristic of a Langmuir double probe.

kinetic energy of the electrons. The slight imbalance in the electron reflection leads to a linear characteristic similar to an ohmic resistor. The sheath resistivity is

$$R_{sheath} = \left. \frac{d\phi}{dI} \right|_{\left| \frac{e\phi}{kT} \right| \ll 1} = \frac{2kT_e}{eI_{\parallel,sat}}. \quad (3.10)$$

With eq. (3.7), we obtain a poloidal voltage

$$U_{pol} = \frac{2kT_e}{e} \frac{I_{\parallel}}{I_{\parallel,sat}}. \quad (3.11)$$

The parallel ion saturation current  $I_{\parallel,sat}$  means that all ions in the ion branch of the filament are flowing with sound speed towards the target tiles and thus can be written as

$$I_{\parallel,sat} = \Delta_{pol} \Delta_{rad} n_{fil} e c_s \quad (3.12)$$

with the poloidal height of the filament  $\Delta_{pol}$ , the radial extent  $\Delta_{rad}$ , filament density  $n_{fil}$ , and the sound speed

$$c_s = \sqrt{\frac{k(T_e + \gamma T_i)}{m_i}}. \quad (3.13)$$

in the collisional limit with the adiabatic exponent  $\gamma = (f + 2)/f = 5/3$  for 3 degrees of freedom. For a discussion on other limits of  $\gamma$  such as  $\gamma = 3$  in magnetized plasmas see [65].

$I_{\parallel}$  is the target current caused by the polarization of the filament,

$$I_{\parallel} = n_{fil} e \left( v_{i,th} \frac{\rho_i}{R} \right) l_{\parallel} \Delta_{rad}, \quad (3.14)$$

where  $v_{i,th}\rho_i/R$  is the drift term from eq. (3.1) and  $l_{\parallel}$  the length of the filament along the field line (typically in the order of 10 m). Combining eq. (3.11) with eqns. (3.12) and (3.14) in the limit  $T_e = T_i = T$  gives

$$E_{pol} = \frac{U_{pol}}{\Delta_{pol}} = \frac{2kT}{e} \frac{\rho_i}{\Delta_{pol}^2} \frac{l_{\parallel}}{R}. \quad (3.15)$$

The poloidal electric field  $E_{pol}$  changes the gyro-motion of the particles and thus leads to a charge independent  $\mathbf{E} \times \mathbf{B}$ -drift

$$\mathbf{v}_{E \times B} = \frac{\mathbf{E} \times \mathbf{B}}{B^2} \approx \frac{E_{pol}}{B} \mathbf{e}_R \quad (3.16)$$

which moves the filament radially outwards with a velocity

$$v_{rad} = \sqrt{2} v_{i,th} \frac{v_{i,th}}{c_s} \left( \frac{\rho_i}{\Delta_{pol}} \right)^2 \frac{l_{\parallel}}{R} \approx \sqrt{2} c_s \left( \frac{\rho_i}{\Delta_{pol}} \right)^2 \frac{l_{\parallel}}{R} \quad (3.17)$$

and the approximation  $v_{i,th} \approx c_s$ . Note that  $l_{\parallel}/R \approx q$ .

Now we have to validate the assumption  $|e\phi| \ll kT$ , or  $I_{\parallel} \ll I_{\parallel,sat}$ , respectively. Using the latter together with eq. (3.12) and (3.14) results in

$$\frac{\Delta_{pol}}{\rho_i} \gg \frac{l_{\parallel}}{R} \approx q. \quad (3.18)$$

This means, that our assumption holds if  $\Delta_{pol} \gg q\rho_i$ . With  $\rho_i = 2.04 \cdot 10^{-4} \text{ m} \sqrt{T(\text{eV})/B(\text{T})}$  and  $\Delta_{pol}/l_{\parallel} \approx 3\text{cm}/10\text{m} = O(10^{-3})$ , we see that this is true for temperatures of up to 1 keV and in particular for the ASDEX Upgrade SOL and filaments, which usually have  $T < 100 \text{ eV}$  [68].

Here is a summary of the vital points of this simple model:

- The model describes a filament that has detached from the plasma and is connected to the target tiles, hence limiting the current. We have assumed the filament shape to be blob like in the poloidal cross section with a poloidal extent  $\Delta_{pol}$  and a radial extent  $\Delta_{rad}$ . The length  $l_{\parallel}$  along the field lines is large compared to  $\Delta_{rad}$  and  $\Delta_{pol}$ .
- According to eq. (3.17), filaments with a smaller height  $\Delta_{pol}$  should move faster than bigger filaments. The radial size  $\Delta_{rad}$  does not influence  $v_{rad}$ .
- Close to the X-point, we expect the filament shape to become strongly distorted. When filament dimensions approach the ion gyroradius  $\rho_i$ , completely different effects will take over. Our assumptions fail close to the X-points, where  $q \rightarrow \infty$  and the filament size becomes of the order of the ion gyroradius  $\rho_i$ . Therefore, this simple model only holds in the far SOL where the filament is far away from the X-points.
- The model does only describe the filament propagation in the far SOL. Filament creation and detachment are far beyond this model and even the more refined models shown in the following sections. The numerical simulations described in section 2.3 are better suited for understanding the filament evolution.

From a more general point of view, we expect that the described model can be qualitatively extended by the following filament properties:

- Filaments with  $I_{\nabla B} \gg I_{\parallel, \text{sat}}$ , i.e.,  $\Delta_{\text{pol}}/\rho_i \ll q$  should be accelerated with  $a = 4kT/mR$ . Note that the adiabatic coefficient has been introduced erroneously in [69] according to [19].
- Bigger filaments should evolve into smaller, faster structures by detaching from the parent filament. The detachment process might again be caused by nonlinear mode growth comparable to the detachment of the parent filament from the plasma core.

It is important to note that the contact with the target plates is not the only possibility to bridge parallel currents. Shearing of a filament in proximity of the X-point eliminates electrical contact with the divertor, see fig 3.4, and allows a connection of the parallel currents due to finite-gyroradius effects, [70, 71]. The filament dimensions are sheared to the gyro-radii scale and hence electrically decoupled from the divertor.

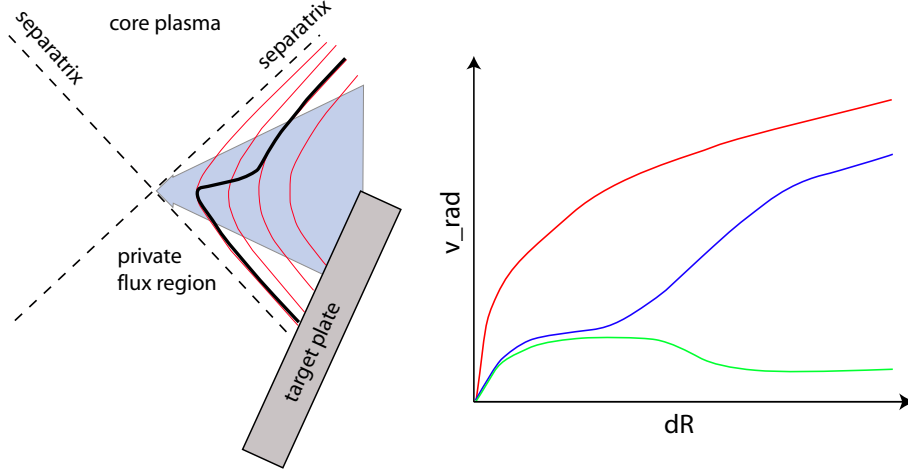


**Figure 3.4:** Left: Possible decoupling mechanism for a filament close to the X-point due to strong shear as suggested in [70]. The filament dimensions are sheared until the gyro-radii scale and electrically decoupled from the divertor. The authors suggest that the electrical connection might possibly not be re-established even at larger distances. The black line illustrates the shape that the filament is assumed to take instead of following the red field lines. Right: Possible scenarios for the radial velocity of a filament: free acceleration without any (red) connection to X-point, with (blue) and without connection to target (green).

### 3.2.1 Dependence on Filament Density

In [72], the sheath damping model has been extended to include varying density along the field line, namely a density  $n_{\text{fil}}$  near the midplane and a density  $n_t$  at the target. The basic equations are the current continuity equation (3.6) with  $\mathbf{j}_{\text{plr}} = 0$ , the diamagnetic current (3.5), and the boundary condition

$$j_{\parallel} \big|_{\text{target}} = en_t c_s \frac{e\phi}{kT}. \quad (3.19)$$

for the parallel current at the target. The equations do not rely on assumptions on homogeneity in this stage but hold for arbitrary filament structures. This leads to the solution

$$\frac{e\phi}{kT} = \frac{l_{\parallel}\rho_i}{2Rn_t}\partial_y n_{fil}, \quad (3.20)$$

assuming a filament density  $n_{fil}$  and neglecting effects of magnetic shear. Eq. (3.20) is used to calculate the  $\mathbf{E} \times \mathbf{B}$  velocity. This allows to solve the blob plasma continuity equation in the absence of sources,

$$\partial_t n_b + \nabla \cdot n_b \mathbf{v} = 0 \quad (3.21)$$

with  $n_t = \text{const} \cdot n_{fil}$  and an ansatz

$$n_{fil}(t, R, y) = n_{fil,rad}(t, R) n_{fil,y}(y) \quad (3.22)$$

$$n_{fil,y}(y) \propto \exp\left(-\frac{y}{\Delta_{pol}}\right), \quad (3.23)$$

resulting in the ballistic equation

$$(\partial_t + v_{rad}\partial_R)n_{fil,R} = 0 \quad (3.24)$$

with the filament propagation velocity

$$v_{rad} = c_s \left( \frac{\rho_i}{\Delta_{pol}} \right)^2 \frac{l_{\parallel}}{R} \frac{n_{fil}}{n_t}. \quad (3.25)$$

Eq. (3.25) generally reproduces the result (3.17), enhanced by the filament density term, which states that filaments with a higher density ratio  $n_{fil}/n_t$  move faster. The ratio  $n_{fil}/n_t$  can be estimated with the two-point model [65] by calculating the dynamic pressure along the filament with the Bernoulli equation

$$p + nmv_{\parallel}^2 = \text{const}, \quad (3.26)$$

where  $v_{\parallel}$  is the flow speed along the magnetic field line to the target plates. At the midplane, we have  $v_{\parallel} \approx 0$ , whereas at the target  $v_{\parallel} \approx \sqrt{2kT_t/m_i}$  holds. A detailed description of how to combine the dynamic pressure with a particle balance and a power balance is given in [65].

The radial penetration depth into the SOL can be estimated from the radial velocity and the filament lifetime  $\tau_{fil} = l_{\parallel}/c_s$ :

$$dR_{typ} = v_{rad}\tau_{fil} = R \left( \frac{q\rho_i}{\Delta_{pol}} \right)^2 \frac{n_{fil}}{n_t}. \quad (3.27)$$

### 3.2.2 Three-Field Braginskii Model

In [73], the sheath damping model has been extended by using a three-field Braginskii model for density, temperature and potential. The discussion is limited to the far SOL in which the diffusive background density is negligible, and where filaments can be treated as isolated and noninteracting.

The SOL has been divided in 2 regions: The first one, located within about one exponential decay length from the separatrix is determined by radial diffusion from the core and parallel particle loss to the sheaths; The heat loss is dominated by heat conduction, and the X-point can lead to a significant variation along the magnetic field line. The second region (far SOL) is dominated by filamentary transport and neutral ionization, which can help in sustaining the filamentary transport. The model consists of the following vorticity, continuity and temperature equations:

$$\frac{c^2}{B^2} n m_i \frac{d}{dt} \nabla_{\perp}^2 \phi = \nabla_{\parallel} j_{\parallel} + \frac{2c}{B} \mathbf{b} \times \mathbf{k} \cdot \nabla p \quad (3.28)$$

$$\frac{dn}{dt} + \nabla_{\parallel} (n v_{\parallel}) = \xi n \quad (3.29)$$

$$\frac{dT_e}{dt} + \nabla_{\parallel} (v_{\parallel} T_e) = \frac{2}{3n} \nabla_{\parallel} (\kappa_{\parallel} \nabla_{\parallel} T_e) - \xi E_i \quad (3.30)$$

where  $d/dt = \partial_t + \mathbf{v_E} \cdot \nabla$ ,  $\mathbf{v_E} = (c/B) \mathbf{b} \times \nabla_{\perp} \phi$ ,  $\mathbf{B} = B \mathbf{b}$ ,  $\mathbf{k} = \mathbf{b} \cdot \nabla \mathbf{b}$  is the magnetic curvature,  $v_{\parallel}$  is the parallel mass flow velocity,  $n_e = n_i = n$ ,  $\kappa_{\parallel}$  is the parallel heat conductivity,  $\xi = n_o < \sigma v >_i$  is the neutral particle ionization rate,  $n_o$  the neutral density and  $3/2 E_i$  is the total energy required per ionization. With  $T_e \gg T_i$ , and neglecting some small parameters, the equations can be solved by integrating along field lines, i.e. assuming constant parameters along  $\mathbf{B}$ . The boundary conditions are  $v_{\parallel} = c_s$  at the sheath entrance and a matching of  $j_{\parallel}$  to the sheath current

$$j_{\parallel} = n e \left( v_{\parallel} - \frac{v_e}{\sqrt{2\pi}} e^{-e\phi/kT_e} \right), \quad (3.31)$$

with the thermal electron speed  $v_e$ . The field lines are assumed to end in grounded plates, i.e. without any bias potential.

First of all, the solution is derived for dense filaments, i.e., filaments that differ from the background by an enhanced density. In Cartesian coordinates  $(R, y)$ , the resulting filament velocities are:

$$v_{rad} = c_s \left( \frac{\rho_i}{\Delta_{pol}} \right)^2 \frac{l_{\parallel}}{R} \quad (3.32)$$

and  $v_{pol} = 0$  for an arbitrary density distribution in the filament. This result is basically identical to eq. (3.17), except for the missing factor  $\sqrt{2}$ . The density decay time  $\tau_n = 1/(\alpha - \xi)$  is determined by the balance between the loss rate due to particle flow to the plates,  $\alpha = 2\rho_i/l_{\parallel}$ , and the rate of particles that are resupplied by ionization,  $\xi$ . When  $\Delta_{pol}$  approaches  $\rho_i$  and thus reaches the limit of the gyrofluid description, the radial velocity  $v_{rad}$  goes to  $c_s$ .

A solution in cylindrical coordinates gives the velocities

$$v_{rad} = c_s \left( \frac{\rho_i}{\Delta_{pol}} \right) \partial_r \ln n(r) \frac{l_{\parallel}}{R} \quad (3.33)$$

and  $v_{pol} = 0$ , which is identical to eq. (3.32) for a Gaussian density profile  $n_{fil}(r) = n_{fil,0} \exp(-r^2/2\Delta_{rad}^2)$  in radial direction ( $\partial_r \ln n(r) = \partial_r n(r)/n(r)$ ).

Possible extensions of the model can lead to a non-vanishing or even sheared poloidal velocity  $v_{pol}(y)$ . A sheared poloidal velocity could be produced by biasing of the divertor end plates or a radial temperature gradient. Both would lead to a significant distortion

of the blob shape, but would not directly affect  $v_{rad}$  (except for indirect effects due to poloidal broadening).

In addition to filaments with higher density compared to the ambient background plasma, this model is also capable of describing filaments with higher vorticity and higher temperature. Assuming cylindrically symmetric filaments, constant temperature in the filament and neglecting ionization, D'Ippolito et al. find the following results:

- $n(r, t)$  and  $T(t)$  do not decay exponentially, but by power laws because of the temperature dependence of particle losses. The temperature decays more quickly than the density because parallel energy transport is much faster than the particle transport.
- A radial potential in the filament causes vorticity, which can then cause an azimuthal rotation of the filament and hence symmetrization of its density. The potential

$$\phi(r, t) = \phi_B(t) + \phi_0(r)e^{-\gamma t} \quad (3.34)$$

consist of 2 parts: The Bohm potential  $\phi_B(t) = 3kT_0(t)/e$  confines the electrons that are streaming along field lines to ensure quasi-neutrality and decays on the shorter temperature time scale. The second component decays due to the flow of parallel currents to the sheaths, so that both components decay faster than the density.

As a result of an initial vorticity  $\nabla_\perp^2 \phi$ , the spinning filament symmetrizes its density,  $n(r, \theta) \rightarrow n(r)$ , if the rotational eddy time is much less than the density decay time, which is the case for typical parameters. When the initial vorticity has decayed, the simple solution for the density structure (3.32) is recovered.

- On the slower density timescale, the particle drifts (3.1), (3.2) polarize the filament, creating a poloidal electric field  $E_{pol}$ , which in turn results in an  $\mathbf{E} \times \mathbf{B}$ -drift outwards with the radial velocity (3.32).
- If the filaments decay before leaving the formation region, they do not contribute to the radial transport. Ionization in the far SOL can sustain the filaments longer against parallel loss of particles on a timescale  $\tau_{fil} = l_\parallel/c_s$  and thus allows larger filaments to contribute to the transport. Otherwise, they would be depleted before moving a significant distance as described by eq. (3.27).

### 3.2.3 Fragmentation of Filaments

Primary instabilities at the core plasma edge create the filaments near the separatrix, whereas secondary instabilities, driven by the filament internal pressure profile, should cause larger filaments to disintegrate into smaller ones. According to the presented model, smaller (child) filaments should move faster than their parents and thus give rise to fragmentation and increased net radial transport. Secondary instabilities have been discussed in [74, 75, 76] in great detail. We will restrict our view to features which are accessible to experimental observations.

- Two instabilities, which are driven by the filament internal profile are the Kelvin-Helmholtz instability, and sheath interchange modes. The Kelvin-Helmholtz instability is driven by velocity shear and becomes important for small filaments, whereas sheath-interchange modes are driven by curvature and become important

for large filaments.

For the sheath-interchange modes, it has been shown in [74] that large filaments with  $\Delta_{rad} > 30\rho_i$  will break immediately into smaller ones, whereas smaller filaments with  $\Delta_{rad} < 10\rho_i$  are stable and propagate radially until they hit the wall. For filament ion temperatures between 30 and 60 eV [68], this gives instability for  $\Delta_{rad} > 120 - 160$  mm and stability for  $\Delta_{rad} < 4 - 6$  mm. Filaments between these values tend to fragment as they propagate through the SOL.

- 2D simulations of the time behaviour have been carried out by integrating the Braginskii equations (3.28-3.30) [76]. In general, this has confirmed most of the points described above, but a new observation affects the shape of the filament in the poloidal cross section in the presence of a non-vanishing floor density: The shape is modified by sheared flows, leading to a double-vortex structure in  $\phi$  and thus a compression of the density contours in the direction of the filament motion. The simulations predict the filament to have a steep leading edge and a trailing wake as shown in fig. 3.5.

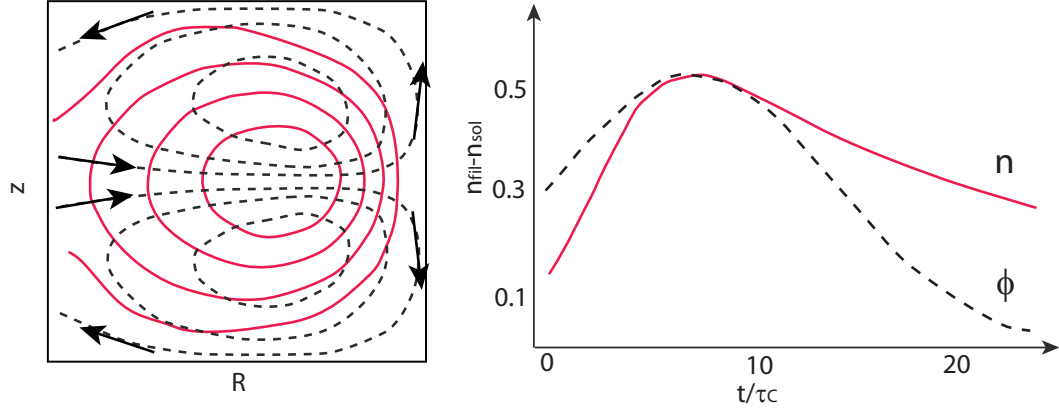


**Figure 3.5:** Left: Poloidal cross-section of a filament moving to the right in front of a constant background density in terms of density (solid line) and potential/flow (dashed line). Right: Numerical simulation of the time trace  $n(t)$  of the moving filament as seen by a Langmuir probe at a fixed spatial point. From [76].

### 3.3 Diamagnetic Current

In [77, 62], a model based solely on a diamagnetic current has been proposed. When the charge separation in the filament is dynamically balanced by the diamagnetic current, the result is a large-scale convective flow field and hence a radial acceleration of the filament.

The evolution of a filament has been modelled by an advection-diffusion equation for the density:

$$\left( \partial_t + \frac{\hat{\mathbf{z}}}{B} \times \nabla \phi \cdot \nabla \right) n = \chi \nabla_{\perp}^2 n \quad (3.35)$$

The equations for the convective flow dynamics arises from the current continuity equation (3.6). Parallel currents have first been neglected, but their effects will be shown



further down. The calculations start with a filament with circular cross-section of the form

$$n_{fil}(\mathbf{x}, 0) = n_{fil,0} \exp \left( -\frac{1}{2}(\mathbf{x} - \mathbf{x}_0)^2 \right). \quad (3.36)$$

Diffusion with diffusivity  $D$  would spread the filament as

$$n_{fil}(\mathbf{x}, t) = \frac{n_{fil,0}}{1 + 2Dt} \exp \left( -\frac{(\mathbf{x} - \mathbf{x}_0)^2}{2(1 + 2Dt)} \right). \quad (3.37)$$

The full calculations give a radial motion with several stages (fig. 3.6): In the first stage, the filament accelerates rapidly for about 5 ideal interchange times, corresponding to a radial distance of 1-2 times its initial size, i.e. about 1 – 2 cm for ASDEX Upgrade as we will see below. A steep front and a trailing wake as indicated in fig. 3.5 form at the filament.

In the second stage, the filament reaches a constant velocity. In the ideal limit, where inertia is dominant, this velocity is given by

$$v_{rad} = c_s \left( \frac{2\Delta_{pol}}{R} \frac{n_{fil}}{n_{sol}} \right)^{0.5}, \quad (3.38)$$

with the SOL density  $n_{sol}$ . Surprisingly, eq. (3.38) predicts that large filaments move faster, and thus are most harmful for first wall structures as they also carry more particles. The model does not predict any acceleration of the filaments in later stages. The filaments might even slow down due to dispersion.

In later stages, depending on the detailed parameters, in particular Reynolds and

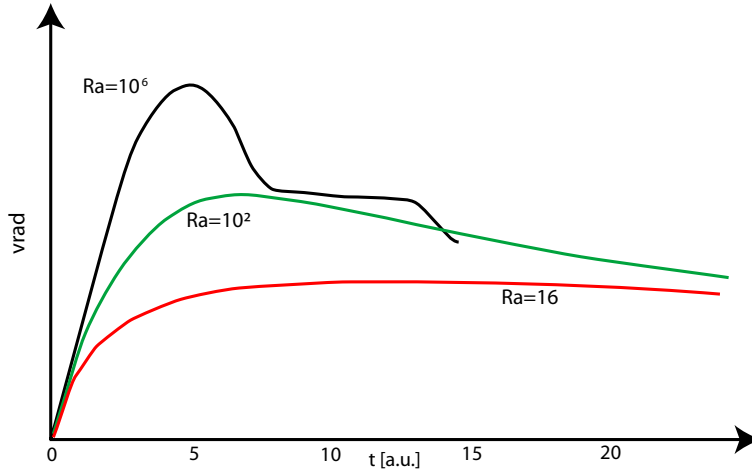


**Figure 3.6:** Evolution of the radial propagation velocity for different Reynolds-numbers according to [62]. In a first stage, up to 2 cm away from the separatrix, the filament is rapidly accelerated to the ideal velocity from eq. (3.38). The second stage will have either constant velocity or slow down due to dispersion.

Prandtl numbers, the filament might undergo strong distortion and obtain a mushroom-like cap in the poloidal cross section as shown in fig. 3.7. The filament might then break into 2 lobes, leaving two smaller filaments with opposite vorticity, which in the end might bring the filament to a halt. The roll-up will lead to an expansion in poloidal direction

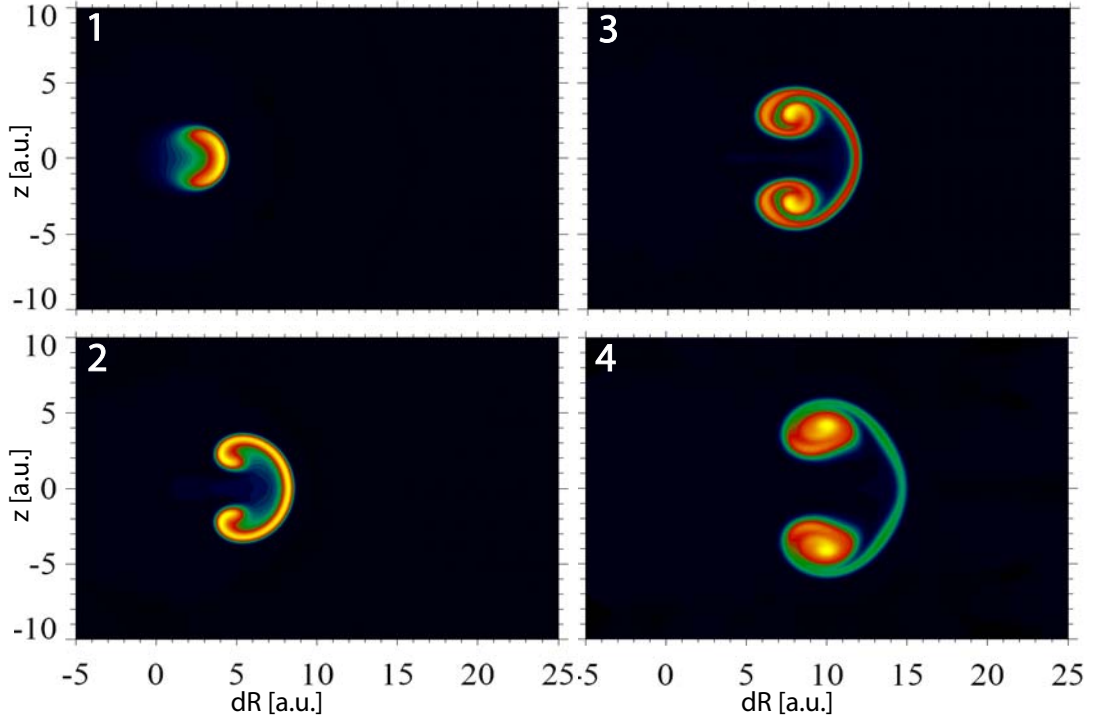


**Figure 3.7:** Evolution of the filament shape according to [62]. The filament might obtain a mushroom-like cap and break into two fragments afterwards. The exact behaviour depends strongly on the Reynolds and Prandtl numbers.

and might give a hint for the elliptic cross-section of filaments. In any case, the filament will travel a radial distance far larger than its initial size. The amplitude decays with time due to collisional diffusion (3.37) and stretching by convective motion. Adding parallel currents similar to eq. (3.9) and, accordingly, dissipation by plasma sheaths leads to a total of three terms [62]:

- interchange drive, causing radial convective transport
- viscosity, damping small spatial scales
- sheath currents, linearly damping large spatial scales

The resulting radial propagation velocity is

$$v_{rad} = c_s \left( \frac{\rho_i}{\Delta_{pol}} \right)^2 \frac{l_{\parallel}}{R} \quad (3.39)$$

in agreement with the equations in sec. 3.2. For large Rayleigh numbers or smaller collisional dissipation, the filament becomes subject to instabilities and breaks into very small structures in presence of sheath dissipation.

Pellet cloud propagation studies [63, 64] have produced similar results, in particular for the shape of the plasma cloud: The calculations give a similar mushroom-like shape, but as the pellet represents a longer-lasting source of particles, the mushroom has a stem that connects the cap with the still ablating pellet. This shape would also be expected for filaments, if the formation mechanism would last longer.

## Chapter 4

# Experimental Setup

### 4.1 Magnetically Driven Filament Probe

A radially movable probe has been developed for studies of ELM induced filamentary transport in ASDEX Upgrade by means of Langmuir probes and magnetic pickup coils, [78]. The probe is permanently installed at the low field side of the ASDEX Upgrade vacuum vessel and is not subject to limitations in probe size, as, for example, probes on the midplane manipulator (sec. 4.2) are. The probe is moved by a magnetic drive, which allows for easy installation in the vessel, and which has only moderate machine requirements as it will only require an electric feedthrough and an external power supply. The drive gives a linear motion with a radial range of 5 cm within 50 ms, but range and velocity can be largely scaled according to experimental requirements.

The new probe allows to measure the structure of filaments, in particular parameters such as filament motion and size using time delay measurements. Activating the drive moves the probe from a safe position behind the limiter to a position in front of the limiters, i.e., exposes the Langmuir pins to the SOL plasma.

In order to understand the basic mechanisms behind filaments and their role in radial heat and particle transport, it is necessary to measure the filament dynamics as well as density and temperature of ions and electrons in detail. This requires both good temporal and spatial resolution in the outer midplane. Langmuir probes are an important tool to measure filament properties, as they provide localized measurements (in the order of the pin size, but not smaller than the ion gyroradius  $\rho_i$ ) and can be run at high sampling rates. On ASDEX Upgrade, filament studies have successfully been carried out using Langmuir probes on a reciprocating midplane manipulator [31]. These probes clearly show filamentary structures passing by, but are not suited for measuring the rotation velocities of filaments because of the small distance between the Langmuir pins. As the probe size on the midplane manipulator is limited by the manipulator feedthrough, we have installed a new probe for filament measurements in the ASDEX Upgrade vessel. The probe consists of several Langmuir pins in suitable distances ( $\approx 10$  cm) and a magnetic pickup coil in the center.

In section 4.1.1, we will discuss the setup of the new filament probe. Section 4.1.2 will focus on the calculation of the force balance of the magnetic drive, whereas section 4.1.3 will discuss the heat produced by the drive itself. In section 4.1.4, we will show the dynamics of the resulting motion of the probe head, which is described in sec. 4.1.5.

### 4.1.1 Setup of the Filament Probe

The filament probe basically consists of 2 parts: a probe head, which carries the Langmuir and magnetic probes and acts as a plasma facing component, and a mounting mechanism (see fig. 4.1).

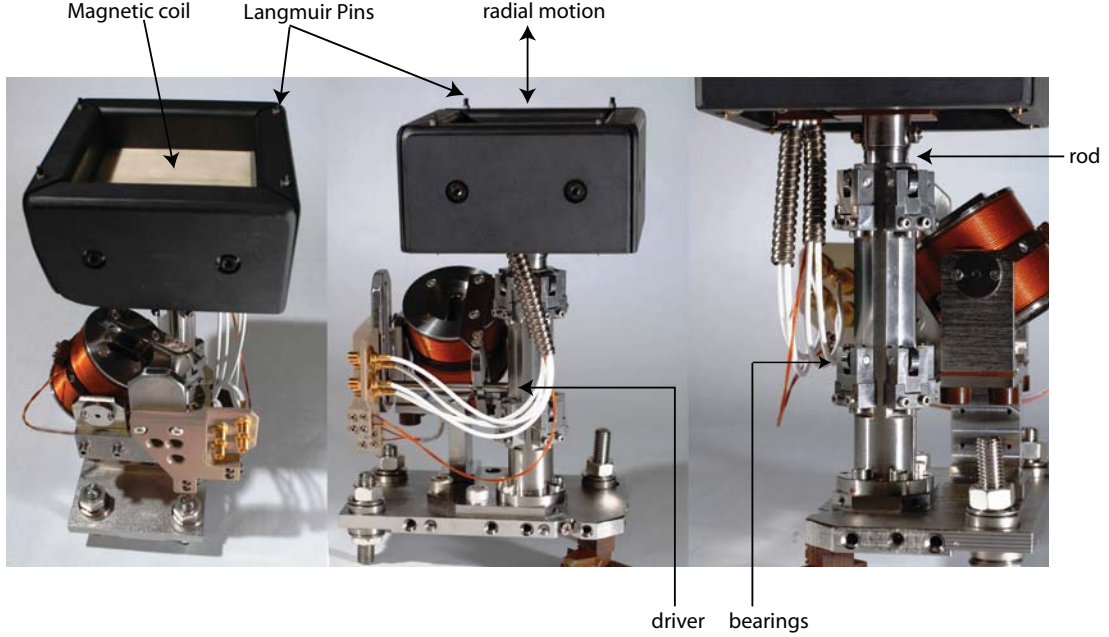


**Figure 4.1:** Pictures of the filament probe (2006 version) showing the graphite head with the 4 Langmuir pins and the driving mechanism.

The mounting mechanism consists of a base plate and the driving mechanism. The position of the base plate can be smoothly varied to fine tune the position of the probe with respect to the limiters. A cylindrical tube with two sets of four grooved ball bearings is mounted on the base plate. The bearings hold a rod, which plunges into the cylindrical tube. The probe head is mounted on top of this rod, so that the probe head and the rod move together with respect to the cylindrical tube and the base plate. A spring inside the tube permanently drags the rod into the tube and, therefore, keeps the probe head in a safe position behind the limiters without an external force. The magnetic drive has to compete against the spring and, if activated, pushes the rod out of the tube and moves the probe towards the plasma. Start and end position of this motion define the range of the drive. The range is determined by the chosen leverage, and can, in principle, be freely adjusted to experimental requirements. In our case, drive and leverage have been designed to have a range of 50 mm, but the range has afterwards been restricted to 40 mm by introducing additional blocking elements to fine-tune the end position of the probe head.

The probe head of the initial 2006 version consists of 4 Langmuir probes and a magnetic coil, measuring the time derivative of the radial component of the magnetic field,  $\dot{B}_r$ , in between. The Langmuir probes are located at the corners of a rectangle defined by the dimensions of the magnetic coil in between. The distances between the Langmuir probes are 114 mm in toroidal direction and 84 mm in poloidal direction. They are operated in Isat mode at sampling rates of 2 MHz, which will be sufficient to detect filament

rotation up to several 10 km/s. The Langmuir probes are mounted 30 mm in front of the magnetic probe on four graphite tiles, which protect the magnetic pickup coil and stick 5 mm out of the graphite tiles. The tiles are not directly connected to each other in order to prevent circular currents which would screen the magnetic coil. The design of the magnetic coil is equal to the other magnetic ballooning coils in ASDEX Upgrade [79], except for the additional protecting graphite tiles.

#### 4.1.2 Magnetic Drive

A magnetic drive serves to push the rod and the probe head mounted on the rod towards the plasma, competing with the retracting spring and the friction in the system. Energizing the magnetic drive requires only an electric feedthrough to the vacuum vessel. Therefore, the probe can be easily installed or removed from the vacuum vessel compared to other mechanisms. Furthermore, it can also be installed at positions which are not suitable for mechanical drives.

The underlying principle (see fig. 4.2) is the alignment of a magnetic moment  $\mu$  with an external magnetic field. This gives a torque  $\mathbf{D} = \mu \times \mathbf{B}$ , which can be translated

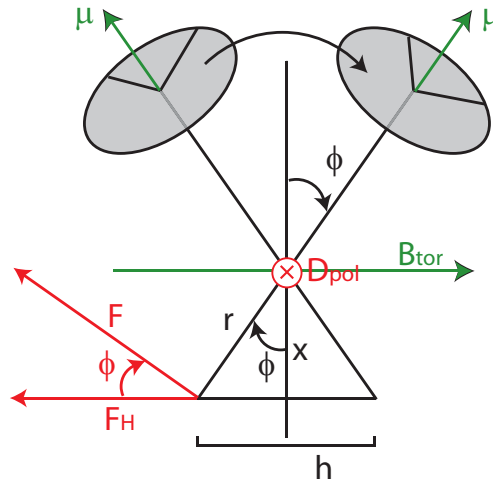


**Figure 4.2:** Principle of the magnetic drive: an energized coil forms a magnetic moment  $\mu$  which aligns with an external magnetic field  $\mathbf{B}_{\text{tor}}$ . This results in a torque  $\mathbf{D} = \mu \times \mathbf{B} = \mathbf{F} \times \mathbf{r}$ , which can be translated into a force  $\mathbf{F}$ .  $\mathbf{F}$  can be directed into any direction in the radial-toroidal plane by choosing an appropriate leverage.  $\mathbf{F}$  points toroidally in this scheme, but radially in the experiment.

into a radial motion of the probe with an appropriate leverage. The same principle has already been used to build rotating drives [80], as well as linear drives for single probes [81]. The magnetic moment  $\mu$  can be generated by an energized coil, which will rotate around its axis in order to align the magnetic moment  $\mu$  with the external magnetic field  $\mathbf{B}$ . We use only the toroidal component of the magnetic field, which is by a factor of  $>5$  the major component. The other components give a torque which is absorbed by the bearings.

The torque of such a drive depends on the cross section area  $A$  of the coil, the number of windings  $N$ , the electric current  $I$ , and the external magnetic field  $B_{\text{tor}}(R)$  at the location of the probe. Considering only the toroidal component of the magnetic field,

the resulting torque is

$$D_{pol} = IANB_{tor}(R) \cos \phi, \quad (4.1)$$

where  $\cos \phi$  denotes the fraction of the magnetic moment perpendicular to the toroidal magnetic field. With a lever of length  $r$ , this torque translates into a force  $F = D_{pol}/r$ . The length  $r$  is determined by the required range of the radial motion  $h = 50$  mm and the maximum rotation angle  $\phi_{max}$  of the coil. To translate the rotation of the coil into a linear motion of the rod, we have applied a driving lever to the coil, which works together with a driver fixed to the rod in such a way that the point of application moves along a straight line (see fig. 4.2). Additional guidance and ball bearings allow smooth operation of the driving lever and the driver under vacuum conditions and prevent seizing. With this construction, the length  $r$  of the lever will change with  $\phi$ :  $r = r(\phi)$ , with  $\phi$  ranging from  $-\phi_{max}$  to  $\phi_{max}$ . With  $\cos \phi = x/r(\phi)$  and  $\tan \phi_{max} = 0.5 h/x$ , we can calculate the length of the lever

$$r(\phi) = \frac{h/2}{\tan \phi_{max} \cos \phi}. \quad (4.2)$$

The resulting force  $F$  is then

$$F = \frac{D}{r(\phi)} = IANB_{tor}(R) \frac{\tan \phi_{max} \cos^2 \phi}{h/2} \quad (4.3)$$

and the component  $F_H$ , which causes the radial motion of the probe, is

$$F_H = F \cos \phi = IANB_{tor}(R) \frac{\tan \phi_{max} \cos^3 \phi}{h/2}. \quad (4.4)$$

From eq. (4.4), we can see that  $F_H$  has a minimum for  $\phi = \pm \phi_{max}$ . As the probe will start its motion at  $\phi = -\phi_{max}$ ,  $F_H(\phi_{max})$  has to be high enough to overcome friction and the force of the retracting spring. The crucial value for  $F_H(\phi_{max})$  has been estimated to be about 50 N in our case.

Fig. 4.3 shows the  $\tan \phi_{max} \cos^3 \phi$  term for  $\phi = \phi_{max}$  and  $0^\circ \leq \phi_{max} \leq 90^\circ$ . The

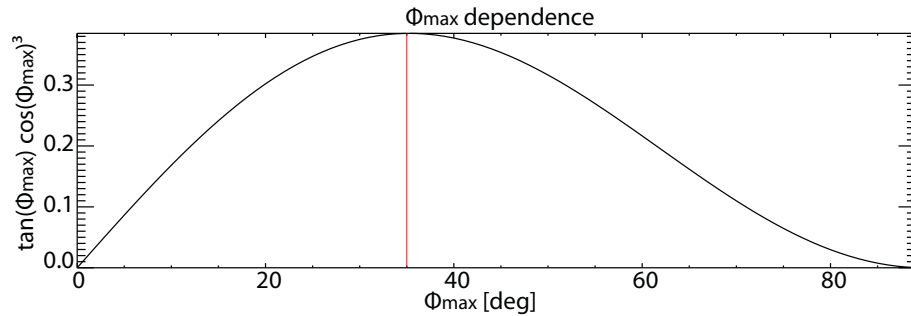


**Figure 4.3:** Dependence of the minimum force of the magnetic drive on the maximum rotation angle  $\phi_{max}$  according to eq. (4.4).  $F_H(\phi_{max})$  determines the initial probe movement and is maximised for  $\phi_{max} = 35^\circ$ .

function has a maximum for  $\phi_{max} = 35^\circ$ , which means that for this value, the highest starting force can be obtained. Choosing this maximum rotation angle  $\phi_{max} = 35^\circ$  determines the length of the lever to be  $r(35^\circ) = 44$  mm or  $r(0^\circ) = x = 30$  mm,

respectively.

With our constraints  $F_H(\phi_{max}) \geq 50$  N,  $h = 50$  mm, and a magnetic field  $B_{tor}(R) \approx 0.8B_{tor}$ , we can now calculate the product of coil size and current from eq. 4.4, assuming  $|B_{tor}| > 2$  T for most discharges:

$$IAN \geq 2.0 \text{ Am}^2 \quad (4.5)$$

### 4.1.3 Heat Production of the Magnetic Drive

As the coil is being operated in a vacuum vessel where there is no efficient cooling mechanism, the temperature rise in the wires of the coil due to resistivity becomes a crucial point. The power dissipation  $P$  inside the wire is

$$P = RI^2 = \rho_{el} \frac{l}{r_i^2 \pi} I^2 \propto I^2 r_i^{-2}, \quad (4.6)$$

where  $\rho_{el}$  is the electric conductivity and  $r_i$  the radius of the conductor of the wire. With the heat capacity

$$C = C_{cond} + C_{ins} \quad (4.7)$$

$$= [c_{cond} \varrho_{cond} r_i^2 + c_{ins} \varrho_{ins} (r_a - r_i)^2] \pi l, \quad (4.8)$$

where  $c$  are the specific heat capacities of conductor and insulator,  $\varrho$  the mass densities,  $r_a$  the total radius of the wire including insulation, and  $l$  the length of the wire. The power dissipation (4.6) leads to a temperature rise

$$\Delta T = \frac{Pt}{C}, \quad (4.9)$$

which is approximately proportional to  $I^2 r_i^{-4} t$  if we neglect the insulation. Therefore, doubling the diameter of the wire will approximately reduce the temperature rise by a factor of 16. Therefore, a relatively thick wire with a copper conductor ( $r_i = 0.23$  mm,  $c_{cond} = 385$  J/kgK,  $\varrho_{cond} = 8920$  kg/m<sup>3</sup> and  $\rho_{el} = 17.8$  nΩm) and a KAPTON insulation ( $r_a = 0.39$  mm,  $c_{ins} = 1090$  J/kgK, and  $\varrho_{ins} = 1420$  kg/m<sup>3</sup>) has been chosen. Wires of this type have already been used in the ASDEX Upgrade vessel before and are able to withstand high temperatures, in particular the vessel baking procedure (150°C). Although the wire is able to withstand even higher temperatures, we have set a limit to the probe drive of 160°C during normal operation. With eq. (4.9) and the values given above, we expect a temperature rise for the wire of 3.85°C/s with a current of 5 A, and, after 10 s, a moderate rise in the order of 38.5°C. Choosing a wire with only half the size would result in a temperature of 600°C after 10 s of operation.

Measurements with infrared thermography in air at room temperature have been carried out to study the temperature rise in practice (see fig. 4.4). According to these measurements, applying a current of 5 A for 60 s will not damage the wire and result in temperatures of less than 140°C. The vacuum behaviour can be estimated from a linear extrapolation of the low-temperature behaviour in these measurements, where convective cooling can be neglected. The extrapolation yields a temperature rise in the order of 3.4°C/s, pretty close to the expected values. During a 10 second discharge, we therefore expect temperatures to remain well below 150°C. Reaching the limit would require operation of the drive for more than 40 s. The power supply will therefore be



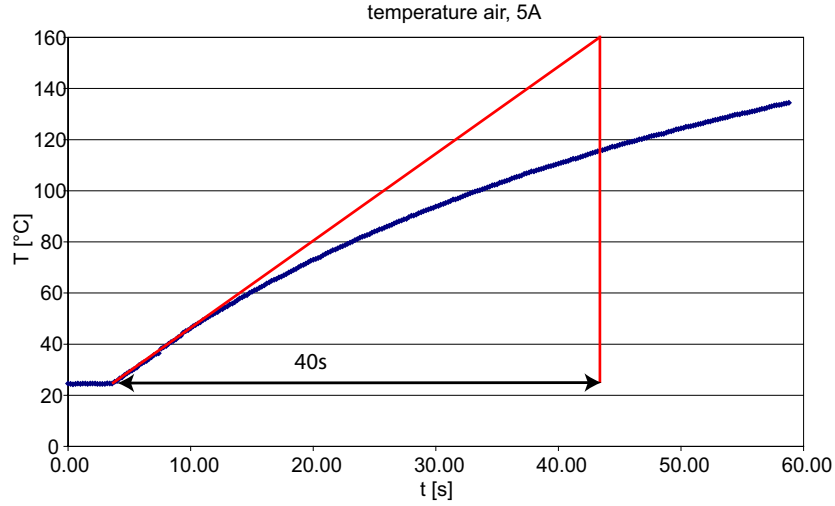


**Figure 4.4:** Thermographic measurement of the temperature rise in the probe drive in air at a current of 5 A (blue line). The vacuum behaviour can be extrapolated from the low temperature behaviour (red line). Critical temperatures will only be reached after 40 s of operation.

automatically shut down after 30 s of operation using remote switchable power switches to prevent overheating of the wires.

After ensuring the functionality of the drive over a complete ASDEX Upgrade discharge, the question arises as to whether the drive can be operated on consecutive discharges, i.e., whether the cooling down time is less than 20 min. Fig. 4.5 shows a direct measurement of the electric resistivity of the coil for 2 consecutive ASDEX Upgrade discharges ( $I = 4$  A for 7 s), which can be used as an indicator for the temperature of the wire. We can clearly see that the resistivity in both cases reaches approximately the starting value of  $6.155\Omega$  within 20 min. The second discharge indicates slightly higher temperatures (the maximum values differ due to moderate time resolution), but, as higher temperatures lead to better heat transport, we do not expect the coil to overheat even during a series of consecutive discharges. From 2007 on, the power consumption of the drive has been recorded, so that heating up of the drive could be checked directly.

Putting a current of up to 5 A into eq. (4.5), the coil size to reach the required minimum force discussed above can be calculated to be

$$NA \geq 0.40 \text{ m}^2. \quad (4.10)$$

The coil has been restricted to a diameter of 58 mm and a length of 44 mm (including a 6.5 mm broad axis) to fit in the space behind the probe head. Using a vespel coil body with a diameter of 48 mm allows for 266 windings of the 0.78 mm thick wire in 6 layers. With these numbers, a cross section of  $A_{total} = NA\bar{r}^2\pi = 266 \cdot (26.6 \text{ mm})^2\pi = 0.59 \text{ m}^2$  could be obtained, which is about 1.47 times the requested cross section. The minimum force  $F_H(\phi_{max})$  of our drive is therefore 72 N, and the maximum force is 133 N as shown in fig. 4.6. In order to reduce the thermal load, the probe drive has, in most cases, been operated with a current of only 3.5 A, which was enough to reliably move the probe in discharges with a toroidal magnetic field of 2 T. In 2007, the power supply



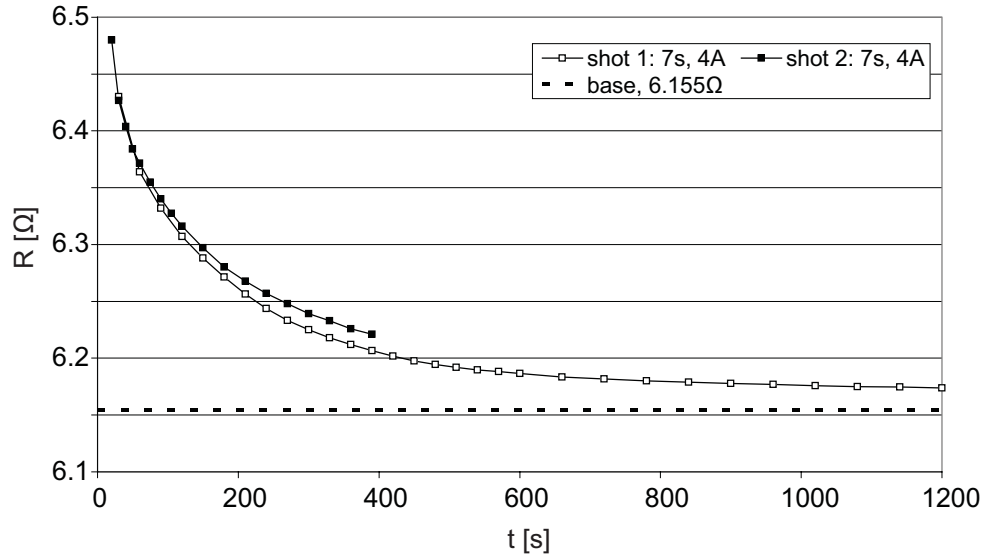


**Figure 4.5:** Time traces of the resistivity of the wires of the magnetic drive after two consecutive discharges which were 20 min apart. The resistivity curves indicate that the drive cools nearly to its starting temperature. The second discharge indicates only a slight increase in temperature, which is due to the reduced heat transport at low temperatures. Critical high temperatures are, nevertheless, reduced quickly.

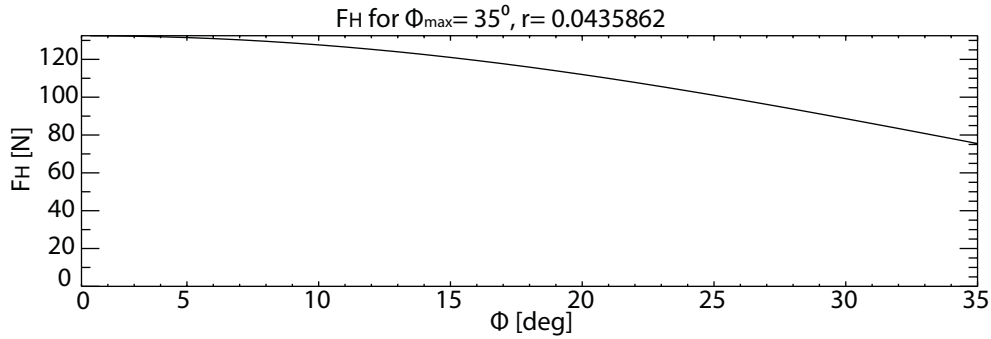


**Figure 4.6:** Resulting force of the magnetic drive for  $\phi_{max} = 35^\circ$ ,  $h = 50$  mm,  $B_{tor} = 2$  T,  $NA = 0.591$  m<sup>2</sup>, and  $I = 5$  A.

has been controlled by a shotfile-based software, which allows for a smooth ramping of the current to reduce wear of the drive and to prevent the mechanism from damage.

#### 4.1.4 Test of the Magnetic Drive

In several discharges, the filament probe has been observed with fast infrared thermography cameras. In #21265, an attempted discharge which did not reach sustained breakdown and, therefore, had no plasma but a full toroidal field of 2 T, the motion of the probe head has been measured with a frame rate of 833 Hz and high sensitivity.

This allows to make use of the different, material-dependent emissivities in the field of view: probe head and background yield homogeneous but different values, resulting in a sharp decay of the signal at the edge of the probe head in front of the homogeneous background. The position of the probe has been derived by integrating the values along a line parallel to the motion of the probe head and its trailing edge. As both the probe head and the background could be accounted as 2 homogeneous regions with different values, the line integral can be used to measure the position of the probe head. The derived motion can be seen in fig. 4.7. The probe drive has been activated

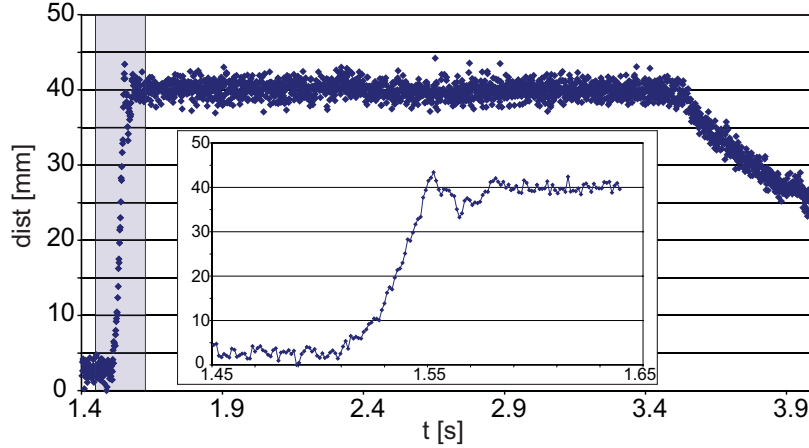


**Figure 4.7:** Position of the probe head, derived from an 833 Hz infrared thermography view. The probe starts in a safe position behind the limiters, then moves radially forward within 0.05 s and rebounds back from the front stop. The backward motion is slower, in the order of 500 ms. Using a harder spring will reduce the impact at the front stop and give a faster backward motion. The inlay shows the forward motion in more detail.

from 1.5 to 3.5 s in this discharge with a current of 3.5 A. The forward motion of the probe head happens very quickly within 0.05 s and with a small rebound at the outermost position, whereas the backward motion, driven only by the retracting force of the spring, was much slower (500 ms). The drive moves the probe forward with a velocity of  $40 \text{ mm}/0.05 \text{ ms} = 0.8 \text{ m/s}$  and has been reliably operated during the 2006 ASDEX Upgrade campaign.

For the 2007 campaign, the probe has been equipped with a harder spring, which is sufficient to move the probe backwards completely, and which reduces the hard impact at the front position together with the smoother current ramping: Feeding the power supply with predefined voltage-time series allows a smoother motion of the probe. If necessary, there would be the possibility to change move the probe actively backwards by changing the polarity of the current at given times.

#### 4.1.5 Probe Head

The probe head is mounted on the driving mechanism which has been described above. It consists of a magnetic pickup coil with a size of  $60 \text{ mm} \times 65 \text{ mm}$ . The coil points into the radial direction and thus measures  $\dot{B}_r$ , the time derivative of the radial component

of the magnetic field. The Langmuir pins are mounted next to the probe and point radially towards the plasma. The pins have a ceramic cover and are inserted in holes in surrounding graphite tiles (see fig. 4.8 for the 2006 version, and fig. 4.9 for the 2007

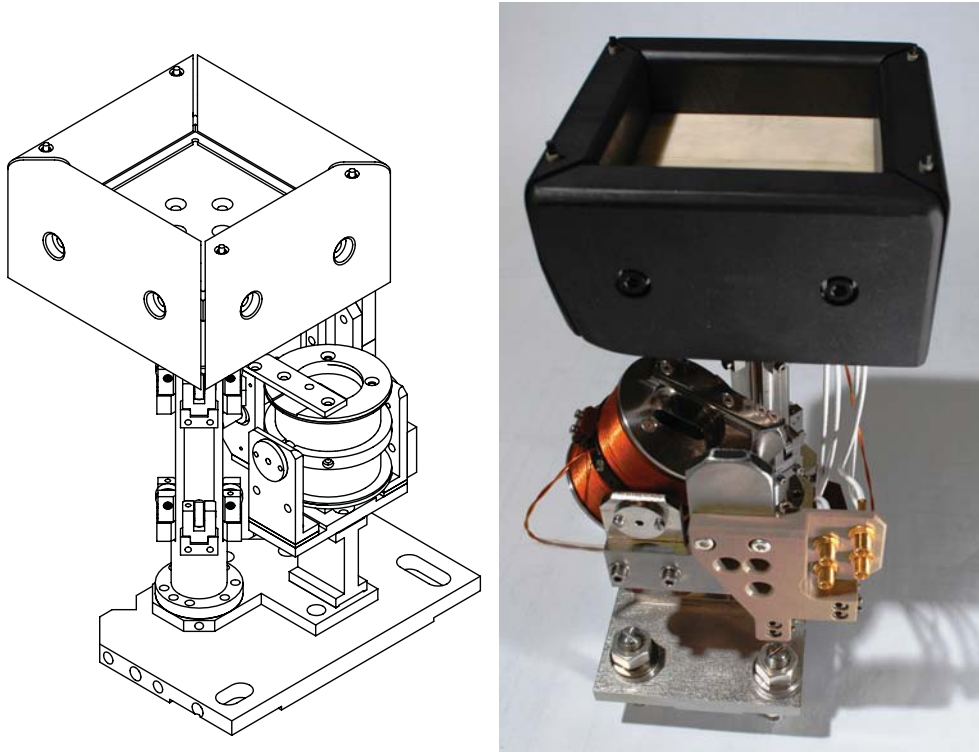


**Figure 4.8:** Technical drawing and image of the filament probe as of 2006. The probe head has 4 Langmuir pins, which stick 5 mm out of the graphite tiles and have a ceramic coating covering the lower 2 mm.

version).

After the 2006 campaign, the probe has been completely revised with the following changes:

- The number of pins has been increased from 4 to 9 to improve poloidal resolution (1 pin) and to get information on the radial dynamics (4 pins). See the following sections for details.
- The driving mechanism has been encased by solid metal plates to shield radiation.
- A harder spring has been used to improve forward and backward motion as described in section 4.1.4.
- Changed pin design: The pins in the 2006 version stuck out 3 mm of the ceramic cover, which stuck out 2 mm of the graphite tile (see fig. 4.10). During plasma operation, some of the ceramic cover broke, so that the pins were exposed to the plasma over a length of 5 mm, which led to rapid overheating and, consequently, destruction of these pins.

For the 2007 campaign, the ceramic cover and the graphite pin were drawn further backward, so that the ceramic cover does not stick out of the graphite tile. The

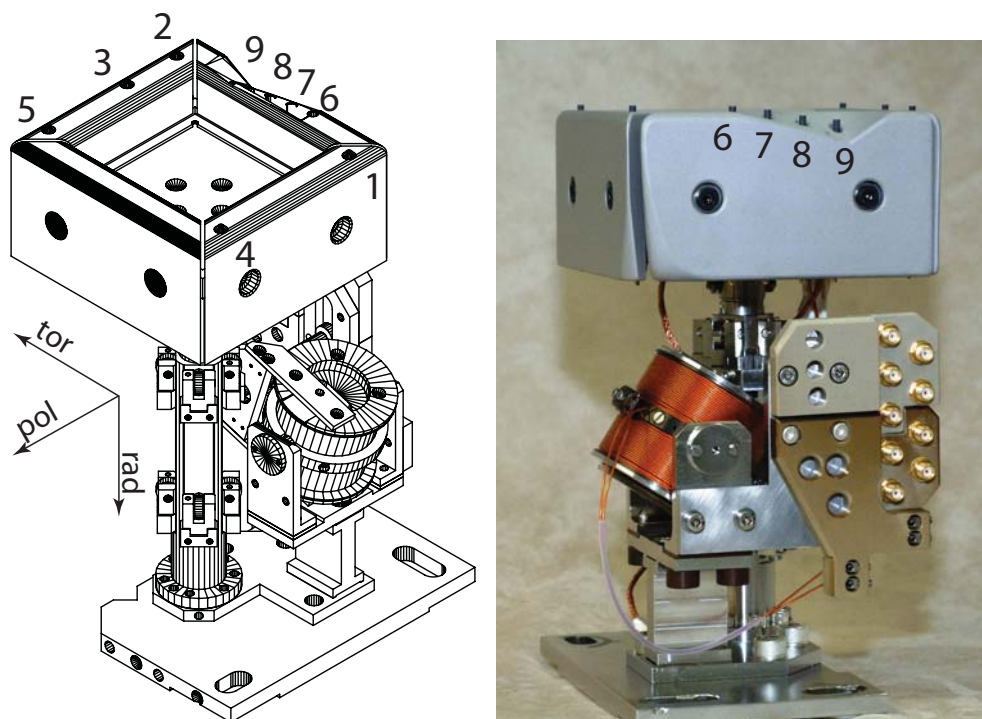


**Figure 4.9:** Technical drawing and image of the filament probe as of 2007. The probe head has now 9 Langmuir pins, which stick 2 mm out of the tungsten covered graphite tiles. The coating has been necessary to comply with the transition of ASDEX Upgrade from a carbon machine to a tungsten machine.

wetted area of the pins has been reduced from 3 mm to 2 mm with a pin diameter of 2.8 mm in both cases. This has greatly improved the durability of the Langmuir pins.

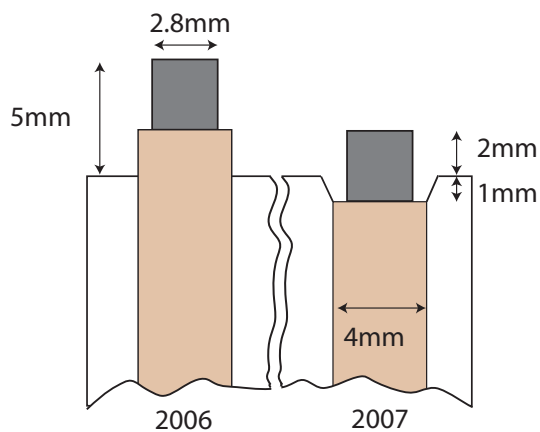


**Figure 4.10:** Illustration of the changes in the pin design from 2006 to 2007. Both pin and ceramic coating were drawn back towards the graphite tile to withstand higher heat loads.

- The graphite tiles have been covered with tungsten to comply with to the transition of ASDEX Upgrade from a carbon machine to a tungsten machine [82, 83].
- The probe drive has been equipped with a smart control of the power supply for the drive. The current through the coil can be varied at a rate of 10 Hz and several strokes can be performed per discharge. The timing can be changed in between shots, which greatly enhances the usability of the drive, as parameters and timing can now be adjusted to the current shot program within few minutes. The status of the power supply is measured with 10 Hz and the data are stored into an ASDEX Upgrade shotfile under the diagnostic TOE.

## 4.2 Midplane Manipulator

The midplane manipulator is a device which allows for easy installation of various probes during an experimental campaign. The probes can be changed on a day-to-day basis and are typically operated for several consecutive shot days in order to condition the probes, to check the wiring, etc.

The radial position of a probe can be varied on a shot-to-shot basis in mm steps and during the discharge by a pneumatic drive, which allows a fast radial motion of the probe (10 cm forward and backward in 0.1 s). Usually, up to 4 of these strokes are performed during one discharge. The fast drive allows the probe to penetrate deeper into the plasma (i.e., to get closer to the separatrix) as would be possible with a stationary probe.

For this thesis, 3 different probes have been used:

- Dual Magnetic probe: A probe with 2 3D coilsets at different radial positions (fig. 4.11, top). A 3D coil set consists of 3 nested magnetic probes, which allow to measure all 3 components of the magnetic field at the same position.
- Combined Magnetic-Langmuir probe: (fig. 4.11, bottom). This is a probe, which has been designed especially for measurements close to the separatrix. The probe carries 10 Langmuir tips at the front of a carbon hood, arranged in two columns of 5 pins and divided by a septum in between. In the back, the probe carries a 3D coil set, which is located at about 9 cm from the Langmuir tips because of the wiring of the Langmuir pins.

This probe has in particular been used for filament studies, for flow measurements [84], and for radially resolved magnetic measurements [40].

For 2007, a tungsten covered cap has been used to reduce carbon influx into the machine. The cap has been slitted in the back to reduce mirror currents, but the magnetic signal from this head was far worse than from the graphite head. The use of isolating materials should therefore be checked for more accurate measurements, even though previous experiments have shown problems with these materials.

- Langmuir probe: The same probe as the Magnetic-Langmuir probe, but without magnetic coil in the back.

The midplane probes are limited in size by the vacuum feedthrough and thus are restricted to a diameter of 60 mm. This limitation makes the midplane manipulator probes unsuitable for measurements of the filament rotation velocity. With a pin distance of 1 cm and a velocity of 1000 m/s, the time delay would be  $10^{-5}$  s, which is only

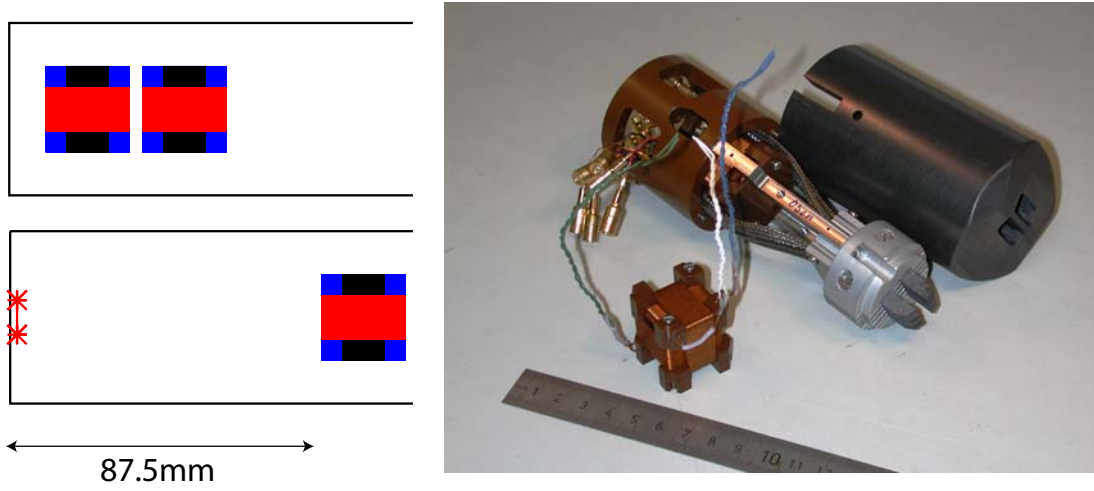


**Figure 4.11:** Left: Midplane manipulator probes used in the frame of this thesis: Double magnetic probe with 2 3D coilsets (top) and the combined Magnetic-Langmuir probe (bottom). Right: Image of the combined Magnetic-Langmuir probe.

20 samples at a sampling rate of 2 MHz. The new filament probe has much bigger dimensions and is therefore better suited for measurements of the rotation velocity. The midplane manipulator probes in turn are better suited for measurements of the filament fine structure.

For the measurement of radial dependencies, dedicated discharges have been tailored in which both the radial position of the midplane probe and the radial position of the plasma edge has been varied. Fig. 4.12 shows time traces for both quantities during an ASDEX Upgrade discharge. Using this scheme, the distance between probe and sepa-

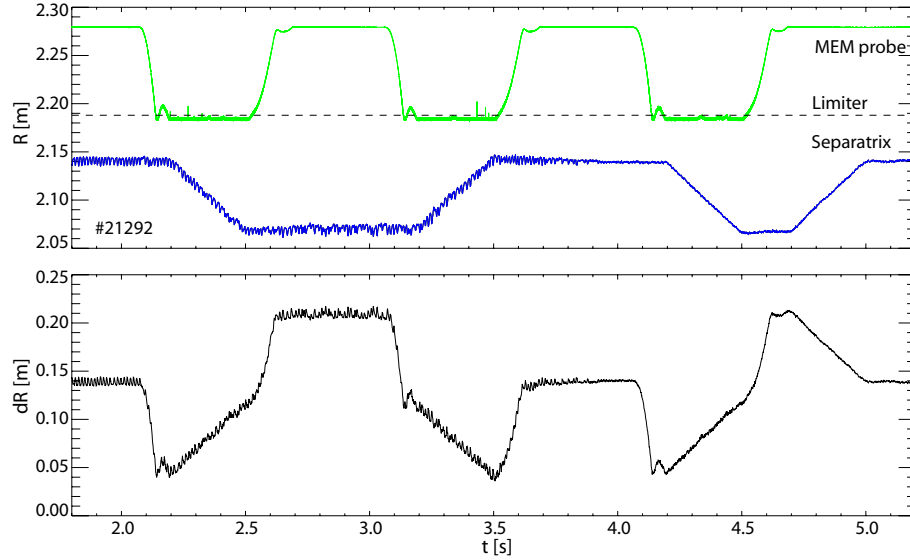


**Figure 4.12:** Top: Radial variation of the separatrix position and the position of the midplane manipulator probe to study the radial parameter dependence. Bottom: Distance of the separatrix to the front of the midplane manipulator probe.

matrix can be varied from 5 cm to 15 cm (limited by the ICRH-limiters). The plasma parameters (especially the energy content of the plasma) have been kept constant as much as possible.

### 4.3 Infrared Thermography

Infrared thermography is an optical method to measure surface temperatures. The number of photons emitted from a surface at a wavelength  $\lambda$  is measured. It is described by Planck's law,

$$M_b(T, \lambda) = \frac{2\pi c}{\lambda^4} \frac{1}{e^{hc/kT\lambda} - 1}, \quad (4.11)$$

which describes the emission of a black body of temperature  $T$  at wavelength  $\lambda$ . A black body is an ideal body that absorbs all electromagnetic radiation that falls onto it. The black body emits the radiation again with wavelengths and amplitudes determined by the temperature of the black body as described in eq. (4.11). Fig. 4.13 shows the emittance of such a black body at different wavelengths and temperatures. The

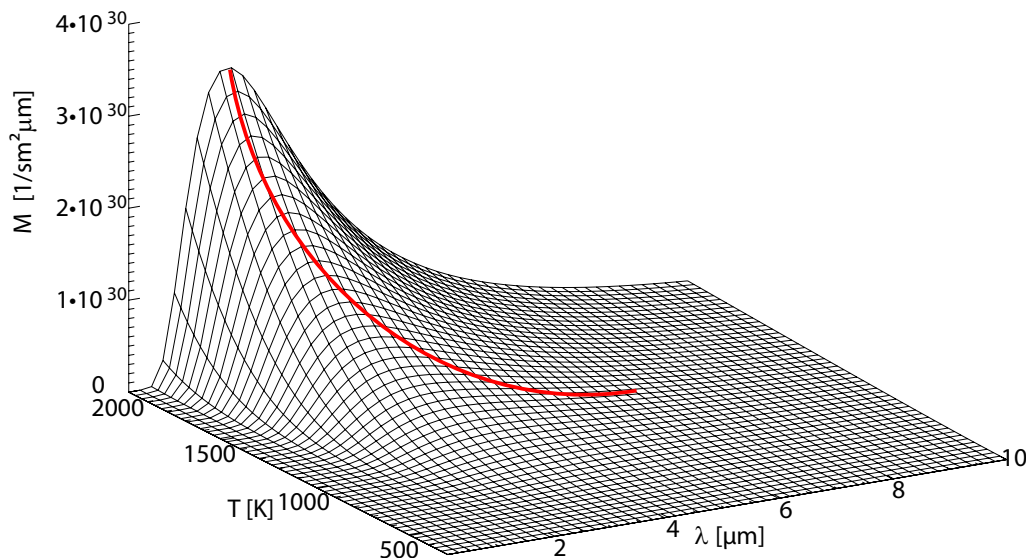


**Figure 4.13:** Emittance of an ideal blackbody at different temperatures and wavelengths. The maximum of the emittance is described by Wien's displacement law, eq. (4.13) (red line).

emittance  $M_{real}$  of real bodies is always below that of an ideal black body. The ratio between real and ideal emittance is the emissivity  $\epsilon$ ,

$$M_{real}(T, \lambda) = \epsilon(T, \lambda) \cdot M_b(T, \lambda), \quad (4.12)$$

which can be dependent on both wavelength and temperature.

The maximum of the emittance  $M_b$  is described by Wien's displacement law,

$$\lambda \cdot T = 2897 \mu\text{mK} \quad (4.13)$$

For room temperature, the maximum emittance occurs at  $10 \mu\text{m}$ . At about 900 K, the intensity of photons emitted in the visible range is high enough to be detected by the



human eye. The infrared cameras on ASDEX Upgrade are sensitive to wavelengths in the range of  $3.5 - 5.1 \mu\text{m}$ .

From fig. 4.13, it is obvious that the photon flux at a fixed wavelength varies strongly nonlinear with temperature: increasing the temperature from room temperature to 900 K will raise the emittency at  $4.7 \mu\text{m}$  by more than a factor of 100. Therefore, measurements require a large dynamic range and good sensitivity. The sensitivity  $\partial_T M$  increases with higher temperatures due to the nonlinearity of the photon flux. Fig. 4.14 shows temperature which is necessary to switch the least significant Bit of a 14 Bit ADC for 5 given maximum temperature ranges. To maximise the sensitivity in our measure-

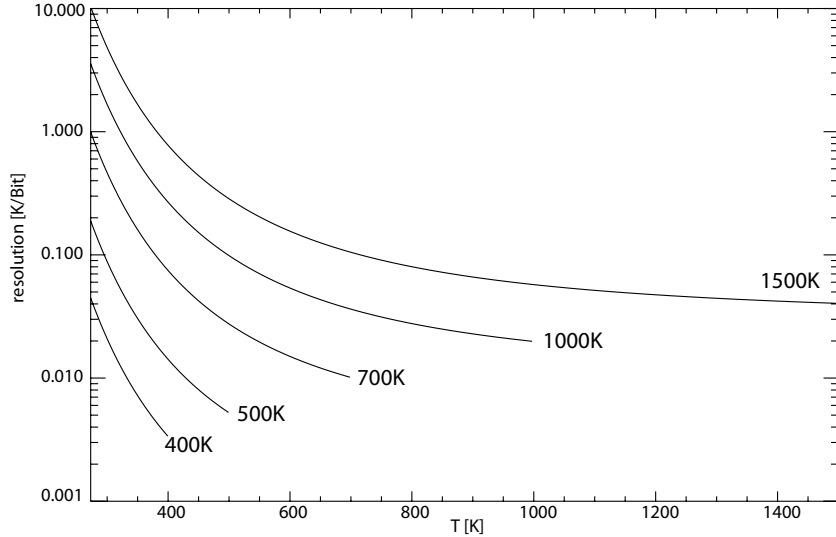


**Figure 4.14:** Temperature change necessary to set the least significant bit of a 14 Bit ADC for different dynamic ranges.

ments and to get a good exploitation of the 14 Bit dynamic range, the integration time of the detector had to be adapted to the expected temperatures.

In the course of this thesis, two different 2D infrared cameras have been used. Both cameras work in a snapshot mode, so that the whole array of pixels is exposed simultaneously. The exposure time can be chosen from a minimal value up to the inverse frame rate. The maximum frame rate depends on the chosen size of the two-dimensional pixel array:

	Santa Barbara	Thermosensorik
integration time	$> 4 \mu\text{s}$	$> 4.5 \mu\text{s}$
array size (max)	$256 \times 320 \text{ px}$	$256 \times 256 \text{ px}$
frame rate	315 Hz	884 Hz
array size (min)	$8 \times 128 \text{ px}$	$8 \times 8 \text{ px}$
frame rate	8 kHz	25 kHz

For the detection of small structures such as filament footprints, a good spatial resolution is required because of the problem of averaging over gradients as photon-emission is highly nonlinear. The heat flux calculation is carried out with the heat flux code THEODOR [85, 86] from the temperature change, not from absolute temperatures. The cameras were calibrated in the lab using black body radiators. Whereas the gain



factor shows no temporal drift, the offset has to be corrected from time to time. This has either been done by a 1-point calibration or by using the first frame of a discharge as reference frame. This takes into account the optical geometry, the electronics and detector response as well as the background signal. However, the emissivity is treated as constant in this case:  $\epsilon(T, \lambda) = \epsilon(\lambda)$ .



## Chapter 5

# Filament Motion Measurements

The filament probe has been designed for measurements of the filament rotation velocity. Fig. 5.1 shows the view from the plasma onto the probe head. In this view, only

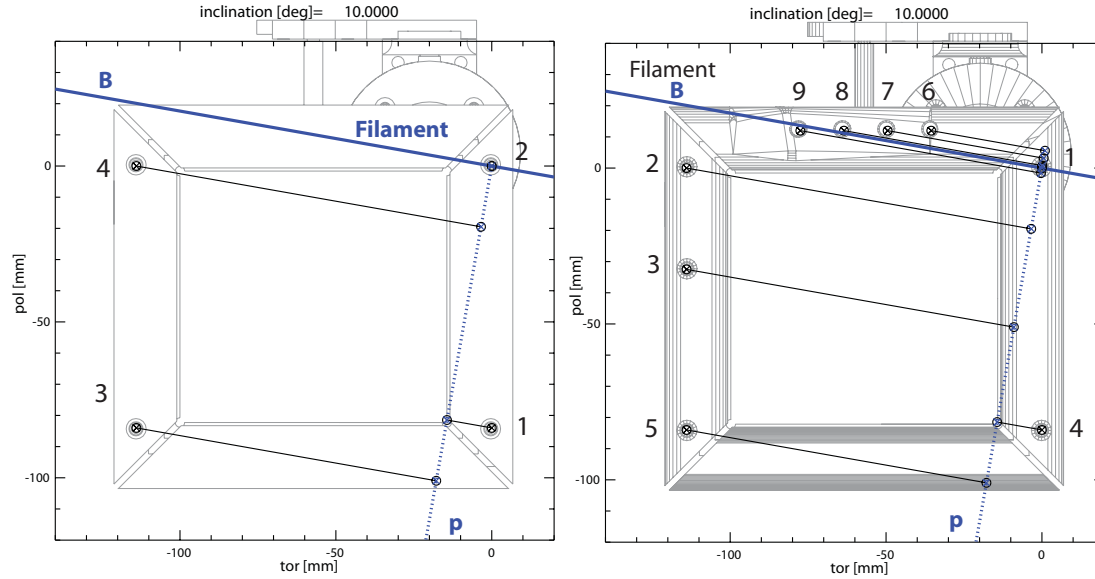


**Figure 5.1:** Technical drawing of the filament probe head (left: 2006, right: 2007 version). The pin positions have been mapped to  $\mathbf{p}$  with  $\mathbf{p} \perp \mathbf{B}$  in order to calculate the distance between the pins perpendicular to  $\mathbf{B}$ , which allows to calculate the rotation velocity of filaments by means of time delay measurements.

poloidal/toroidal rotation becomes visible, but not the radial motion. The picture on the left of fig. 5.1 shows the 2006 version of the probe head (symmetric design with 4 pins), the picture on the right shows the 2007 version (asymmetric design, 9 pins). The pin positions from the 2006 design have still been used for the 2007 version. 5 new pins have been added and the numbering has been revised. Note that pins 6-9 are at different radial positions and allow to measure the radial motion.

A blue line, schematically representing a filament, is shown in fig. 5.1, passing the probe in front of the probe head, thereby touching the Langmuir pins. The Langmuir pins are operated at constant negative voltage  $U \approx -60 \dots -120 \text{ V}$  with  $eU \gg kT_i$  [68] in order to reach the ion saturation branch and to measure the ion saturation current

$j_{i,sat} = en_i c_s$  as described in sec. 3.2. As filaments have a higher density than the surrounding background plasma, they will appear as prominent spikes in the timetraces of the Langmuir ion saturation current measurement of the pins which they have hit. The Langmuir system has a sampling rate of 2 MHz, and has briefly been described in [40]. This set-up allows for fast and spatially well-resolved measurements in the SOL.

## 5.1 Radial Motion

As has been described in chapter 3, several theories for radial filament propagation based on  $E \times B$  drift have been proposed. These models, however, result in opposing predictions, depending on the underlying damping mechanism: Sheath dissipation leads to a damping of large scale structures so that smaller filaments move faster, whereas damping through a polarization current is more effective for small scale structures, i.e. larger filaments move faster. Experimental studies of the radial propagation velocity are therefore necessary.

### 5.1.1 Diagnostic Setup

The filament probe is equipped with 4 radially separated pins for the 2007 ASDEX Upgrade campaign as shown in fig. 4.9. The radially resolving pins (numbers 6 to 9) are located at the upper tile of the filament probe head along a horizontal line, i.e. at the same  $z$  position as shown in fig. 5.1 or in an enlarged view in the upper part of fig. 5.2. The latter shows the pin position in a view from the plasma and their mapping along the magnetic field  $\mathbf{B}$ . The lower part of fig. 5.2 shows the pins in a poloidal cross section, mapped along  $\mathbf{B}$  to the same toroidal position. The poloidal variation resulting from this mapping depends strongly on the local field line inclination angle. For #22134 at 1.7 s, the field line inclination is  $8.6^\circ$ , resulting in a poloidal variation of 4 mm from pin 6 to pin 8. From visible imaging, the poloidal size of filaments seems to be in the cm range, i.e. far bigger than the poloidal variation of the pin position, so that we can neglect the poloidal variation here.

The radial distance is, for example, 3.5 mm between pin 6 and pin 8, so that the radial propagation velocity of impinging filaments can be calculated from time delay measurements. With a sampling rate of  $0.5 \mu\text{s}$ , propagation velocities of up to 7 km/s can be detected (pin 9 has not been used).

Similar plasma discharges have been carried out for these measurements. For the radial motion, we have evaluated #21866-21869 (black data points in the following figures) and #22133-22134 (brown data points). Fig. 5.3 shows timetraces for  $D_\alpha$  radiation and outer plasma radius  $R_{aus}$  for discharge #22134. The discharges had  $I_p = 0.8$  MA,  $B_{tor} = -2.5$  T, heating power of 6 – 7.5 MW and line averaged plasma densities of  $6 \cdot 10^{19} \text{ m}^{-3}$ . Density and stored energy have been held constant during  $R_{aus}$  scans, in which the plasma has been shifted horizontally by several cm in order to vary the distance between filament probe and separatrix, i.e. the distance the filaments have to travel before they hit the filament probe as indicated in sec. 4.2. Up to three strokes of the filament probe have been performed in each discharge (shaded regions in fig. 5.3) to move the Langmuir pins in front of the leading ICRH limiters. ELM frequencies of about 90 Hz have been achieved. All the ELMs during the filament probe strokes have been analysed manually for filaments as described in section 2, and a database containing 466 analysed filaments has been built.

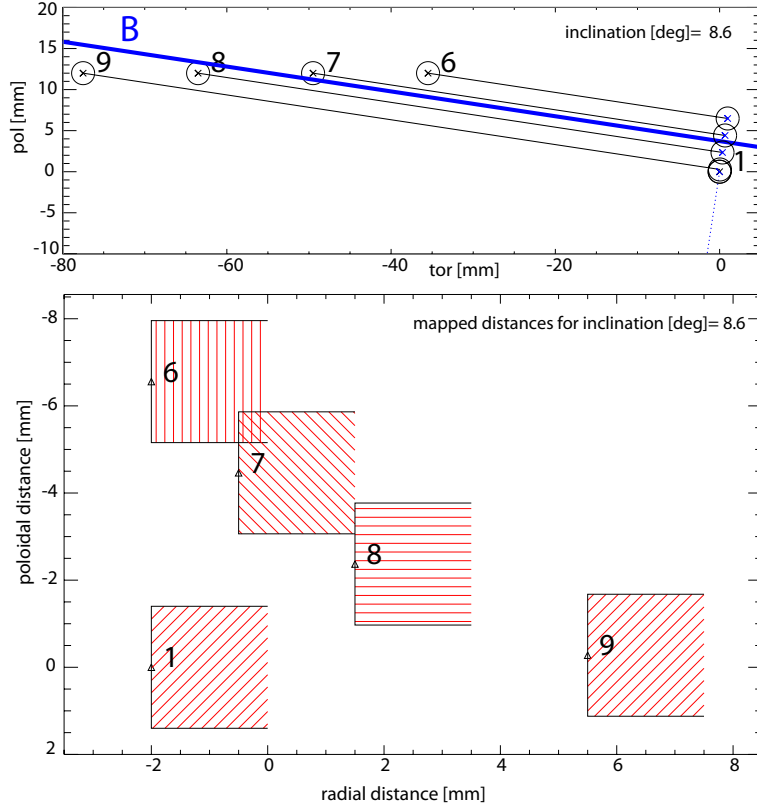


**Figure 5.2:** Position and mapping of the filament probe pins in a poloidal-toroidal plane (upper part) and in the radial-poloidal plane (lower part). The radial separation of pins 6 to 8 allows to measure the radial propagation velocity of impinging filaments by time delay measurements.

### 5.1.2 Measuring Method

The analysis of #21866-21869 is based on pins {6, 8}, whereas pins {6, 7, 8} have been used for #22133-22134. For the latter, a different set of power supplies has been used, in most cases limiting the analysis to filaments with an ion saturation current  $< 1$  A. On the ion saturation current timetraces, filaments appear as prominent spikes due to their higher density and temperature. Fig. 5.4 shows these time traces for pins 6-8 during one ELM. The signals are shifted along the  $y$ -axis according to their radial separation, so that filaments moving with constant radial velocity follow a straight line in this plot (however, even an acceleration with  $10^8$  m/s<sup>2</sup> [87] would only give negligible deviations because of the small radial distance between the pins). This feature is heavily used for finding filaments and separating them from other, uncorrelated signals on the Langmuir pins. In the ELM shown in figure 5.4, six filaments could clearly be detected. The radial velocities are determined from an enlarged view of the filament as shown in the right hand side of figure 5.4. This view is used to mark the center of a filament on two channels, and to calculate the velocity from the time delay and the corresponding radial distance. The width of the filament is then calculated by fitting a Gaussian with linear plus constant background to the data, the width given in the following being the full width at half maximum. The amplitude is taken as the maximum of the

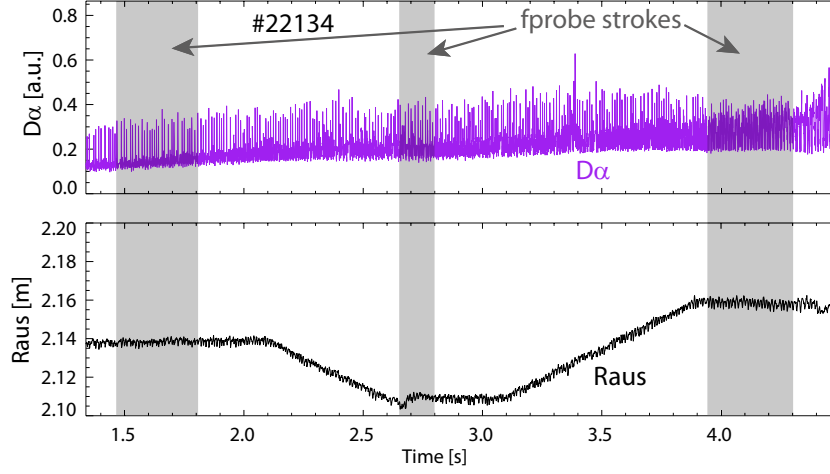


**Figure 5.3:** Outer plasma radius  $R_{ous}$  and  $D_\alpha$  radiation for discharge #22134. The variation of the outer plasma radius (from  $R = 2.11$  m to 2.16 m in this case) changes the distance the filaments have to travel to reach the filament probe. Shaded regions denote when the filament probe (motion not shown here) was in front of the leading ICRH limiters. Plasma parameters have been held constant during these  $R_{ous}$ -scans.

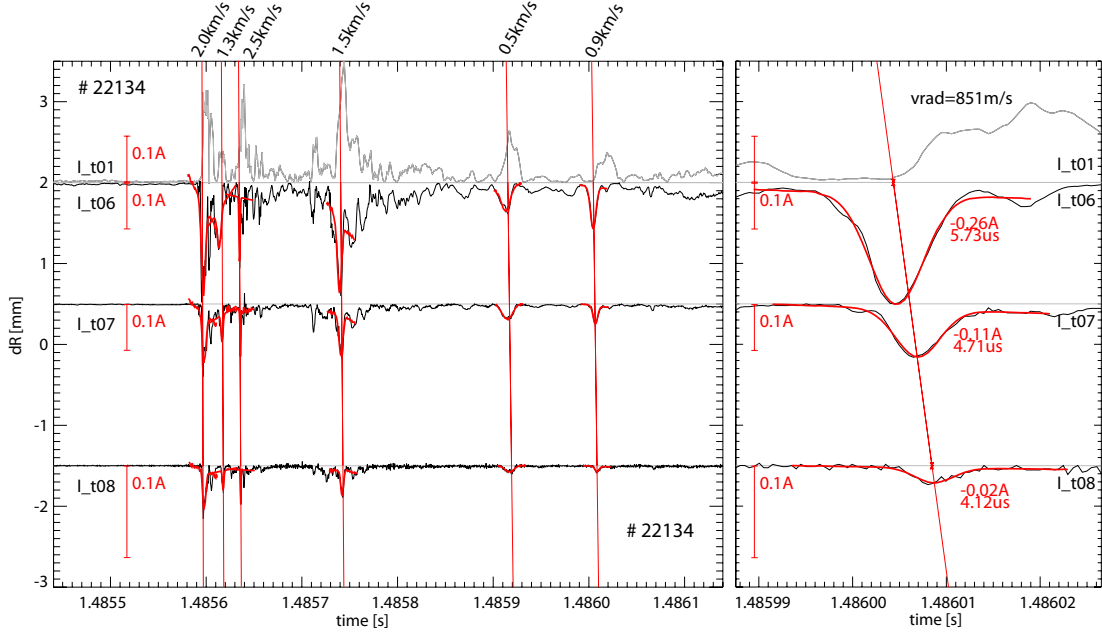


**Figure 5.4:** Langmuir timetraces during an ELM. The signals are plotted in  $y$ -direction according to their radial separation, so that filaments can be traced over the radially separated pins by straight lines. Overview of one ELM (left) and enlarged version of one filament (right).

ion saturation current in the  $30\mu\text{s}$  broad fit region. The temporal separation between filaments is usually large enough to prevent crosstalk in that method.

For each filament, the following parameters have been stored in the database:

- distance  $dR$  between filament probe and separatrix, i.e. the distance the filament has travelled before reaching the filament probe
- radial velocity  $v_{rad}$  of the filament from time delay measurements and an estimated measurement error (see below)
- peak ion saturation current
- (temporal) width  $\Delta[s]$  of the ion saturation peak

The data analysis described above leads to uncertainties in the data, which comes mostly from the determination of the position of the peaks:

- A first component comes from missing the absolute maximum of the  $I_{sat}$  peak. This happens even for sharp spikes. As we are only interested in the relative time difference between peaks on two channels, the error has been assumed to be  $\pm 0.25 \mu s$ , i.e. half of the time resolution.
- A second component comes, for broader peaks with a flat top, from the problem of identifying the real position of the center of the peak. This error has been estimated to be 0.2 times the peak width.

If the second component becomes larger than the first component, the first one has been neglected. Width and amplitude have not been assigned an error.

The database contains every structure that exceeds the noise and could be traced over at least two pins. Events that did not fulfil these requirements have not been regarded as filaments and have therefore not found their way into the database. In the following, width and size will always refer to the width and size as measured with pin 6 which is closest to the plasma.

### 5.1.3 Raw Data and Data Conversion

Fig. 5.5 shows an overview of the obtained data. Blue dashed curves have been introduced to show trends in the data: the radial velocity increases with the ion saturation current of the filament (upper part) and decreases with the temporal width (lower part). These and the following blue curves serve as upper or lower limits to the data in a sense that the number of data points changes strongly across the line. The curves are not meant as absolute limits or as envelopes but serve as a description of the distribution of the data points.

The two graphs show a large scatter in the data due to the uncertainties in the determination of the filament peak. To demonstrate this problem, we will focus on the strong outlier at  $I = 2.67 \text{ A}$  and  $v_{rad} = 1.2 \text{ km/s}$  from fig. 5.5. The time traces of the Langmuir measurements for this filament are shown in fig. 5.6. The velocity of this filament has been determined by the (assumed) center of the ion saturation current peak to be  $1.222 \text{ km/s}$ . The dashed lines denote the estimated uncertainties which yield a range  $v_{rad} = 1.03 - 1.52 \text{ km/s}$ . From fig. 5.5, filaments with such an ion saturation current should have a velocity of roughly about  $3 \text{ km/s}$ , indicated in fig. 5.6 by the blue line. The available data, however, does not allow a better velocity determination in that case, as the signals do not provide enough information (more fine structure, or better smoothness of the signal) in this case. Typically, this uncertainty has been much smaller for the other filaments and should be contained in the error bars, as the shown

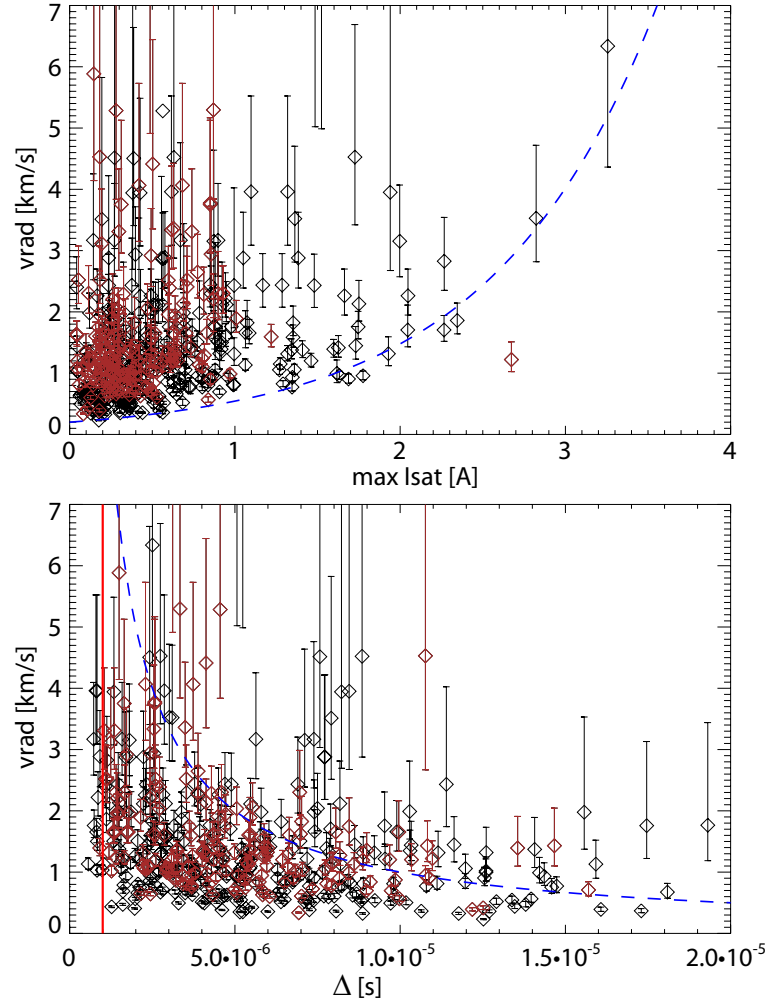


**Figure 5.5:** Raw data from a database of 466 analysed filaments. The radial velocity increases with the ion saturation current of the filament and decreases with the temporal width as indicated by the dashed lines. The red line in lower plot denotes the detection limit due to the finite sampling rate (5.1).

filament is obviously the worst outlier. Nevertheless, these uncertainties contribute to the large scatter in the data and explain why such a large number of filaments had to be analysed to derive the physical properties governing the radial motion of filaments. The red, solid line in the lower graph in fig. 5.5 describes a detection limit: filaments with a temporal width

$$\Delta[s] < 1 \mu s := \Delta_{min}[s] \quad (5.1)$$

will usually not be detected with their full amplitude due to the sampling rate of 2 MHz. The data in fig. 5.5 is only raw data and has to be translated into more meaningful numbers. First, we estimate the filament density from the ion saturation current density, which is given by the measured ion saturation current divided by the relevant pin cross-section (i.e. the pin surface perpendicular to  $\mathbf{B}$  for  $v_{rad} \ll c_s$ ),

$$j_{sat} = I_{sat}/(2d_{pin}dR_{pin}) = I_{sat}/11.2 \text{ mm}^2. \quad (5.2)$$



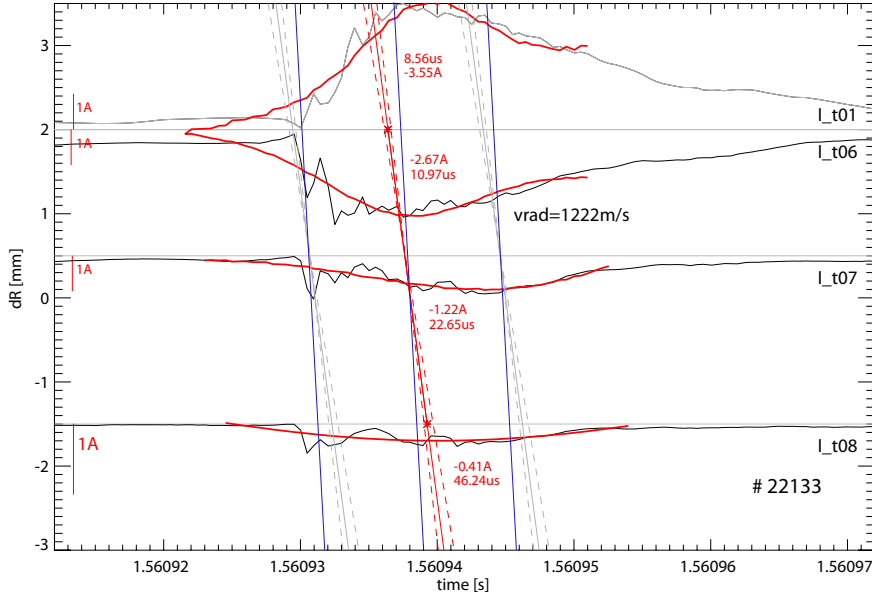


**Figure 5.6:** Time traces of the outlying filament with  $I = 2.67$  A and  $v_{rad} = 1.2$  km/s in fig. 5.5. The velocity has been determined by the (assumed) center of the ion saturation current peak. The dashed lines denote the estimated uncertainties (1.03 – 1.52 km/s). From fig. 5.5, filaments with the given current should have a velocity of roughly about 3 km/s (blue lines). The available data, however, does not allow a better velocity determination as the data does not provide enough information in this case. (5.1).

The ion saturation current itself is given by

$$j_{sat} = en_{fil}c_s \approx en_{fil}\sqrt{k(T_i + T_e)/m_i} \quad (5.3)$$

with filament density  $n_{fil}$ , sound speed  $c_s$ , and ion mass  $m_i$ . From a comparison of heat flux and ion saturation current on ASDEX Upgrade, the temperatures in a filament have been found to be nearly constant over a wide range in the far SOL and to be in the order of  $T_i = 30 - 60$  eV and  $T_e = 5$  eV [68]. This gives

$$j_{sat}/n_{fil} = ec_s = 6.6 - 9 \cdot 10^{-15} \text{ Am} \approx 8 \cdot 10^{-15} \text{ Am}, \quad (5.4)$$

so that we can translate the ion saturation current into a filament density via

$$n_{fil} = I_{sat}[A] \cdot 1.12 \cdot 10^{19} \text{ m}^{-3} := I_{sat}[A] \cdot n_{fil,0} \quad (5.5)$$

with  $n_{fil,0} = 1.12 \cdot 10^{19} \text{ m}^{-3}$ .

It should be noted that the filament density used in the following will be derived from the maximum of the peak in the ion saturation current using these equations. If the Langmuir pin hits the core of the filament, this value will correspond to the central density of the filament. If the filament hits the Langmuir pin somewhere else, the core density will be underestimated according to the density distribution in the filament.

The temporal size  $\Delta[s]$  of a filament is a measure for the time the filament takes to pass through the Langmuir pin. In order to describe the meaning of this measure, we assume a filament that moves with a radial velocity  $v_{rad}$  and a poloidal velocity  $v_{pol}$  towards

the probe (the poloidal velocity could of course be translated into a toroidal one via the field line inclination angle, see e.g. [78] for details). The filament will hit a Langmuir pin and, assuming that the interaction is too low to distort the filament, will just move on through the pin. The pin will move through the filament and measure the density of the filament along that line. The left part of fig. 5.7 shows two filaments with different poloidal extent  $\Delta_{pol}$ , a radial propagation velocity of 1000 m/s, and a Gaussian density distribution in  $R$  and  $z$ . The slope of the curve that shows the motion of the center of the filament changes with the velocity ratio  $v_{rad}/v_{pol}$ , i.e. becomes steeper for higher  $v_{pol}$ . The plots at the right of fig. 5.7 show the timetraces that would result from a

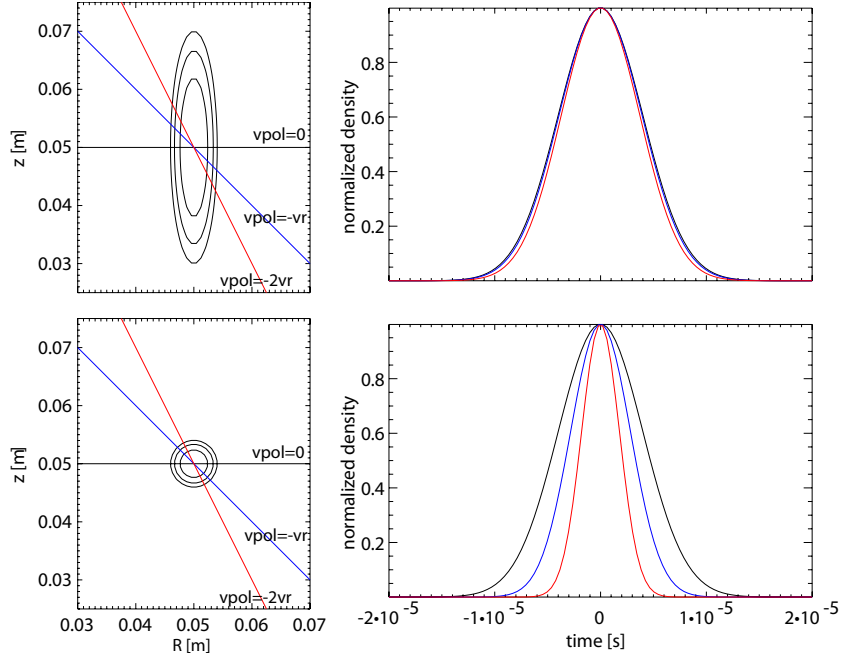


**Figure 5.7:** Dependence of the temporal peak width on the velocity ratio  $v_{rad}/v_{pol}$ . The peak width is the length of the cut of the Langmuir pin through the filament. The width of circular filaments is more affected by the velocity ratio than the width of poloidally elongated filaments.

Langmuir measurement through the filament along these lines, yielding

$$n_{fil}(t) = n_{fil,0} \exp \left( -v_{rad}^2 t^2 / 2\Delta_{rad}^2 - v_{pol}^2 t^2 / 2\Delta_{pol}^2 \right) \quad (5.6)$$

For the circular filament ( $\Delta_{rad}/\Delta_{pol} = 1$ ), the peak width changes with the velocity ratio, whereas the peak width of the elongated filament ( $\Delta_{rad}/\Delta_{pol} = 0.2$ ) is not affected by the velocity ratio. From visible imaging, one expects filaments to be elongated [42], so that we can assume the temporal peak width  $\Delta[s]$  to be independent from the velocity ratio.  $\Delta[s]$  can therefore be translated into a radial filament width  $\Delta_{rad}$  by multiplication with the radial filament velocity:

$$\Delta_{rad} = v_{rad} \cdot \Delta[s]. \quad (5.7)$$

The filament size given here is the full width at half maximum. It is thus not the total size of the filament, which is difficult to derive due to smearing by background

variations. One has to keep in mind, that different methods for measuring the filament size deliver different measures for the filament size: infrared thermography, for example, will pronounce the hotter core of the filament, as the photon flux increases strongly with temperature, see eq. (4.11). Measurements with fast cameras in the visible range, however, tend to pronounce the cold edge of a filament, i.e. its border. The numbers given here should therefore be smaller than values from visible imaging.

#### 5.1.4 Interpretation

With the translation into physical units, the filament velocity can be shown as a function of filament density and filament size, see fig. 5.8. The blue dashed lines indicate that

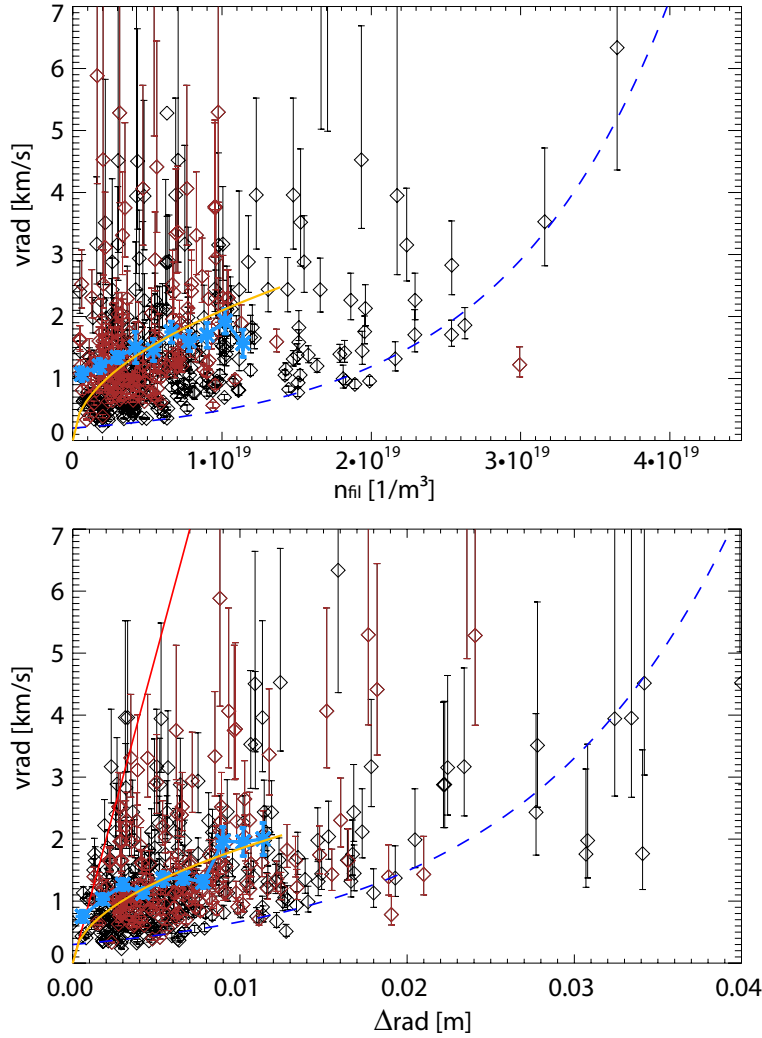


**Figure 5.8:** Dependency of the radial filament velocity on filament density (top) and the radial extent of the filament (bottom). The dashed blue curves show a lower limit for the radial velocity. Large or dense filaments move faster than smaller or thinner ones. Light blue: Mean radial velocity obtained with a boxcar averaging technique. Orange: Fits from eq. (3.38) to the mean radial velocities.

filaments with high density or large radial extent have a higher radial velocity. Due

to the scatter, these lines can only be indications for lower limits. These limits can be expressed by exponential functions of size and density:

$$v_{rad} \geq 300 \text{ m/s} \cdot e^{\Delta_{rad}/0.0125 \text{ m}} \quad (5.8)$$

$$v_{rad} \geq 200 \text{ m/s} \cdot e^{n_{fil}/n_{fil,0}} \quad (5.9)$$

with  $n_{fil,0}$  as defined in eq. (5.5). The exponential behaviour is substantiated by a double logarithmic plot of the data, see fig. 5.9. Even though some filaments are

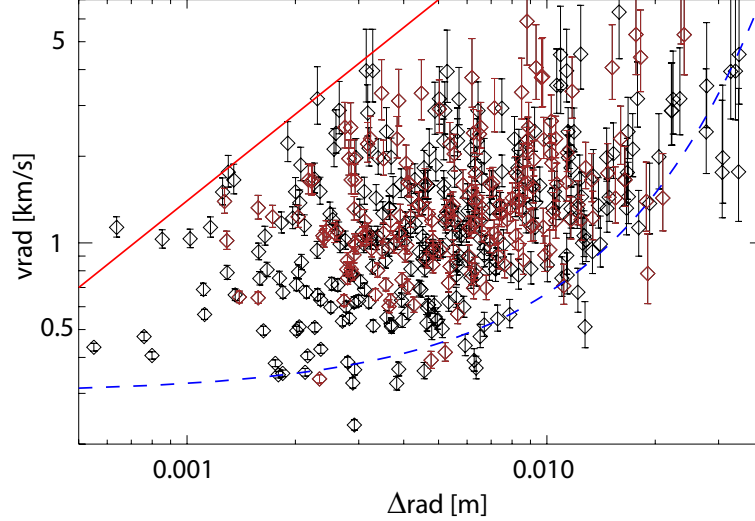


**Figure 5.9:** Double logarithmic plot of fig. 5.8 (bottom) to show the exponential behaviour between radial velocity and filament size, with the dashed blue line showing a lower limit on  $v_{rad}$ .

remarkably faster than the indicated lower limits (up to the velocity resolution limit of 7 km/s), it is clear from fig. 5.8 that dense filaments do not occur at small velocities, and that large filaments do not occur at small velocities.

The solid red line in the lower plot of fig. 5.8 and in fig. 5.9 shows again the detection limit for small filaments based on eq. (5.1), which in this figure translates into

$$v_{rad} \leq \Delta_{rad}/\Delta_{min}[\text{s}]. \quad (5.10)$$

The light blue lines in figure 5.8 show average values for the radial propagation velocity  $v_{rad}$ . The values are obtained by a simple boxcar-technique and have to be compared with eqns. (3.25) and (3.38). The first predicts a rise with density and a decrease with poloidal size, whereas the latter predicts a rise with the square root of density and poloidal size. Slope and offset of the two lines are roughly in agreement with the latter, i.e. with eq. (3.38). To compare with this model, square root functions have been fitted to the averaged radial velocities, giving  $v_{rad} [\text{km/s}] = (n_{fil}/2.28 \cdot 10^{18} \text{ m}^{-3})^{1/2}$  and  $v_{rad} [\text{km/s}] = (\Delta_{rad}/2.94 \cdot 10^{-3} \text{ m})^{1/2}$  (orange lines in figure 5.8). The curves disagree significantly from the scaling predicted by equation (3.25).

Further details can be derived from the distribution functions that are shown in fig. 5.10. All three parameters show a clear maximum at  $v_{rad} = 1.1 \text{ km/s}$ ,  $\Delta_{rad} = 2.7 \text{ mm}$  and  $n_{fil} = 2.6 \cdot 10^{18} \text{ m}^{-3}$ , respectively. About 85% of the evaluated filaments have a radial extent of less than 1 cm. The tail of the density distribution function ( $n_{fil} >$

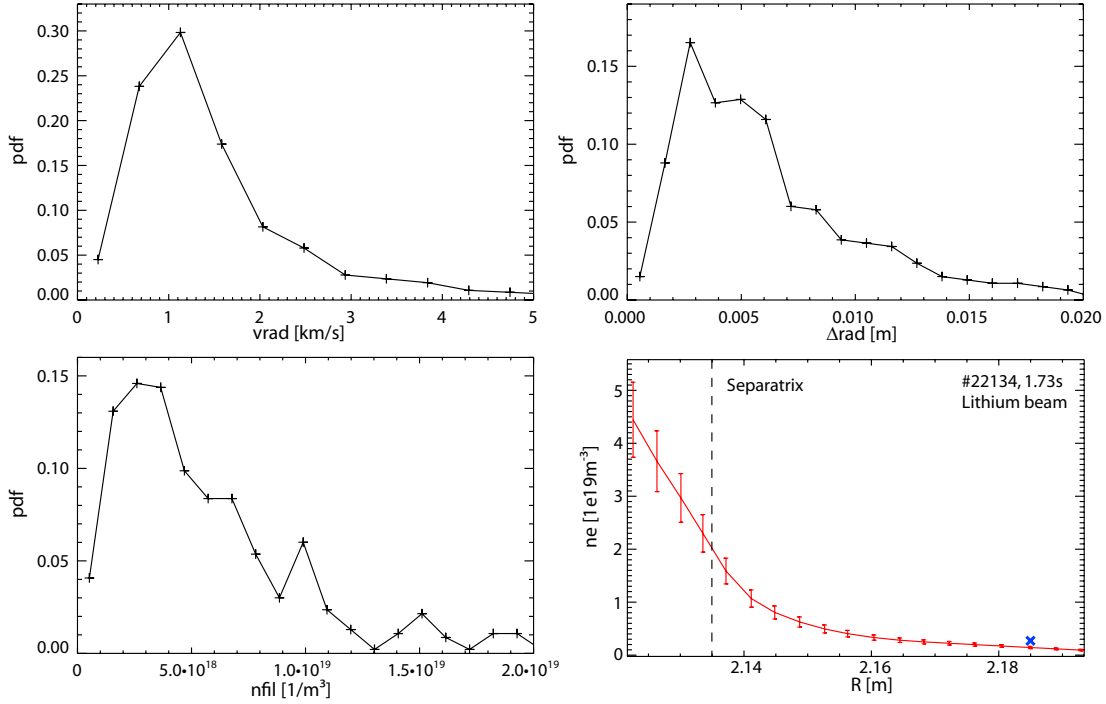


**Figure 5.10:** Distribution functions for radial velocity, radial extent and density from a database of 466 filaments. The maxima are  $v_{rad} = 1.1$  km/s,  $\Delta_{rad} = 2.7$  mm and  $n_{fil} = 2.6 \cdot 10^{18} \text{ m}^{-3}$ . The plot in the lower right shows an inter-ELM plasma density profile from Lithium beam measurements for a comparison with the filament density. The peak of the filament density distribution as measured by the filament probe is indicated by the blue cross.

$1.2 \cdot 10^{19} \text{ m}^{-3}$ ) is slightly underestimated because of the current limitation of the second set of power supplies. From a comparison with an inter-ELM plasma density profile (lower right in fig. 5.10, 10 ms integration time, integration period ends right before the ELM crash), one can see that the filament densities reach values of up to the separatrix density which is about  $2 \cdot 10^{19} \text{ m}^{-3}$ . However, most filaments have a smaller density, consistent with the assumption that filaments are generated close to the separatrix with densities close to the separatrix values, and that they lose particles by parallel transport to the target tiles on their way radially outwards.

### 5.1.5 Evolution of Size and Density

Fig. 5.11 shows the relation between the radial size of a filament and its density. Several trends can be derived from this figure:

- The red line shows again the detection limit (5.1) together with eq. (5.9), giving an absolute detection limit for filaments with small  $\Delta[s]$  and low density,

$$\Delta_{rad}(n_{fil}) \geq 200 \text{ m/s} \cdot \Delta_{min}[s] \cdot e^{n_{fil}/n_{fil,0}}. \quad (5.11)$$

- A lower limit to the radial extent  $\Delta_{rad}$  is given by the linear dashed blue line, which is described by

$$\Delta_{rad}(n_{fil}) \geq 2.5 \cdot 10^{-3} \text{ m} \cdot n_{fil}/n_{fil,0}. \quad (5.12)$$

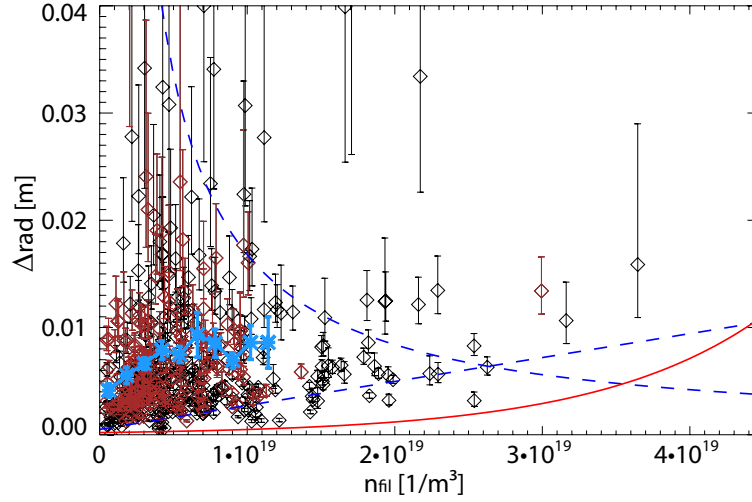


**Figure 5.11:** Radial size of a filament versus filament density. Solid red: Absolute detection limit. Dashed blue: Limit on density gradient and particle content of filaments.

This line can be seen as an upper limit on the radial density gradient inside a filament, e.g.

$$\frac{n_{fil}}{\Delta_{rad}/2} = 8.96 \cdot 10^{21} \text{ m}^{-4} \quad (5.13)$$

under the assumption of a symmetric density gradient at both sides of the filament.

- An upper limit to the radial extent can be given by the decreasing dashed blue line, which is described by:

$$\Delta_{rad}(n) \leq \frac{0.015 \text{ m}}{n_{fil}/n_{fil,0}}. \quad (5.14)$$

Because of the density dependence, this can be converted into an upper limit on the line integrated density,

$$n_{fil} \cdot \Delta_{rad}(n) \leq 1.68 \cdot 10^{17} \text{ m}^{-2}, \quad (5.15)$$

which is a measure for the particle content of a filament.

- The light blue line has been obtained by a boxcar averaging technique and gives mean values for the radial extent for different filament densities and suggests  $\Delta_{rad} \propto n_{fil}$  for small filament densities.

Fig. 5.12 shows the development of filament core density and size with the travelled distance. The filament density (upper plot) decreases with propagated distance and can be described by an upper limit

$$n_{fil}(dR) \leq 3.5 \cdot 10^{19} \text{ m}^{-3} \cdot (1 - dR/0.115 \text{ m}). \quad (5.16)$$

This indicates, that filaments are generated close to the separatrix with a density of about  $3.5 \cdot 10^{19} \text{ m}^{-3}$ , which is in the order of the pedestal density. Equation (5.16) has

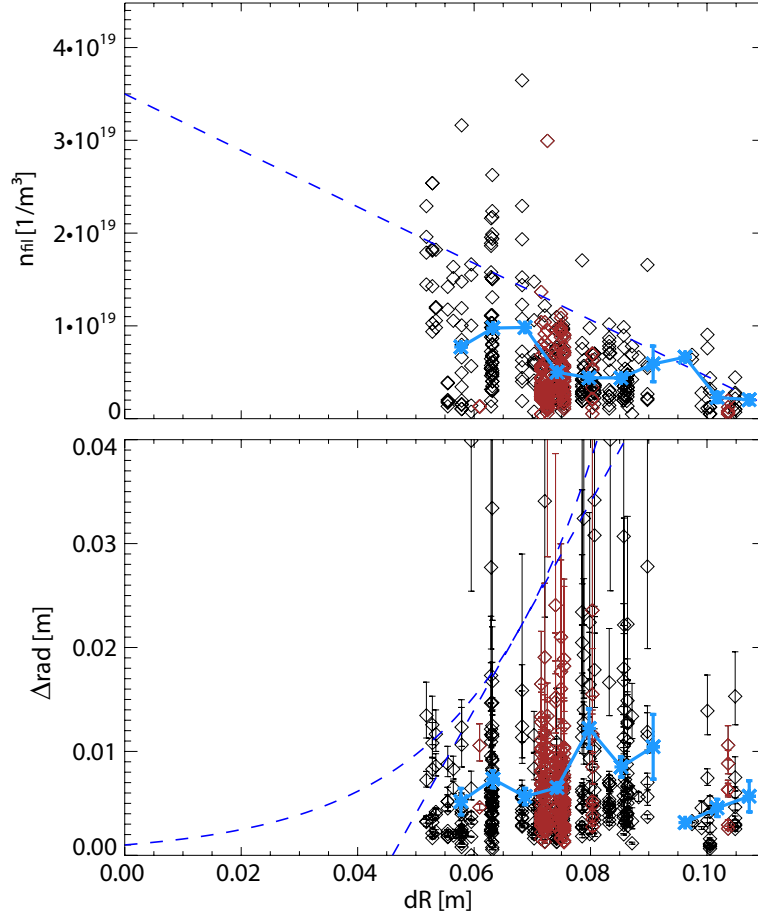


**Figure 5.12:** Evolution of filament core density (upper) and radial extent (lower) with distance from the separatrix. Light blue: Boxcar averaged values.

been based on the significant decay in the number of data points at higher densities. Choosing an absolute limit or envelope would yield higher densities, e.g. in the order of the pedestal top values. The extrapolation could be improved by additional data from very small or very large  $dR$ . However, the data from  $dR < 5$  cm shows already lots of structures on the ion saturation current, so that it would become more and more difficult to detect and/or distinguish filaments. On the other hand, very large distances such as  $dR > 10.5$  cm will give very few filaments in a machine like ASDEX Upgrade, i.e. 1-2 per ELM. These would of course be the remainders of the strongest filaments. Therefore, adding new data will be difficult. Nevertheless, from the data already available, it seems very reasonable to assume that filaments are generated close to the separatrix with initial densities close to the separatrix values.

The lower graph in fig. 5.12 shows the evolution of the filament size with the distance from the separatrix. Two curves are shown: A linear approximation  $\Delta_{rad}(dR) \leq dR - 0.046$  m that matches the data for  $dR = 4 - 9$  cm. A linear fit is, however, not very reasonable if we assume that the filament is generated somewhere around the separatrix, as it would not allow filaments within 4 cm from the separatrix. An exponential function

is a more reasonable approximation, e.g.

$$\Delta_{rad}(dR) \leq 0.001 \text{ m} \cdot e^{dR/0.022 \text{ m}} \quad (5.17)$$

can be used as an upper limit to the data in the given  $dR$ -range. From both approximations, it becomes clear that the filaments broaden with travelled distance, i.e. with time, probably due to diffusion.

The question is whether the density decay is only due to broadening or also due to particle loss by parallel transport: In the latter case, the filament would move radially outwards and, in the meanwhile, lose density to the target plates by parallel transport. From (5.16), the filaments seem to be depleted after a distance not larger than 12 cm, which would correspond to a time of flight of about  $120 \mu\text{s}$ , assuming a mean radial velocity of 1 km/s.

Fig. 5.13 shows the evolution of the particle content  $n_{fil}\Delta_{rad}$  of a filament. The solid

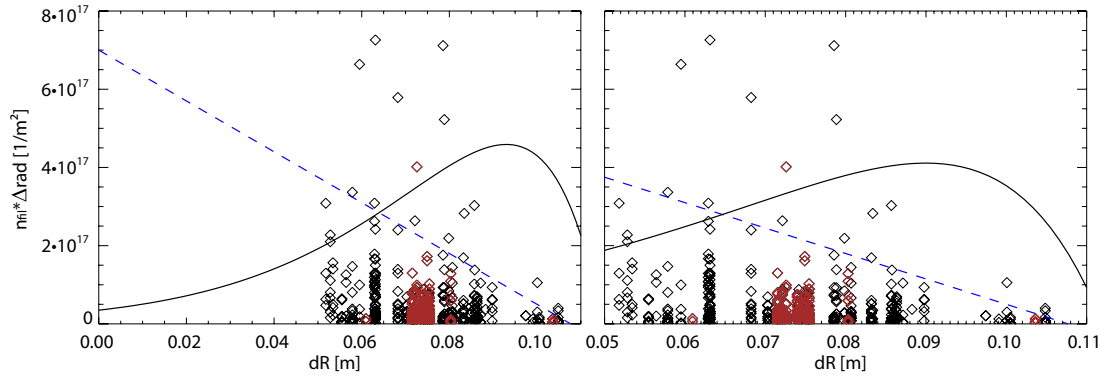


**Figure 5.13:** Evolution of the particle content of a filament with the distance from the separatrix (enlarged version on the right). The decay clearly indicates that particles are lost by parallel losses, and not by broadening of the filament.

black curve is an estimate of the upper limit of the particle content from eqns (5.16) and (5.17), whereas the dashed blue line represents an upper limit on the data with the linear parametrisation

$$n_{fil}\Delta_{rad} \leq 7 \cdot 10^{17} \text{ m}^{-2} - 6.5 \cdot 10^{18} \text{ m}^{-3} \cdot dR \quad (5.18)$$

The slope of that line is negative, which means that the particle content of a filament decreases from its initial value of about  $7 \cdot 10^{17} \text{ m}^{-2}$  with time, i.e. with the distance from the separatrix, which can be explained by parallel losses. With the most likely radial velocity of  $v_{rad} \approx 1 \text{ km/s}$  (fig. 5.10), the resulting loss rate is  $6.5 \cdot 10^{22} / \text{m}^2\text{s}$ . This is in quite good agreement with a simple estimate for free particle flow along the field lines,  $\Gamma = n_{fil}c_s = 1.3 \cdot 10^{23} / \text{m}^2\text{s}$ , using the most probable filament density and the sound speed for the temperatures cited above.

### 5.1.6 Radial Acceleration

This leaves us with the question whether the radial velocity changes with the distance from the separatrix, i.e. whether the filaments are accelerated or not. Even though one would not expect any acceleration more than 2 cm away from the separatrix according



to [77, 62], a radial acceleration of  $1.2 \cdot 10^8 \text{ m/s}^2$  has been reported from MAST [42]. The data from ASDEX Upgrade is shown in fig. 5.14 as a scatter plot on the left, and as  $v_{rad}$  distribution functions on the right. The scatter plot has an envelope that goes

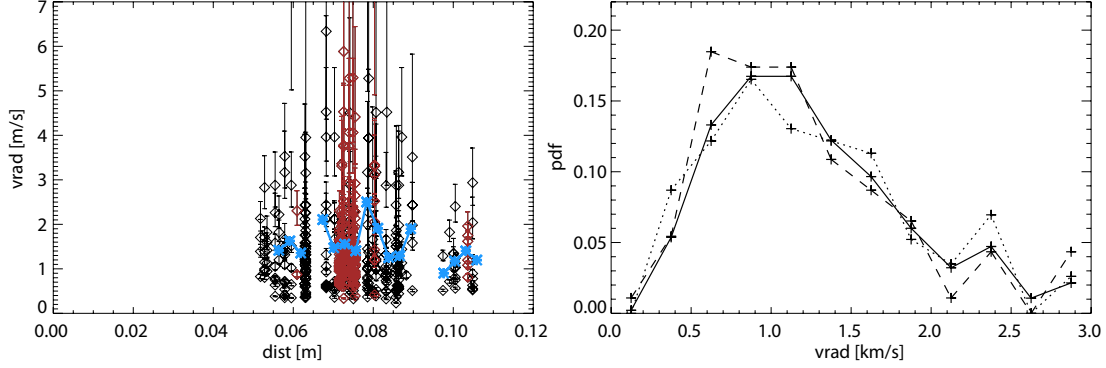


**Figure 5.14:**  $v_{rad}$  dependency on the distance to the separatrix (left). The light blue points indicate the mean values for every 0.5 cm. The distribution function on the right show the  $v_{rad}$  distribution for all filaments (solid line), for  $dR < 7 \text{ cm}$  (dotted) and  $dR > 8.1 \text{ cm}$  (dashed line).

to higher radial velocities for medium distances due to the higher number of data points there. Mean values have been overlaid in blue for every 0.5 cm. These points do not show a significant dependence on the distance  $dR$  to the separatrix. This is confirmed by the probability distribution functions that have been calculated for velocities up to 3 km/s for all filaments (solid line), for filaments with  $dR < 7 \text{ cm}$  (dotted) and with  $dR > 8.1 \text{ cm}$  (dashed). The curves do not show significant deviations, so that acceleration does not seem to be a dominant factor for the ASDEX Upgrade data shown here.

A constant acceleration  $a = 10^8 \text{ m/s}^2$  [87] would give a velocity  $v_{rad} = (2a \cdot dR)^{0.5}$  in the order of 4 km/s after 7 cm, which is within the detection limits of the method used here.

### 5.1.7 Summary on the Radial Propagation Velocity

The radial velocity of impinging filaments has been calculated from time delay measurements together with the amplitude and width of the corresponding ion saturation current signal. 466 filaments have been analysed. The data has been converted into density and size of the filaments, and several trends have been derived. Most important, it has been shown that filaments with large radial extent move faster than smaller ones, and that filaments with higher density move faster than filaments with less density,

$$v_{rad} \propto \Delta_{rad}^{1/2} \cdot n_{fil}^{1/2}, \quad (5.19)$$

according to eq. (3.38).

Distribution functions have been calculated, showing that most typical filaments have  $v_{rad} = 1.1 \text{ km/s}$ ,  $\Delta_{rad} = 2.7 \text{ mm}$  and  $n_{fil} = 2.6 \cdot 10^{18} \text{ m}^{-3}$  at the filament probe, compared to separatrix densities of  $2 \cdot 10^{19} \text{ m}^{-3}$ . From a comparison of filament size and density, we could show that the filaments lose density by parallel losses and broaden radially with time. In ASDEX Upgrade, the filaments would be depleted after a distance of about 12 cm from the separatrix. Accordingly, their number is strongly decreased at

large distances from the separatrix. Particle content and density gradient of filaments are limited, giving an upper limit on the energy content of a filament.

The radial velocity of filaments does not seem to vary with time or distance from the separatrix, i.e. no acceleration could be identified from the data. Derived trends were upper or lower limits to the data, as there is a large scatter, most probably due to hidden parameters that are not accessible by our measurements. One possible candidate is the poloidal extent  $\Delta_{pol}$  of the filaments, which is a crucial parameter in the models cited above. The measured radial extent might be directly related to the poloidal extent of the filament, so that the  $\Delta_{rad}$ -dependencies given here might be translated into  $\Delta_{pol}$ -dependencies. In case of a direct conversion, the  $\Delta_{pol}$ -dependencies would already be included in the data shown here. Only deviations from a direct correlation are hidden. Given a direct correlation, or at least a positive scaling between  $\Delta_{rad}$  and  $\Delta_{pol}$ , the data shown here would favour models that predict large filaments to move faster, e.g [77, 62].

## 5.2 Filament Rotation

### 5.2.1 Pin Mapping

Filaments are aligned to the local magnetic field  $\mathbf{B}$  and thus have the same inclination angle as the magnetic field. In this thesis, rotation refers to a poloidal/toroidal motion of the filament as described in sec. 2.2, i.e. a motion in a direction  $\mathbf{p}$  with  $\mathbf{p} \perp \mathbf{B}$  and  $\mathbf{p} \perp \mathbf{R}$ . The direction of the rotation (up/down or co/counter-current) can be derived from a time series analysis, or, to be exact, from the order in which the filament hits the Langmuir pins. The pin order varies with the inclination angle  $\alpha$  and can be calculated by mapping the position  $\mathbf{x}_i$  of the pins  $i = 1...6$  to  $\mathbf{p}$ :

$$\mathbf{x}_i' = (\mathbf{p} \cdot \mathbf{x}_i)\mathbf{p} \quad (5.20)$$

with  $\mathbf{p} \cdot \mathbf{x}_i$  being the directed distance from the first pin  $\mathbf{x}_0 = (0,0)$ . Fig. 5.1 shows the mapped positions  $\mathbf{x}_i$  for  $\alpha = 10^\circ$ . The resulting pin order is

direction	order, 2006	order, 2007
pol. down	2-4-1-3	1-2-3-4-5
pol. up	3-1-4-2	5-4-3-2-1

for pins 1-5. Pins 1 and 6-9 are located very close to each other in terms of their height above the midplane, so that their mapped order depends strongly on the local inclination angle. For  $\alpha = 10^\circ$  and a rotation poloidally downwards, we get the order 6-7-8-1-9-2-3-4-5. An enlarged image of such a mapping is shown in fig. 5.2 for  $\alpha = 8.6^\circ$ . Pins 6-9 have different radial positions and have been used for measuring the radial propagation velocity  $v_{rad}$  in section 5.1.

The rotation velocity can again be derived by time delay measurements with a procedure similar to the procedure used in sec. 5.1.

First of all, we calculate the perpendicular velocity  $v_{\mathbf{p}}$  from the time delay that can be measured when a filament hits a first pin  $i$  and a second pin  $j$  with a relative time difference  $dt_{i,j}$ :

$$v_{\mathbf{p}} = \frac{(\mathbf{p} \cdot \mathbf{x}_i) - (\mathbf{p} \cdot \mathbf{x}_j)}{dt_{i,j}} \quad (5.21)$$

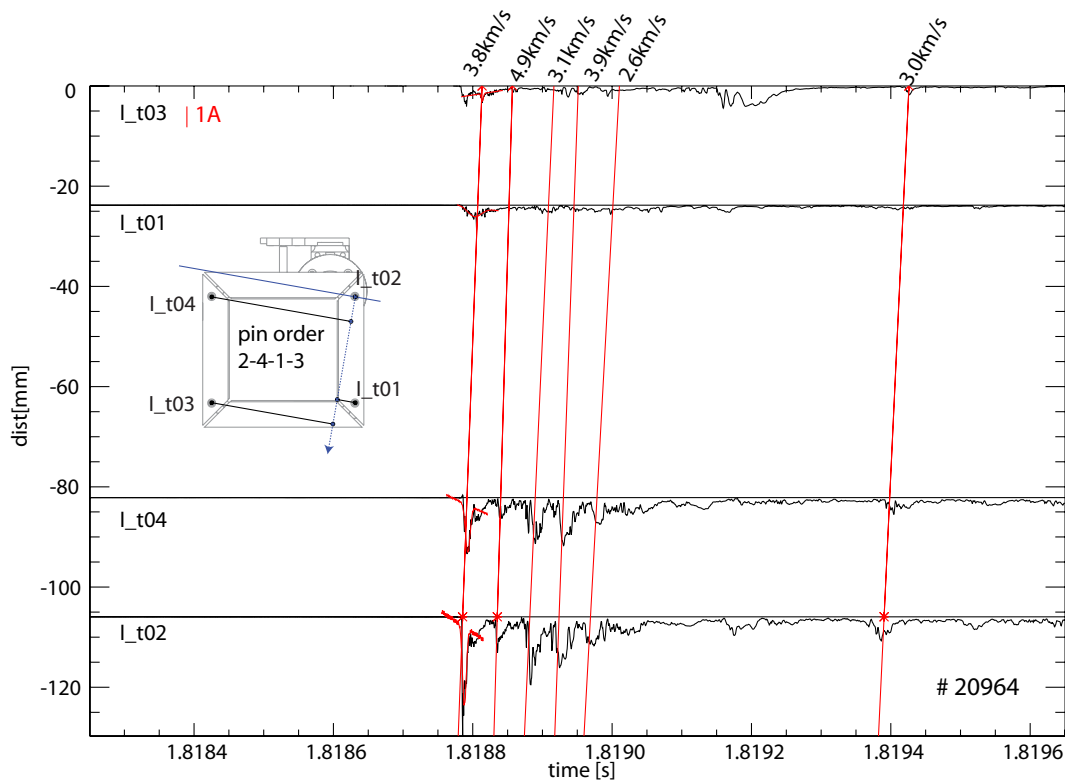
Poloidal and toroidal rotation velocities can then be calculated by mapping  $v_{\mathbf{p}}$  toroidally or poloidally:

$$v_{pol} = v_{\mathbf{p}} / \cos \alpha \quad (5.22)$$

$$v_{tor} = v_{\mathbf{p}} / \sin \alpha = v_{pol} / \tan \alpha \quad (5.23)$$

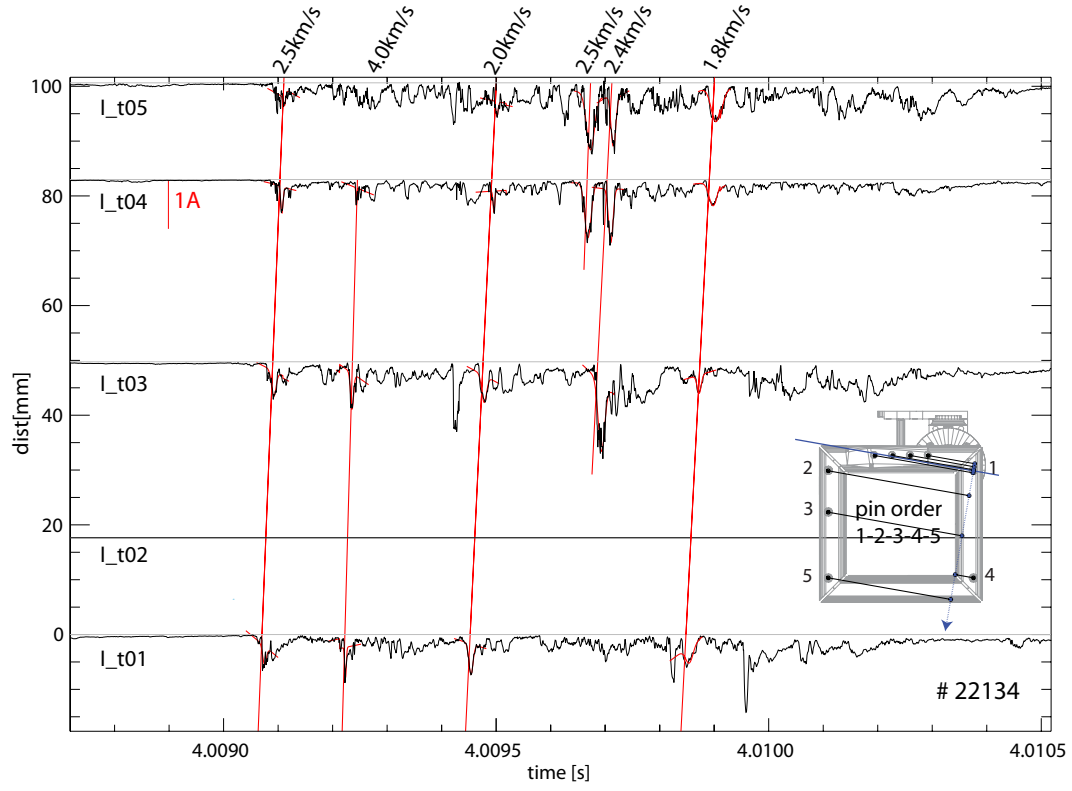
In section 5.1, fig. 5.4, the Langmuir timetraces have been plotted according to their radial separation. Here, the pins have been mapped according to eq. (5.21) and the signal baseline has been shifted by the distance  $\mathbf{p} \cdot \mathbf{x}_i$ . Tracing a filament that is rotating with constant velocity results in a straight line in this plot, whereas a variation of the rotation velocity on the scale of the pin distance would lead to deviations from a straight line. The velocities are then calculated according to eqns. (5.21)-(5.23).

Fig. 5.15 shows an example for the 2006 probe head. The symmetric pin distribution,



**Figure 5.15:** Geometric mapping of the time traces from the 2006 filament probe. Poloidal rotation velocities are given in the upper part.

which was chosen to allow measurements at different magnetic field helicities, translates into 2 pairs of signals with a large gap in between. This gap often led to the problem that filaments have been lost between pin 1 and pin 4 and could therefore not be traced properly over all 4 pins. The 2007 version has therefore been equipped with an additional pin in the middle of the gap, and the numbering has been revised as shown in fig. 5.1. The resulting mapped signals are shown in fig. 5.16. Pin 2 has not been operational for these discharges, but the tracing still has improved a lot. From the 2007 version, it becomes clear that only a fraction of the filaments touches all 5 pins. Some filaments can be traced over 4, 3 or only 2 pins. There might even be cases, where filaments will



**Figure 5.16:** Geometric mapping of the time traces from the 2007 filament probe. Poloidal rotation velocities are given in the upper part.

only hit one pin. This can be explained by the radial propagation velocity of filaments: The filament probe has an inclination angle of about  $16.75^\circ$  to the vertical axis as shown in fig. 5.17. Filaments with a velocity ratio

$$v_{rad}/v_{pol} = \tan \vartheta_{probe} \approx 0.3 \quad (5.24)$$

will therefore hit all 5 pins (if they hit the probe at all). For a velocity ratio up to  $v_{rad}/v_{pol} \approx 0.4$ , the filaments can also hit all 5 pins, but this depends on the starting point: It would be impossible to touch all 5 pins, if the first hit would be at the lowest pin. Filaments with a different velocity-ratio will hit fewer pins, again depending on size and velocity ratio of the filament.

### 5.2.2 Data Evaluation

The poloidal rotation velocities derived from the file delay measurements are given in the upper part of figs. 5.15 and 5.16. They range roughly between 2 and 4 km/s, but do not give a trend within the ELM, e.g. a slowing down of the filaments during the ELM. With the ideal velocity ratio eq. (5.24), this range corresponds to radial velocities of 0.7 – 1.3 km/s, which is exactly the maximum of the  $v_{rad}$ -distribution.

Similar to the evaluation of the radial propagation velocity, a statistical analysis has been carried out for the filament rotation velocities: A series of 128 filaments from discharge #22134 has been analysed. For each filament, the following parameters have been stored in the database:

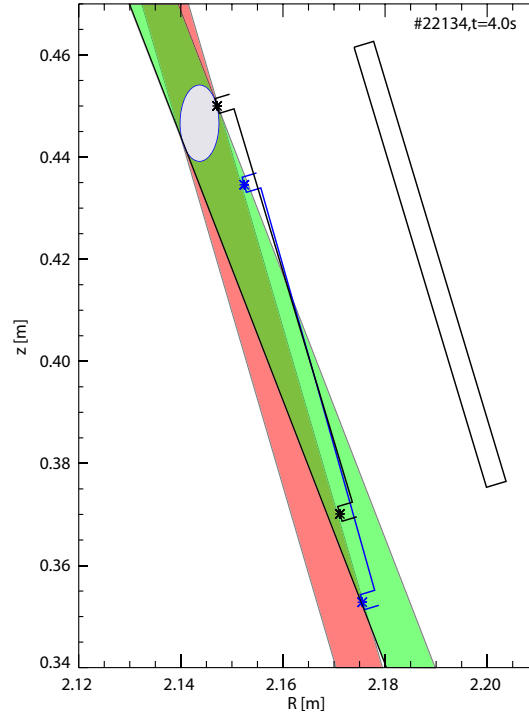


**Figure 5.17:** Velocity range in which filaments can hit all 5 pins of the filament probe. The black line shows the pins of the right side of the filament probe ( $\phi_r = 183, 8^\circ$ ), and the blue line shows the pins from the left side of the filament probe ( $\phi_l = 183, 8^\circ$ ) mapped along the magnetic field to  $\phi_r$ . The velocity limits are  $v_{rad}/v_{pol} \approx 0.3$  (red) and  $v_{rad}/v_{pol} \approx 0.4$  (green). Exact values depend on the shape of the filament, as the range widens for larger filaments.

- distance  $dR$  between filament probe and separatrix
- poloidal rotation velocity  $v_{pol}$  and toroidal rotation velocity  $v_{tor}$  from the time delay measurements, the conversion being given by eq. (2.8).
- peak ion saturation current
- (temporal) width  $\Delta[s]$  of the ion saturation peak

Errors have not been estimated here, because the error of erroneously connecting non-correlated events is not negligible due to the still large distance between the pins. For the  $v_{rad}$  measurements, this error was non-existent as the small radial distance between the pins gave much better correlated signals, i.e. the signals could be traced much easier.

The ion saturation current has been translated into a filament core density  $n_{fil}$  according to eq. (5.4), and the temporal peak width  $\Delta[s]$  has been converted to a spatial extent  $\Delta_{pol}$  by multiplication with the poloidal rotation velocity,

$$\Delta_{pol} = v_{pol} \cdot \Delta[s]. \quad (5.25)$$

The resulting scatter plot for the poloidal rotation velocity versus filament size is shown in fig. 5.18. The blue line describes a linear rise of  $v_{pol}$  with the poloidal size of the

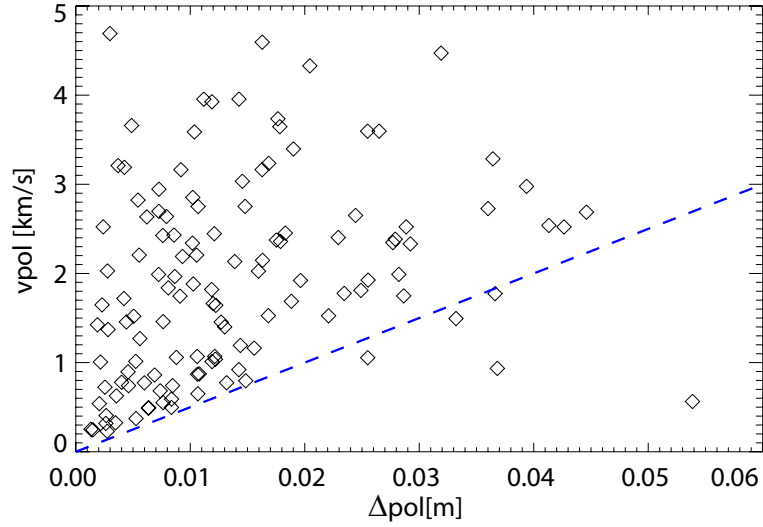


**Figure 5.18:** Poloidal rotation velocity versus poloidal size of the filament, showing that  $v_{pol}$  increases with filament size.

filament,

$$v_{pol} = \Delta_{pol}/2 \cdot 10^{-5} \text{ s} \quad (5.26)$$

Again, the line denotes only a lower limit to the data and there are lots of filaments with considerably higher poloidal velocities of up to 5 km/s. The poloidal size of the filaments is in the cm range with an extent of up to 6 cm for the largest filaments.

Fig. 5.19 shows the dependency of the poloidal rotation velocity on the distance from

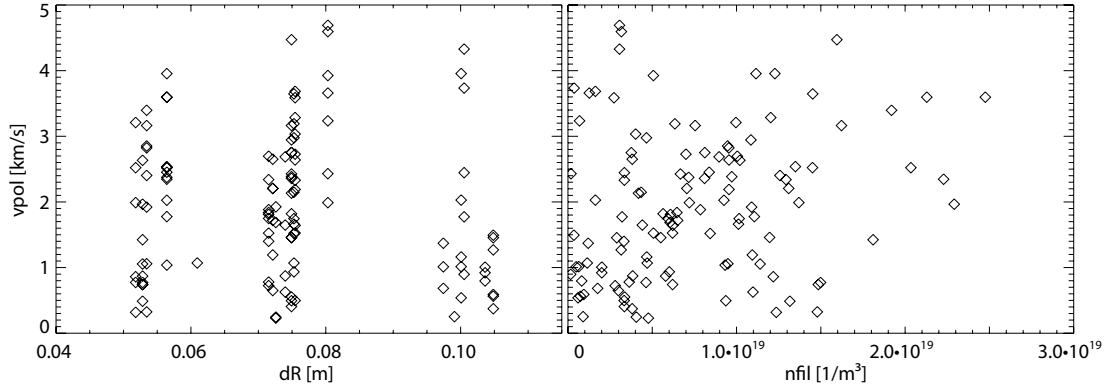


**Figure 5.19:**  $v_{pol}$  versus distance from the separatrix and filament density. The scatter plots show no clear trend, so that both parameters do not seem to affect the poloidal motion of the filament.

the separatrix and the density. For both parameters, there is no clear trend observable and  $v_{pol}$  does not seem to be affected.

Probability distribution functions are shown in fig. 5.20 for the poloidal rotation velocity  $v_{pol}$  and the poloidal size  $\Delta_{rad}$ . The velocity distribution shows a flat top between 0.5 km/s and 2.6 km/s. Velocities up to 5 km/s can be seen at non-negligible rates.

The filament size has a maximum at about 1 cm and significant contributions until

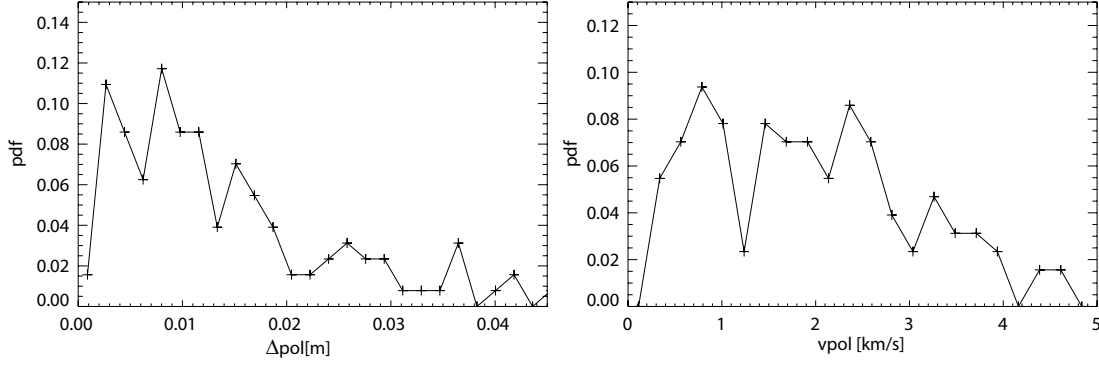


**Figure 5.20:** Probability distribution function for  $v_{pol}$  and  $\Delta_{pol}$ . The poloidal filament size (FWHM) has a maximum at  $\Delta_{pol} = 1$  cm, whereas the  $v_{pol}$ -distribution shows a flat top from 0.5 km/s to 2.6 km/s.

2 cm. This poloidal size given here is again the full width at half maximum, i.e. visible imaging will give somewhat higher numbers as it pronounces the filament's edges. According to eq. (5.23), the poloidal velocity has also been translated into a toroidal velocity. The ratio between  $v_{tor}$  and  $v_{pol}$  is given by the tangens of the local field line inclination angle  $\alpha$  as described in eq. (2.8). For the 128 filaments shown here, the ratio is  $6.37 \pm 0.17$ , so that the velocity range for  $v_{tor}$  goes up to 38 km/s. This is very close to the plasma rotation at the separatrix, which is about 30 km/s according to very recent measurements with a highly resolving charge exchange diagnostic [88]. Unfortunately, the time resolution does not allow for time resolved measurements of the rotation during an ELM, so that these measurements can not be directly correlated to the filament measurements.

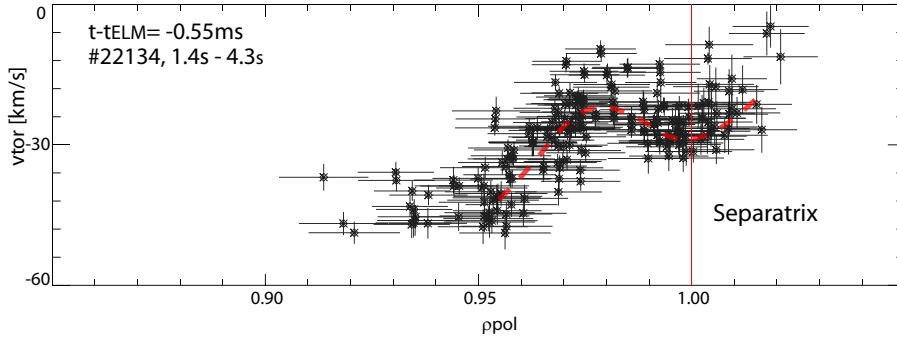


**Figure 5.21:**  $v_{tor}$  profile from the new charge exchange diagnostic [88] over the radial coordinate  $\rho_{pol}$  (normalized poloidal magnetic flux), 550  $\mu$ s before the ELM. Close to the separatrix, the plasma rotates with about 30 km/s in co-current direction, which is in the same range as the maximum toroidal filament rotation values.

### 5.3 On the Interpretation of Velocity Measurements

In the preceeding sections, we have derived values for poloidal, toroidal and radial propagation velocities. The following table summarises the most probable values:

$v_{rad} = 1.1 \text{ km/s}$	$\Delta_{rad} = 0.27 \text{ cm}$
$v_{pol} = 0.5 - 2.6 \text{ km/s}$	$\Delta_{pol} = 0.8 \text{ cm}$
$v_{tor} = 3 - 16 \text{ km/s}$	$\Delta_{tor} = 5.1 \text{ cm}$
$n_{fil} = 2.6 \cdot 10^{18} \text{ m}^{-3}$	$T_i = 30 - 60 \text{ eV}$

The question is how these values can be combined. The answer is quite simple for the velocities, where

$$\mathbf{v}_{fil} = v_{rad} \cdot \mathbf{e}_R - v_{pol} \hat{\mathbf{z}} \quad (5.27)$$

holds: The two velocity measurements are completely independent because of the given geometry.

The derived filament sizes are not independent, as they are based on the temporal length of the cut through the filament. The slope of the cut is given by the velocity ratio, and the filament sizes derived from these values are basically projections on the horizontal and vertical axis, respectively. Fig. 5.22 shows the underlying principle: The

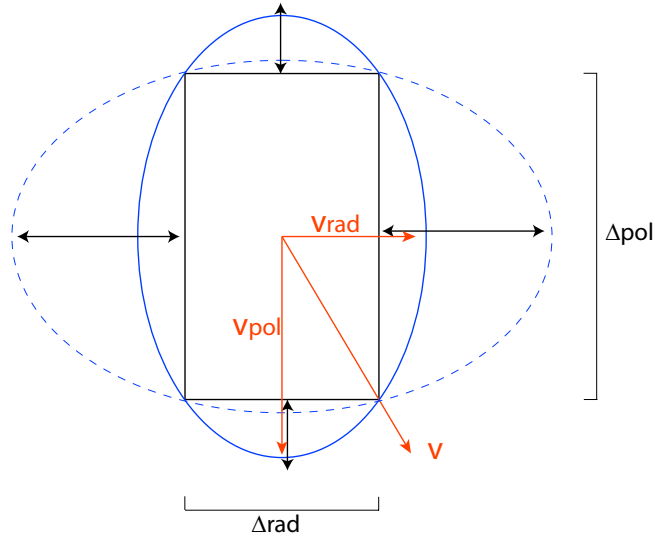


**Figure 5.22:** Possible filament shapes from the Langmuir measurements, which define the inscribed rectangle. The filament shape is known to have a poloidal axis larger than the radial one from both theory and visible imaging, so that shapes like the dashed one can be discarded.

red line shows the motion of the center of a filament moving with velocity  $\mathbf{v}$  as given by eq. (5.27). Radial extent  $\Delta_{rad}$  and poloidal extent  $\Delta_{pol}$  of the filament are projections of the spatial extent of the cut to the vertical or horizontal axis, respectively. These projections span a rectangle with width  $\Delta_{rad}$  and height  $\Delta_{pol}$ . The contour of the filament at half maximum must go through the corners of this rectangle, because the peak width values have been derived from the full width at half maximum of the ion saturation peak.

For a more detailed analysis, we assume that filaments have an elliptic cross-section. This ellipse is determined from our measurements by the fact that it has to touch the corners of the rectangle, which are given by the filament sizes. Ellipses are generally described by

$$r(\phi) = \sqrt{a^2 \cos^2 \phi + b^2 \sin^2 \phi} \quad (5.28)$$



with  $\phi = [0, 2\pi]$ , and the two axes  $a$ ,  $b$  are therefore constrained by the rectangle to fulfill

$$r(\phi) = \frac{1}{2} \sqrt{\Delta_{rad}^2 + \Delta_{pol}^2} \text{ for } \phi = \arctan\left(\frac{v_{pol}}{v_{rad}}\right), \quad (5.29)$$

which leaves the eccentricity of the ellipse undetermined. The constraint (5.29) can therefore be fulfilled by a bunch of ellipses with different axes  $a$  and  $b$ . As indicated in fig. 5.22 by the dashed line, even filaments with a radial axis larger than the poloidal one would fulfill the requirement (5.29). However, it is well known from theory and visible imaging that filaments take a shape with a poloidal axis bigger than the radial one. The inscribed rectangle delivered by our Langmuir measurements is in good agreement with both.

With the method used here, it is furthermore not possible to fully determine the filament properties for one single filament, as radial and poloidal velocity of one single filament can not be measured simultaneously. We can either measure  $v_{rad}$  and the temporal peak width  $\Delta[s]$ , or  $v_{pol}$  and  $\Delta[s]$ , which gives only one of the two dimensions as

$$\Delta_{rad} = v_{rad} \cdot \Delta[s], \quad (5.30)$$

$$\Delta_{pol} = v_{pol} \cdot \Delta[s]. \quad (5.31)$$

It has to be evaluated, if the filament shape can be derived from a combination of several Langmuir pins that cut through the filament at different positions as indicated in fig. 5.23. However, the positions of these cuts depend strongly on the exact  $v_{rad}/v_{pol}$  ratio: For a velocity ratio  $v_{rad}/v_{pol} = 0.3$ , which corresponds exactly to the poloidal inclination angle of the filament probe, eq. (5.24), the 5 pins cut through the filament at the same position. On the other hand, for the case with the highest radial velocity, where still all 5 pins are hit,  $v_{rad}/v_{pol} = 0.4$ , the positions of the cut stretch over the whole size of the filament. Therefore, a rough assumption on  $v_{rad}/v_{pol}$  is not sufficient to locate the positions of the 5 cuts relative to the filament. It would be necessary to measure both radial and poloidal velocity with an error of less than 5% in order to evaluate the shape of the filament by Langmuir probes.

## 5.4 Propagation in Limiter Shadowed Regions

Up to now, we have only treated unperturbed filaments in front of limiting structures. We can estimate the effect of limiting structures on filaments by comparing measurements of the filament probe at different radial positions to measurements of the mid-plane manipulator at a fixed position. Fig. 5.24 shows the position of the filament probe in #21278 at  $t_1 = 2.17$  s, where it is in front of the leading ICRH-limiter, and at  $t_2 = 4.17$  s, where it is behind this limiter and the adjacent protection limiter. In the discharge shown here, the probe drive has been activated from 1.5 – 3.5 s, so that, according to fig. 4.7, the filament probe should be approximately 4 cm behind the adjacent protection limiter. It is important to note, that the filament probe is located close to a surrounding limiter: The pin in the lower left corner is the one with the the greatest distance to the adjacent protection limiter, with  $d_{pol} \approx d_{tor} \approx 13$  cm. Fig. 5.25 shows the time traces of the ion saturation measurements during an ELM at the 2 times  $t_1$  and  $t_2$ . One can clearly see several characteristic differences between the two sets of time traces, in particular:

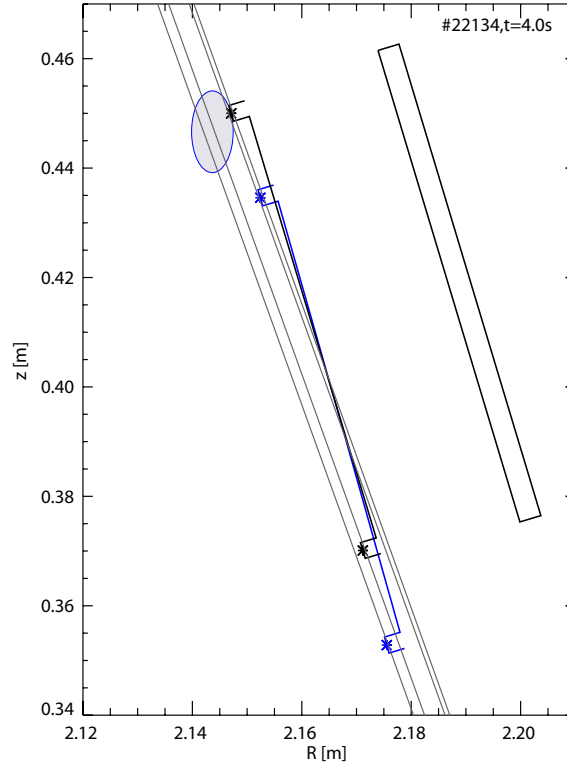


**Figure 5.23:** A filament within the velocity range shown in fig. 5.17 touches all 5 Langmuir pins. The pins cut the filament at different positions that strongly depend on the exact velocity ratio.

- The amplitude ratio between midplane and filament probe has changed from 0.6/2 in case 1 to about 0.6/1 in case 2, where the filament probe has been retracted, i.e., the amplitude and, consequently, the filament density have been reduced by a factor of 2 because of the limiters and parallel transport in the limiter shadow: the smaller connection length to solid surfaces (i.e., the limiting structures) leads to a faster loss of energy and particles and to a reduction of the amplitude of the ion saturation current.
- The filament width has been strongly reduced in case 2. The retracted filament probe shows only sharp peaks, whereas the midplane probe shows peaks with a certain width. The peak width is affected by both filament velocity and filament size. As we do not expect the filaments to accelerate in the limiter shadow, so that the change in peak width indicates a strongly reduced filament size.
- The background component has been reduced in case 2, on the retracted filament probe. The background is caused by a more or less homogeneous flow of particles (or small structures) to the probe during the ELM. The reduction of the background component indicates that big structures are nearly unaffected by the limiter, whereas small structures are completely sheared off.

It is important to note that the limiters do not prevent filamentary structures from penetrating into limiter shadowed regions. This shows that filaments can reach structures

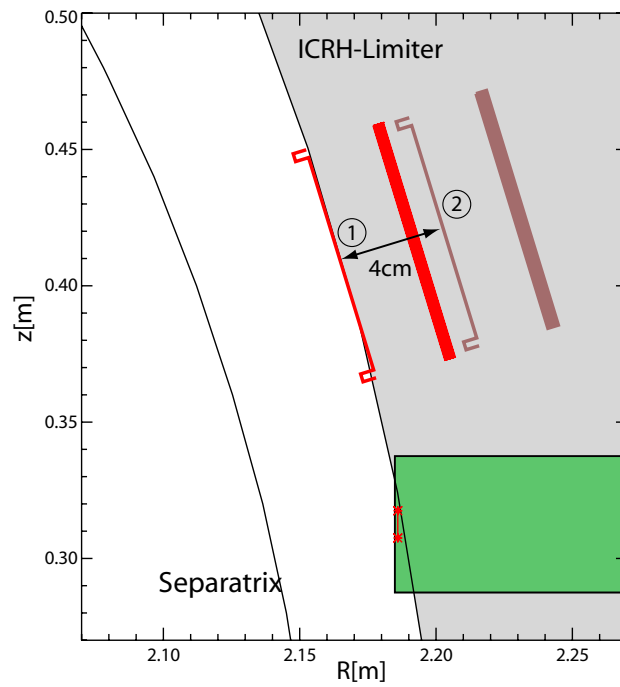


**Figure 5.24:** Position of the filament probe at  $t_1 = 2.17\text{s}$  and  $t_2 = 4.17\text{s}$ . The position of the midplane probe is constant as well as plasma parameters. A comparison of both probes allows for studies of the filament propagation into limiter shadowed regions.

even behind limiters, although they do not deposit much energy there. The limiters do, however, succeed in reducing the power load to these components, although no exact numbers can be given here.

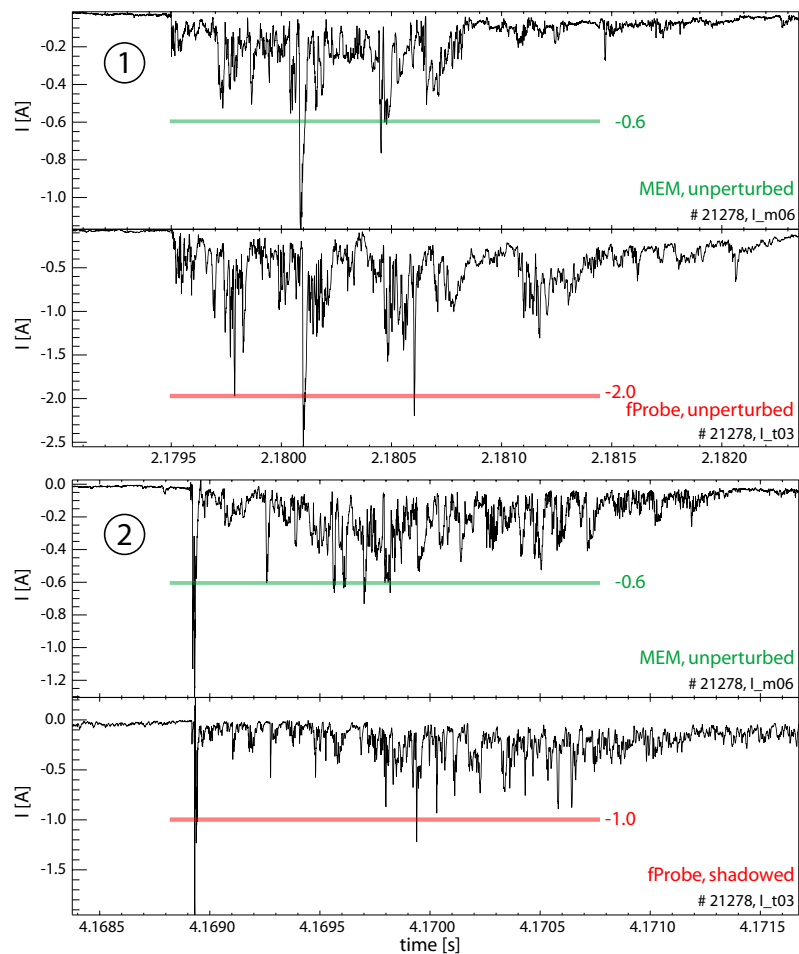


**Figure 5.25:** Time traces from the filament probe at a position in front of the limiter (unperturbed, upper part) and at about 4 cm behind the limiter (lower part) compared to measurements from the midplane manipulator probe at constant position. Note that the pin area is different for both probes.

## Chapter 6

# Magnetic Signature of ELMs

The magnetic signature of ELMs has been studied since many years. Authors have usually focused on magnetic precursors [89, 90, 91, 92]: magnetic oscillations at various frequencies, which appear shortly before an ELM and have been used for ELM classification. Almost no studies have been performed on the magnetic signature during the ELM itself. An example for the magnetic signature of a type-I ELM is given in fig. 6.1. Here, the magnetic signature has been measured with the magnetic coil in the filament probe and the two 3D coilsets on the dual magnetic probe on the midplane manipulator, which measure radial, poloidal, and toroidal component at 2 different radial locations. As both midplane manipulator and filament probe are located along the same field line, they measure along the same filament at different positions relative to the filament. In this chapter, we will try to assess the question if and how filaments contribute to the magnetic signature of an ELM.

### 6.1 Numerical Simulation

#### 6.1.1 Technical Properties

A numerical simulation program has been written to calculate the magnetic signature of a filament for the ASDEX Upgrade geometry. The program correctly includes the position of the filament probe and the (time resolved) position of the midplane manipulator probe. Fig. 6.2 shows the poloidal cross section of the ASDEX Upgrade geometry. The calculation is not full 3D, but calculates the magnetic field in two poloidal planes, namely the plane of the filament probe ( $\phi = 185.06^\circ$ ) and the plane of the midplane manipulator ( $\phi = 168.75^\circ$ ). In fig. 6.2, filaments in the plane of the filament probe are indicated by lighter colours.

The filament is assumed to have an elliptic shape as indicated by visible imaging (e.g. fig. 2.7). We constrain our parameter space to the order of the values derived in section 5 in a sense that the input parameters do not differ by a factor of more than 2 or 3 from the most probable values.

Arbitrary current distributions can be defined over a calculation grid with a resolution of typically 1 mm. The grid represents the rest frame of the filament and is shifted poloidally and radially according to the motion of the filament. Filament motion, velocity, or acceleration can also be defined arbitrarily.

The magnetic field is evaluated over a rectangular grid that contains the probe positions and has a resolution of typically 1 mm. For each point of the filament grid, the magnetic

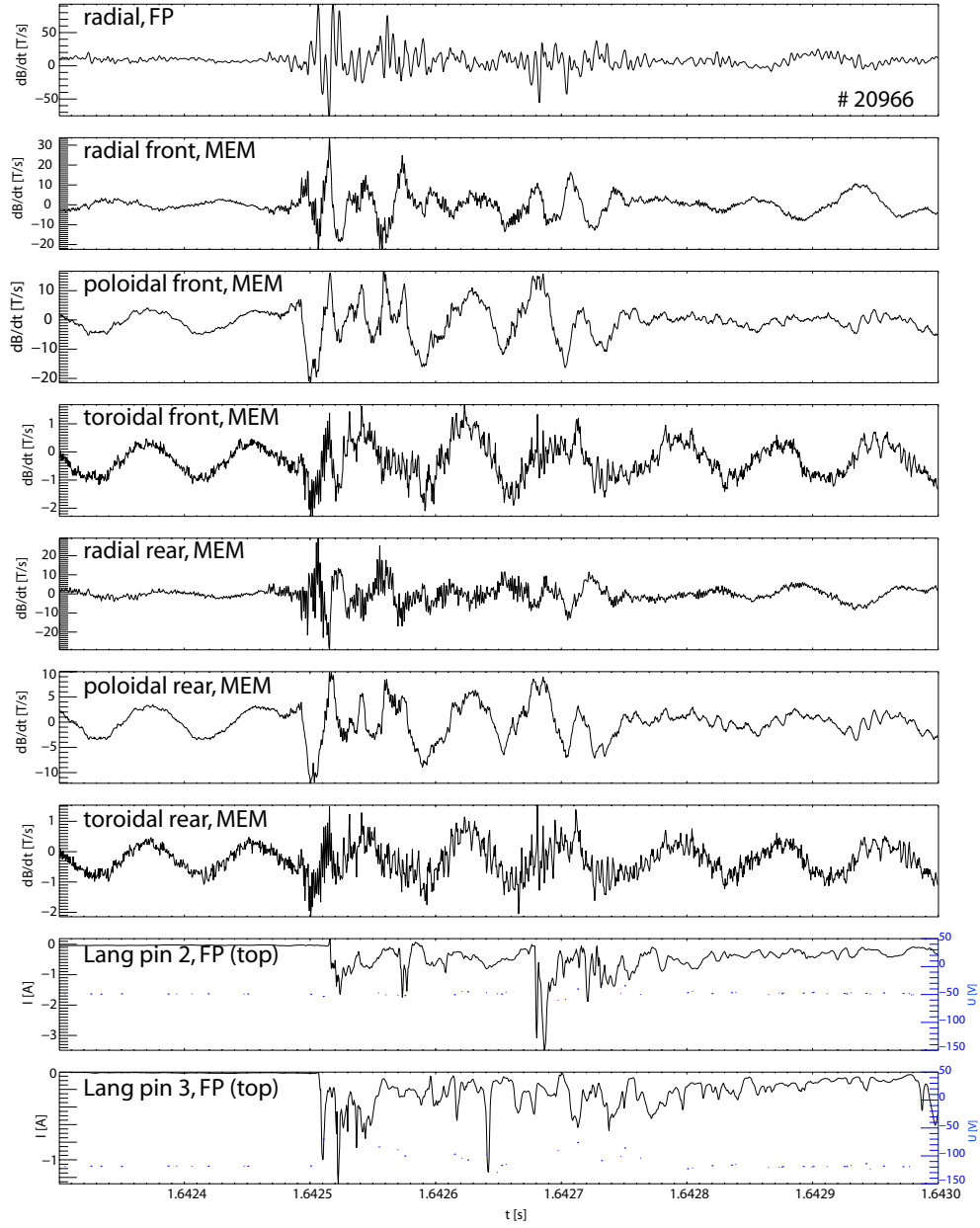


**Figure 6.1:** Magnetic signature  $dB/dt$  of a type-I ELM as measured with 7 magnetic coils along the same field line and, i.e., along the same filaments. The coils used here are the magnetic coil in the filament probe and the two 3D coilsets in the dual magnetic midplane probe.

field for every point of the probe grid is calculated using Biot-Savart's law. The total magnetic field is then calculated by superposition. The 3 components are

$$B_{rad} = \frac{\mu_0}{2\pi} \left\langle \int_{fil} \frac{I}{d} \cos \theta \, dA \right\rangle_{probe} \quad (6.1)$$

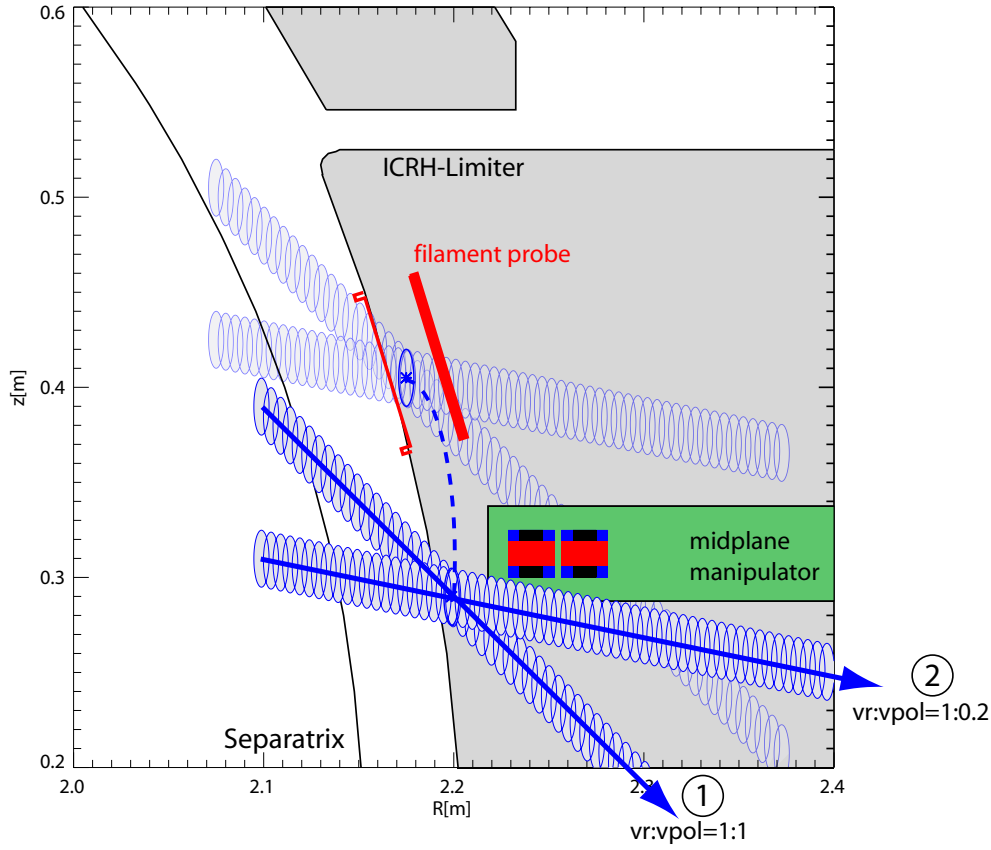


**Figure 6.2:** Illustration of the calculation grid for the numerical simulation of the magnetic signature of filaments. Positions of the probes and the filament with radial and poloidal propagation velocity are correctly taken into account. Arbitrary current distributions can be used, e.g. to represent uni-directional and bi-directional currents.

$$B_{pol} = \frac{\mu_0}{2\pi} \left\langle \cos \alpha \int_{fil} \frac{I}{d} \sin \theta dA \right\rangle_{probe} \quad (6.2)$$

$$B_{tor} = \frac{\mu_0}{2\pi} \left\langle \sin \alpha \int_{fil} \frac{I}{d} \sin \theta dA \right\rangle_{probe}, \quad (6.3)$$

with integration over the filament grid and averaging over the probe grid.  $d$  is the distance between the point of the probe grid and the point of the filament grid,  $\theta$  is the corresponding angle,  $I$  the current of the particular grid point, and  $\alpha$  the field line inclination angle for the particular filament position. As the calculations are based on Biot-Savart, the code cannot cope with filaments that fly directly through the magnetic coil, i.e.  $d = 0$ . Such cases have been excluded, as they would require a very detailed knowledge on the filament position (mm-range) relative to the probe.

The calculations are repeated for every time stamp, and the filament is shifted according to its velocity. The time step is typically  $0.5 \mu s$ , corresponding to the sampling rate of the magnetic diagnostic. The starting point of the filament can, for example, be fixed by the time when a filament touches one of the Langmuir pins (thick ellipse in fig. 6.2). The starting point in the second plane is then given by mapping the filament along the

magnetic field lines (dashed line).

The result of the calculations are timetraces for  $B$  or  $\dot{B}$  for each coil used in that particular discharge. A comparison of the calculated magnetic signals to the measured signals allows to adapt the assumed filament parameters until the match is satisfactory.

In order to study different models for filament propagation, the following current distributions have been used:

- An uni-directional current distribution

$$j(r, z) = \exp \left[ - \left( \frac{r}{0.25\Delta_{rad}^*} \right)^2 - \left( \frac{z}{0.25\Delta_{pol}^*} \right)^2 \right] \quad (6.4)$$

with filament grid size  $\Delta_{rad}^* \approx 2\Delta_{rad}$ ,  $\Delta_{pol}^* \approx 2\Delta_{pol}$  and normalisation

$$I = \int_{fil} j(r, z) dA. \quad (6.5)$$

Such a distribution has been proposed in [42] and might occur, when filaments take along a fraction of the total plasma current. An illustration of the distribution is given in fig. 6.3 (top).

- A bi-directional current distribution

$$j(r, z) = \text{sgn}(z) \cdot \exp \left[ - \left( \frac{r}{0.25\Delta_{rad}^*} \right)^2 - \left( \frac{z - 0.35\Delta_{pol}^*}{0.1\Delta_{pol}^*} \right)^2 \right], \quad (6.6)$$

with  $\Delta_{rad}^* \approx 2\Delta_{rad}$ ,  $\Delta_{pol}^* \approx \Delta_{pol}$  and normalisation

$$2I = \int_{fil} |j(r, z)| dA. \quad (6.7)$$

Such a distribution has been predicted by the polarization model with parallel currents (sec. 3.2). Fig. 6.3 (bottom) gives a schematic view of such a distribution. Note that the distribution is shifted to the upper and lower edges of the filament, as the currents are expected to flow somewhere near the edge, and not close to the center of the filament.

### 6.1.2 Characterization for Uni- and Bi-Directional Current

In order to determine if the magnetic signature of filaments comes from an uni-directional current or from a bi-directional current, some characteristic differences between the simulation results for the 2 cases have to be worked out. Fig. 6.4 shows an overview of the calculated timetraces for the 2 different distributions. Solid lines show the magnetic signature of a bi-directional current, whereas dashed lines show the signature of a uni-directional current. The upper part (1) corresponds to filaments with a velocity ratio  $v_{rad} : v_{pol} = 1 : 1$ , the lower part (2) to filaments with lower poloidal and therefore dominant radial velocity,  $v_{rad} : v_{pol} = 1 : 0.2$ . An illustration of the motion of such filaments in the poloidal plane is given in fig. 6.2. The most important characteristics are:



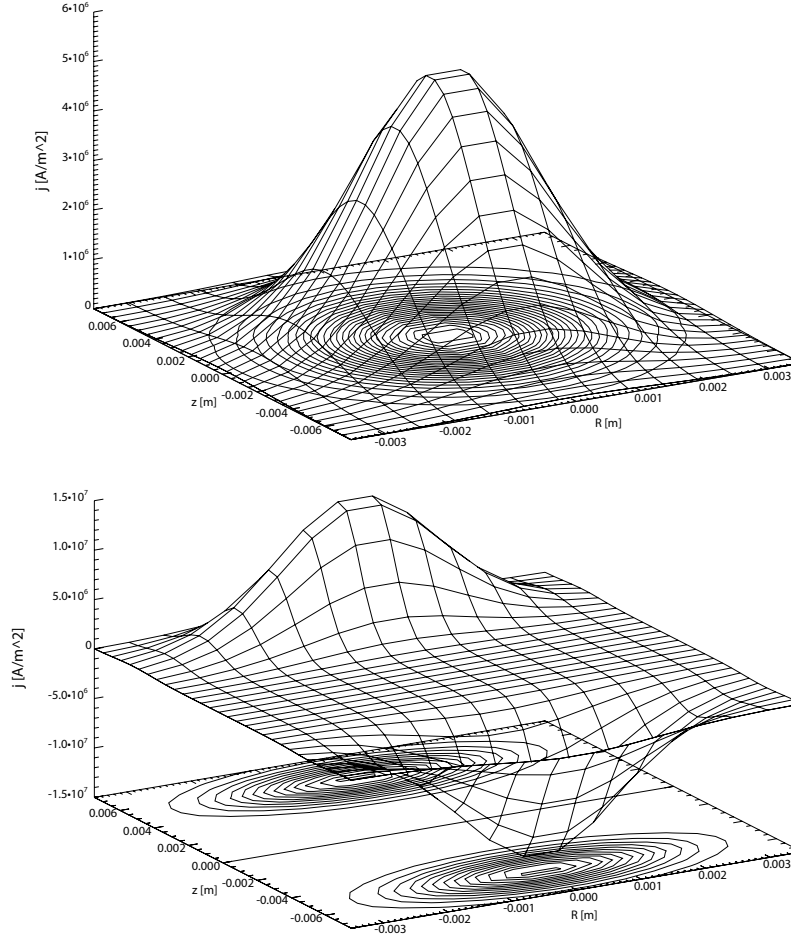


**Figure 6.3:** Uni-directional (top) and bi-directional current distribution (bottom). The filament grid size in this example is  $\Delta_{rad}^* \times \Delta_{pol}^* = 7 \text{ mm} \times 15 \text{ mm}$  with a total current of 100 A (according to definitions (6.5) and (6.6)).

- The uni-directional current gives a much broader signal, according to the slower decay of the amplitude of its magnetic field.
- The bi-directional current changes signs more often. This is also true for slope (first derivative) and curvature (second derivative) of the timetraces. Especially the rise of the signals can be used to distinguish between uni- and bi-directional current.
- The toroidal component is directly proportional to the poloidal component,  $B_{tor} : B_{pol} \approx \tan \alpha$ .
- The velocity ratio has a significant impact on the shape of the signal and adds additional zero crossings.
- The velocity ratio strongly affects the ratio between maximum and minimum of the signal: A high  $v_{rad} : v_{pol}$  yields a high  $\dot{B}_{pol,max} : \dot{B}_{pol,min}$  ratio.

These items should help in distinguishing the parameters of the measured filament. Additional variations occur depending on the position of the filament relative to the

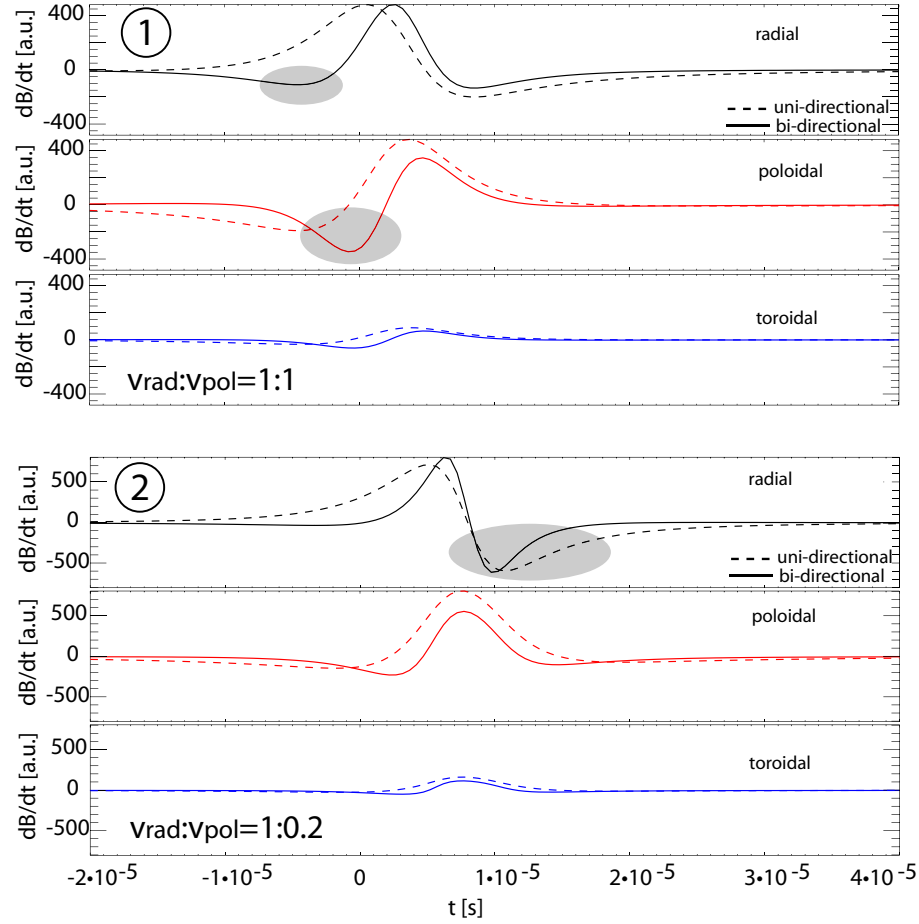


**Figure 6.4:** Comparison of the simulation results for uni- and bi-directional (dashed, solid lines) current and different velocity ratios (top, bottom). Shaded regions denote characteristic differences in the signals.

coil as we will see farther down.

## 6.2 Application to Measurements

### 6.2.1 Filament-Based Model

The calculation results will now be fitted to the measured data in order to derive the parameters of the filaments. Fig. 6.5 shows the magnetic measurements from fig. 6.1 with timetraces from calculations with uni- and bi-directional currents. A filament with  $\Delta_{rad}^* = 7$  mm,  $\Delta_{pol}^* = 15$  mm, i.e. in the order of the most probable values from sec. 5, has been used. The velocities are slightly higher than the most probable values, with  $v_{rad} = 2.2$  km/s and  $v_{pol} = 3.2$  km/s, but well within the measured velocity range. From the features cited above, one can clearly see that the bi-directional current gives a far better match than the uni-directional one. The shape of the uni-directional current is too broad to match the data due to the longer decay length. This could be improved by making the filament smaller and/or faster. Raising the velocity would, however, lead farther away from the most probable values, whereas reducing the filament size

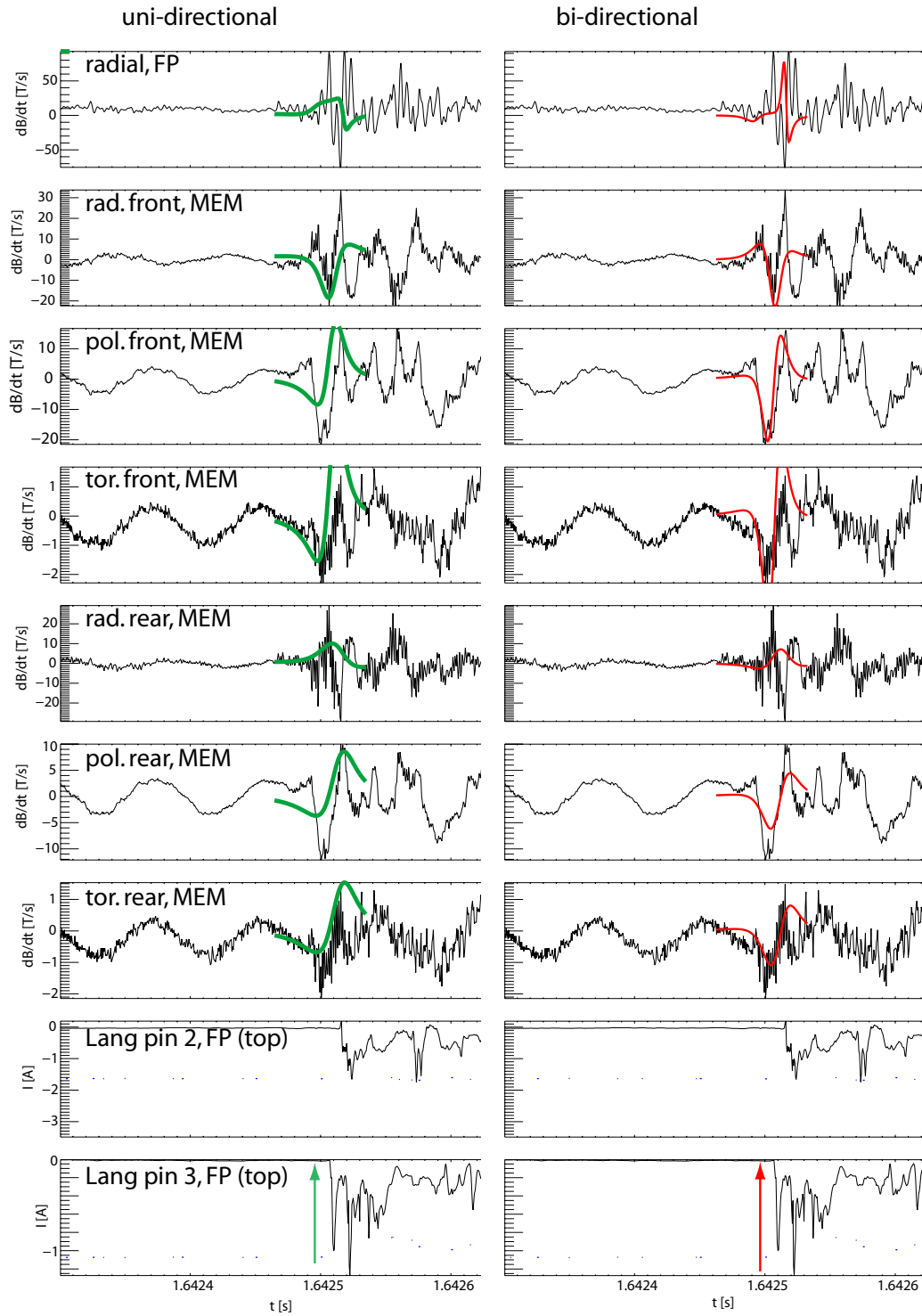


**Figure 6.5:** Left: Matching the measurement with an uni-directional current with  $I = 60$  A. Right: Bi-directional current with  $I = 150$  A. Filament parameters:  $\Delta_{rad}^* = 7$  mm,  $\Delta_{pol}^* = 15$  mm,  $v_{rad} = 2.2$  km/s,  $v_{pol} = 3.2$  km/s. The arrow denotes the point where the filament touches pins 2 and 3 in the calculations.

would not help much in matching the signal, as the shape (in particular the rise at the beginning) is not reproduced correctly. See for example the first radial component at the beginning, which is not reproduced by the uni-directional current (where the signal falls) but by the bi-directional current (where the signal rises correctly).

The derived filament parameters are strongly dependent on each other and, to some extent, even exchangeable so that they can not be fully determined. For example, the amplitude of the magnetic signature is influenced by the current in the filament, the total velocity of the filament (as we are watching  $\dot{B}$ ), and the distance to the coil. An illustration of these dependencies is shown in fig. 6.6: Changing the velocity will strongly

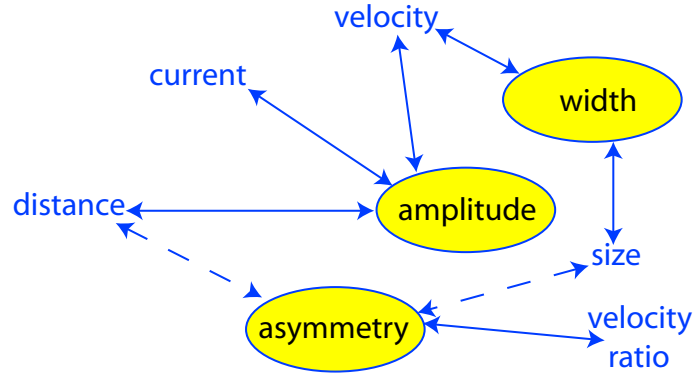


**Figure 6.6:** Parameter dependencies for the determination of filament properties from the magnetic signature. Solid lines indicate strong influences, dashed lines denote weak dependencies. Multiple dependencies make the full determination difficult, but additional information can strongly reduce the parameter space.

influence the width of the signal, which in turn will influence the size of the filament. Distance and size are, however, weakly coupled to the asymmetry of the signal, which is a measure of how far the signal is influenced by the dipole structure of the filament. The exchangeability of the parameters allows for variations in the parameters, in particular as the measured signal is noisy and the fit just an approximation to that signal. Just to give an example, it would be possible to get an adequate fit with  $v_{rad} \approx 5$  km/s and larger filaments with  $\Delta_{pol} \approx 4$  cm, but these values are far from the most probable values derived in chapter 5. The interpretation of the magnetic measurements can therefore be greatly improved by using additional information on the particular filament.

The arrows in fig. 6.5 denote the point in the calculations, where the assumed filament touches the 2 upper Langmuir pins (pins 1 and 3) according to the calculations. However, no signal is visible on the Langmuir data at that time. Both diagnostics, Langmuir and magnetics, are based on the same timing system, so that the offset should not be of technical nature. A perfect match to the data, including not only the magnetics but also the Langmuir data, could only be observed in very few cases, raising first doubts on a correlation between magnetic signature and filaments.

In the parallel current model with bi-directional current distribution, the polarization always has to be the same, as the toroidal magnetic field does not change its topology and the particle drifts do not change their direction. Observations of an inversed current distribution by changing signs would be a clear contradiction to that model. But changing signs could also be caused by the position of the filament relative to the magnetic coil: If  $v_{rad}$  is the dominant velocity, one would expect that approximately

half of the filaments passes below the coil and the other half passes above the coil. If  $v_{tor}$  is dominant, one would expect that the filaments always hit the probe at the upper right corner. The first case should give significant variations in the magnetic signature, depending on the positions of the filaments, whereas the latter cases would always yield equal signs. A summary of possible combinations is given in fig. 6.7. A series of 65

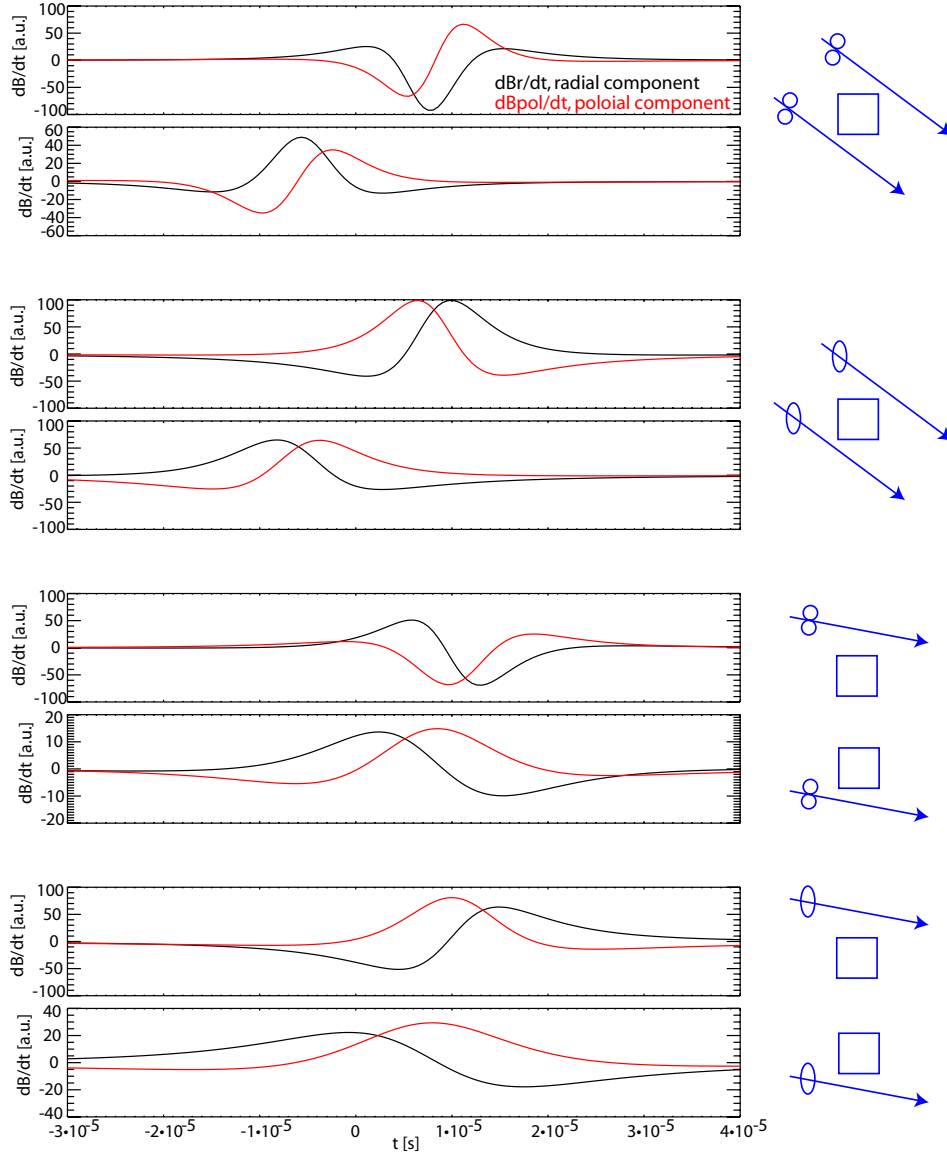


**Figure 6.7:** Illustration of the dependency of the magnetic signal on the filament position and velocity ratio  $v_{rad} : v_{pol}$ . The motion of the filaments relative to the 3D coilset is indicated on the right side. The resulting signal is characteristic for the filament motion and can be used to derive the filament dynamics from magnetic measurements alone.

filaments has been analysed in order to check sign variations in the measured data. No clear evidence that would indicate a reversed polarization has been found. Virtually all filaments hit the probe at the same side, which is in agreement with the measurements from chapter 5, which predict  $v_{tor} \gg v_{rad}$ .

The code has undergone substantial testing and has been found to match quite well with a similar but simpler code that has been used at MAST [42]. This code has initially not been able to calculate bi-directional currents and is not suited to calculate current distributions. For the filament shown above, the predicted currents have been in the order of 100 A, which according to fig. 6.3 yields current densities in the order of 6 A/mm<sup>2</sup> for an uni-directional current and 15 A/mm<sup>2</sup> for a bi-directional current. According to the parallel current models described in chapter 3, this current has to be carried by the particles in the filament. An upper limit to that current is given by the ion saturation current. With temperatures of  $T_i = 30 - 60$  eV and  $T_e = 5$  eV, and filament densities of  $n_{fil} = 2.6 \cdot 10^{18} \text{ m}^{-3}$ , the ion saturation current in a filament should be

$$j_{sat} = nec_s = ne \sqrt{\frac{k(T_e + T_i)}{m_i}} \approx 0.02 \text{ A/mm}^2. \quad (6.8)$$

This ion saturation current is by 2 orders of magnitude smaller than the required current, i.e. the required current can not flow in a filament with the given parameters. The filaments would have to be much bigger and much faster to reduce the required current, or they would have to be much hotter or more dense to allow higher currents. A variation of the sheath current model has been proposed in [71], where the currents are closed not at the sheaths, but near the X-point because of the shearing of the filament there. This model avoids the reduction of the current by the plasma sheath resistivity and thus allows higher parallel currents. But this is not useful in explaining the required currents, because the estimate from eq. (6.8) neglects any resistivity at the target tiles or close to the X-points: It is solely based on the number of particles and their temperature, and assumes that all ions contribute to the current.

If the current would only be carried by the electrons, this would lead to a net drift of the filament in the ion drift direction, which has neither been observed in the experiment nor in theory.

Altogether, the required current densities generally are un-physically high, in particular because the magnetic signature has been measured close to the midplane, where the current should be minimal according to fig. 3.2, i.e. according to the parallel current models, we would expect an even stronger magnetic signature farther away from the midplane, which would require even higher current densities there. In order to be fully consistent with the models, the ion saturation current density measured with the filament probe should always be higher than the current density required for the magnetic signature.

### 6.2.2 Mode-Based Model

The filament-based model is not very convincing when it comes to explain the magnetic signature of an ELM, in particular with regards to the required current densities, and the timing problems. The signal itself is, however, matched very well by the bi-directional current, which leads to a new, mode-based ansatz to explain the magnetic signature: Rotating helical structures with a bi-directional current close to but inside the separatrix could give a similar magnetic signature. These modes would not be directly correlated to the Langmuir signals, so that the modes would not have to coincide with the Langmuir signal directly (a mechanism for indirect correlation is described below).

The calculation program described above has been used to calculate the magnetic signature of a mode structure that rotates at the pedestal region. A current distribution similar to the bi-directional filament model has been used, but with a sinusoidal distribution in poloidal direction, which is typical of magnetic modes in the core plasma [93, 94, 40]. The following parameters have been used, based on typical numbers of core MHD modes:  $\Delta_{pol}^* = 300$  mm,  $\Delta_{rad}^* = 10$  mm,  $v_{pol} = 16.5$  km/s. The radial velocity has been chosen to be  $v_{rad} = 5$  km/s in order to match the separatrix shape close to the probes. The resulting magnetic signature is shown in fig. 6.8. In general, the match is quite good, in particular for the coils on the midplane manipulator, where the match is as good as it was for the filament-based model with bi-directional current. This is mainly due to the exchangeability of the different parameters, meaning that we have matched the amplitude with a different combination of velocity, distance and total current as shown in fig. 6.6. The resulting minor differences with respect to asymmetry and dipole structure can be inferred from fig. 6.8.

A total current of 140 A has been used, resulting in a current peak density of  $350$  kA/m<sup>2</sup>, which is in the order of the edge current density ( $j_{q95} \approx 0.3 \cdot 10^6$  A/m<sup>2</sup>) [95]. Again, it is possible to exchange some of the parameters, e.g. to raise the poloidal velocity at the expense of poloidal size. The rotation has been chosen to be poloidally upwards as we will see farther below.

In principle, the magnetic coil on the filament probe should deliver a very good signal for large modes, but the signal is obviously very noisy, compared to the coils on the midplane manipulator probe. This might be due to a non-shielded twisted-pair cable, which has been used to connect electrically the magnetic coil to the vacuum flange. Although other coils of that type use a similar wiring, the signal-to-noise ratio does not seem to be that good on the filament probe. The coils on the midplane manipulator probe are connected by coaxial wiring and seem to be perfectly shielded.

The time onset used for the calculations is indicated by the arrow in fig. 6.8 and is right at the beginning of the filamentary activity. A mechanism that links the assumed modes to the formation of filaments has been proposed in [96], where rotating magnetic helical structures have been described as remnants of mode structures that have caused the formation of the filaments by locally changing the magnetic field. The filaments then grow explosively, e.g. as described in [52, 58], separate from the core plasma and propagate radially outwards. According to this approach, a filament is generated when the mode is close to the separatrix at the low field side. As the filament propagates through the SOL, the mode still rotates for a short period and decays afterwards. In that period, the mode can be seen on the magnetics if the coils are close enough to the plasma. Coils that are more remote can probably not see these modes, as the magnetic signature seems to decay quickly with distance.

In order to re-establish a correlation between the mode remnant to the signal on the Langmuir pins, one has to keep in mind that a mode with  $v_{pol} \approx 16$  km/s travels over the whole height of the core plasma, i.e. from the plasma bottom to the top, in the time the filament takes to travel from the separatrix to the Langmuir probes.

Among the magnetic coils mentioned up to now, there are several other magnetic pick-up coils -similar to the one in the filament probe- installed in the ASDEX Upgrade vessel: One set of these coils forms a poloidal array that spans over the low field side as indicated in the insert in fig. 6.9 (right, top). This set of coils is usually used to determine poloidal mode numbers of MHD modes that rotate in the core plasma. These coils can be used here to determine velocity and direction of the ELM mode remnants



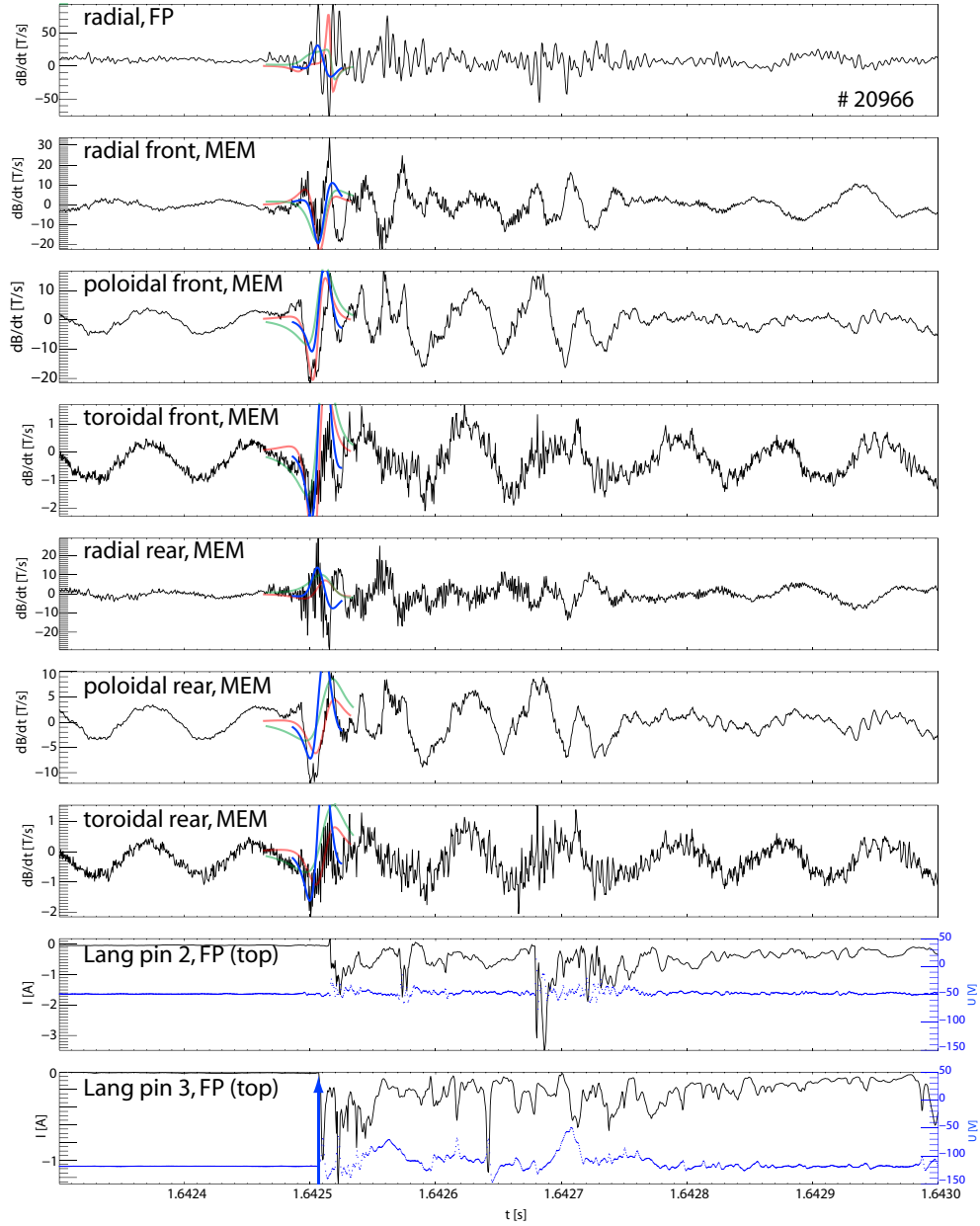


**Figure 6.8:** Matching the magnetic measurement with a mode rotating close to the separatrix (blue). Mode parameters:  $\Delta_{rad}^* = 10$  mm,  $\Delta_{pol}^* = 300$  mm,  $v_{rad} = 5$  km/s,  $v_{pol} = 16.5$  km/s. Calculations from the filament-based model, fig. 6.5, are indicated by lighter colours.

that might be responsible for the filament formation process. Fig. 6.9 shows the time traces of this poloidal coil array. Magnetic structures are clearly visible and can be traced over several coils. The most dominant one can be traced over 6 coils and rotates poloidally upwards with a velocity of about 20 km/s, which is close to the velocity we have assumed for the calculations. The rotation poloidally upwards is identical to the electron drift direction or the pedestal  $\mathbf{E} \times \mathbf{B}$  direction

In order to make a clear correlation between the measurements on filament probe or



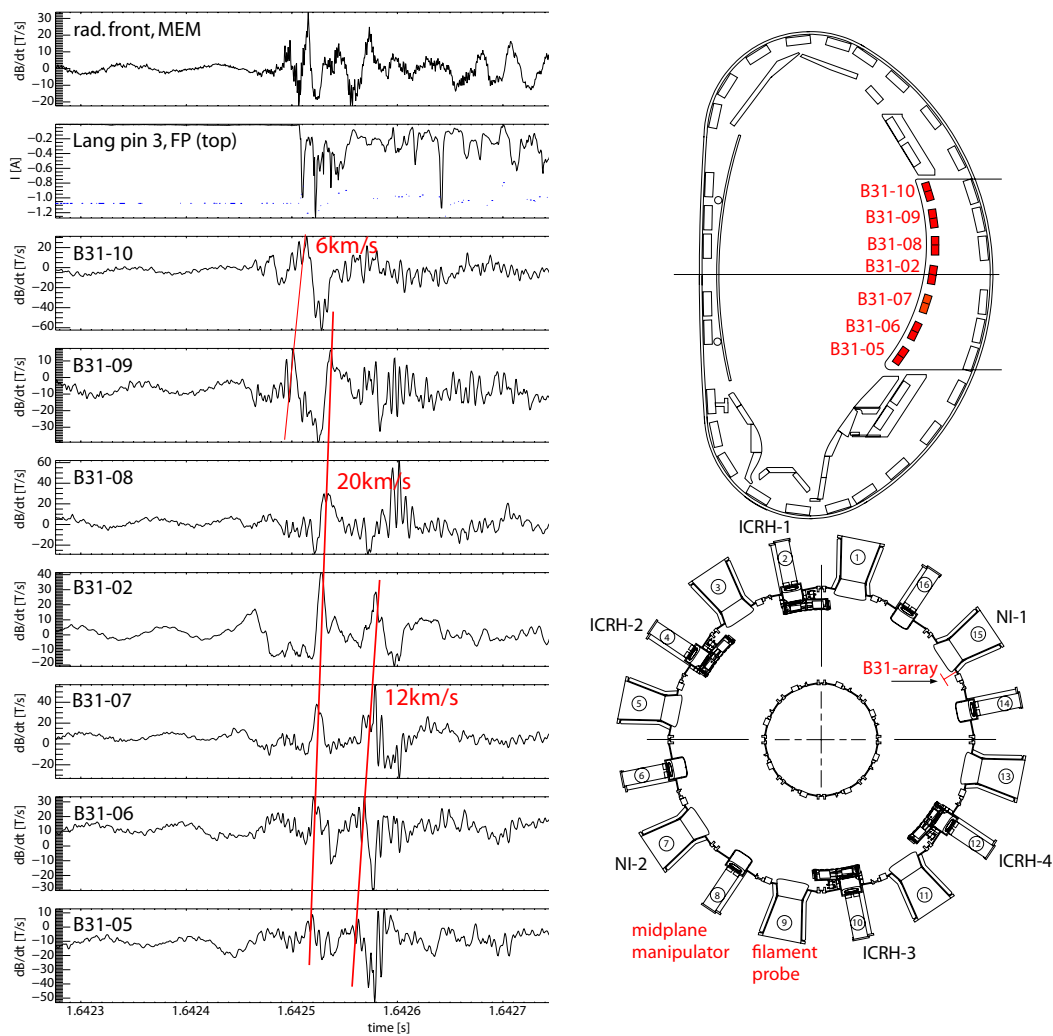


**Figure 6.9:** Timetraces of a poloidal magnetic coil array at the low-field side of ASDEX Upgrade. The position is shown in the poloidal plane (top, right) and in the toroidal plane (bottom, right). The structures can be traced over several coils and the observed poloidal rotation velocities are in the order of the values used for the calculations. The rotation is directed poloidally upwards, i.e. with the electron drift or pedestal  $\mathbf{E} \times \mathbf{B}$  direction.

midplane manipulator probe and the poloidal coil array, a direct connection along a field line would be necessary. Unfortunately, such a connection is not available, as the filament probe or midplane manipulator probe map far above the poloidal coil array when mapped along field lines. The probes can not be easily rearranged to get a better correlation, so that this question has to be left open here. Nevertheless, it can be stated already that the magnetic signature of ELMs could probably be explained by mode structures rotating close to but inside the separatrix. The required values fit very well to the edge parameters, so that further studies should be carried out as soon as possible.



## Chapter 7

# Temperature of Filaments

### 7.1 Heat Flux Measurements

Many discharges have been recorded with infrared thermography (see description in sec. 4.3) in order to evaluate the filamentary heat flux to plasma facing components such as the filament probe, the midplane manipulator probes, and limiters. The camera view is shown in fig. 7.1: The probes and the protection limiter can be observed via a gold-

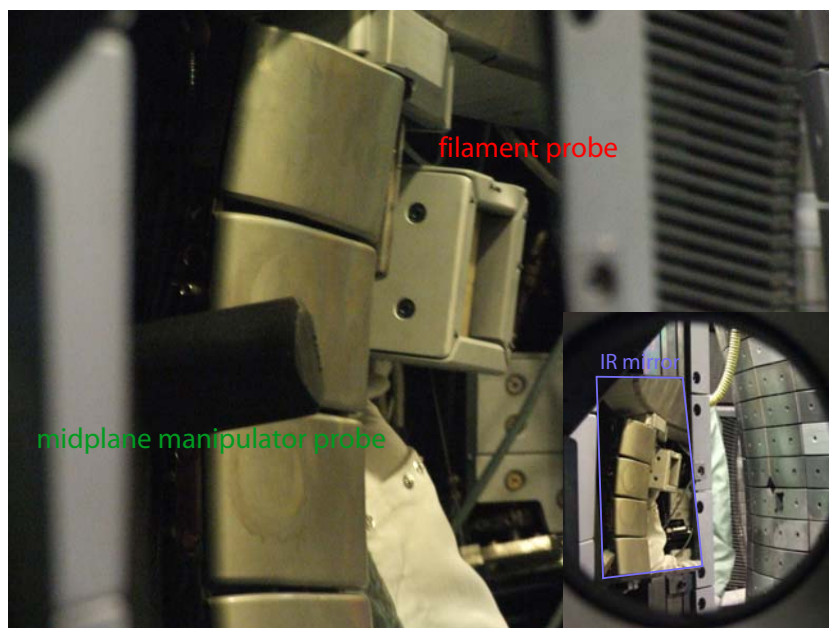


**Figure 7.1:** Photograph of the view through the infrared thermography port. Filament probe and midplane manipulator can be seen via a gold-coated mirror (marked in blue). The motion of the mirror has to be corrected for calculations of the heat flux.

coated mirror, which is installed in the ASDEX Upgrade vessel. During discharges, the mirror wobbles due to motions of the vessel. The movement is corrected offline in order to avoid artefacts in the heat flux calculations. Small window sizes have been chosen to obtain a high time resolution in the order of 10 kHz. Smaller windows would allow a higher time resolution, but will lead to a temporary loss of the probe as it moves out of

the image. An example for the resulting photon flux is given in fig. 7.2. Brighter spots

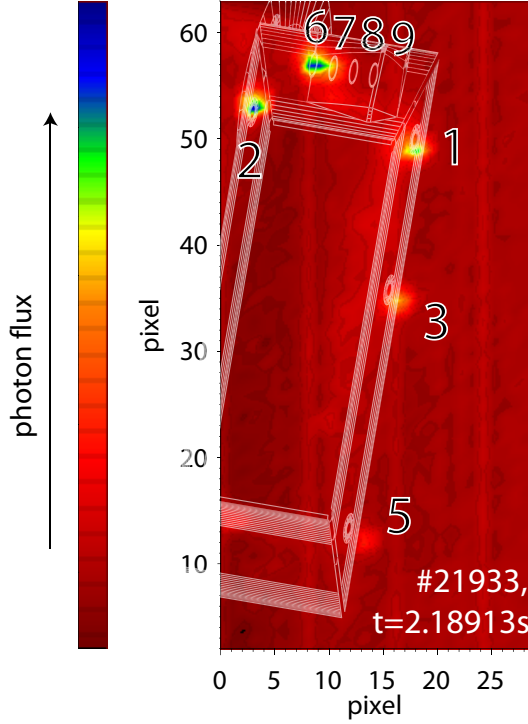


**Figure 7.2:** Thermography measurement (photon flux) of the filament probe. Brighter spots denote higher temperatures, e.g. at the Langmuir probe tips. The CAD drawing of the filament probe has been overlaid in white to clarify the geometry.

correspond to a higher photon flux and thus to higher temperatures. The heat flux calculated from the temporal evolution of the measured temperature can be compared to the heat flux derived from the probe measurements. The heat flux from a magnetized plasma along field lines is given by

$$q_{\parallel} = \gamma_s n_{fil} c_s T_e = \gamma_s T_e j_{sat} / e \quad (7.1)$$

with the sheath transmission factor  $\gamma_s$ , which accounts for the cooling of electrons and the heating of ions in the sheath [68, 65]. According to [65], the sheath transmission factor is given by

$$\gamma_s = \frac{2}{1 - \gamma_e} + \frac{2.5 T_i}{T_e} - 0.5 \ln \left[ \frac{2 \pi m_e}{m_i} \left( 1 + \frac{T_i}{T_e} \right) \frac{1}{(1 - \gamma_e)^2} \right], \quad (7.2)$$

where  $\gamma_e$  is the secondary electron emission coefficient. For low temperatures ( $< 100$  eV),  $\gamma_e$  increases with  $T_e$  and is for example about 0.7 for tungsten [97] and graphite [98] at  $T_e \approx 50$  eV.

Assuming that the heat flux to the probe is dominated by ions, and is thus described by eq. (7.1), a comparison of the measured ion saturation current and the thermographically calculated heat flux (see fig. 7.3) allows to deduce electron and ion temperatures:

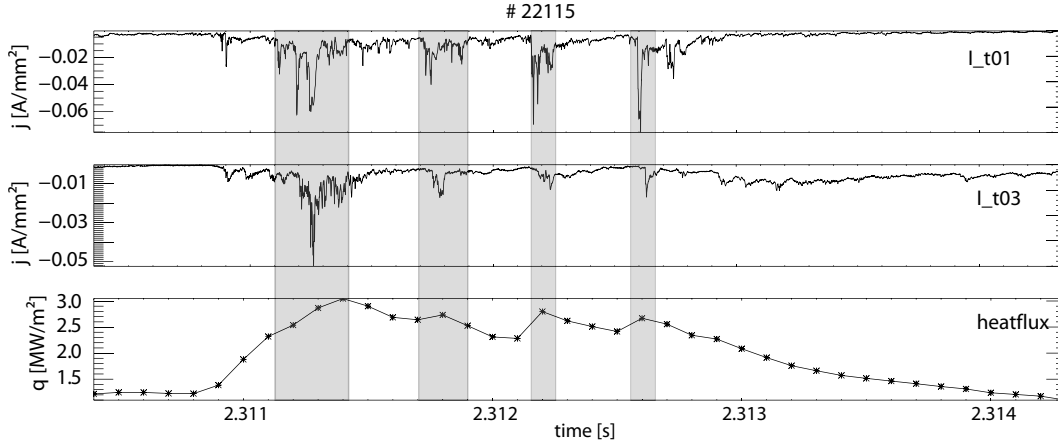


**Figure 7.3:** Timetraces for heat flux and ion saturation current onto the filament probe. The heat flux has been calculated from thermographic measurements close to Langmuir pins 2 and 3.

$$\frac{q_{\parallel e}}{j_{sat}} = \gamma_s T_e \approx 60 - 150 \text{ eV}. \quad (7.3)$$

A temperature  $T_i/T_e \approx 3$  has been proposed in [37] after a series of calculations with both kinetic and fluid codes, giving a sheath transmission factor  $\gamma_s \approx 10$  [65]. This leads to filament temperatures  $T_e \approx 6 - 15 \text{ eV}$  and  $T_i \approx 20 - 50 \text{ eV}$  at the filament probe. From a similar analysis in 2006 with a carbon machine,  $T_e \approx 10 - 20 \text{ eV}$  and  $T_i \approx 30 - 60 \text{ eV}$  have been derived [68] (see also fig. 2.6).

## 7.2 Heat Loss Mechanisms

Parallel heat loss can be caused by various mechanisms, in particular by heat conduction and heat convection. The equations describing these mechanisms are [65]:

$$q_{\parallel e, cond} = \kappa_e T_e^{5/2} \nabla T_e \approx 2000 T_e^{7/2} / l_{\parallel} \quad (7.4)$$

$$q_{\parallel i, cond} = \kappa_i T_i^{5/2} \nabla T_i \approx 60 T_i^{7/2} / l_{\parallel} \quad (7.5)$$

$$q_{\parallel e, conv} = \frac{5}{2} k T_e n v_e \quad (7.6)$$

$$q_{\parallel i, conv} = \left( \frac{1}{2} m_i v_i^2 + \frac{5}{2} k T_i \right) n v_i. \quad (7.7)$$

Heat conduction is dominated by the electron branch, so that the total amount of heat conduction is  $q_{\parallel, cond} \approx 2000 T_e^{7/2} / l_{\parallel}$ . Heat convection can be approximated to be  $q_{\parallel, conv} \approx 5.5 m_i^{-1/2} n (kT)^{3/2}$  with  $v \approx c_s$ . A graphical representation of these equations is given in fig. 7.4: For high filament temperatures, which prevail in the initial phase right after the formation of the filament, the dominant heat loss mechanism should be heat conduction by electrons. This reduces the electron temperature and, hence, the electron contribution to the heat conduction until electron and ion contribution become equal at  $T_i/T_e \approx 2.7$ . For smaller temperatures, heat convection becomes dominant over heat conduction.

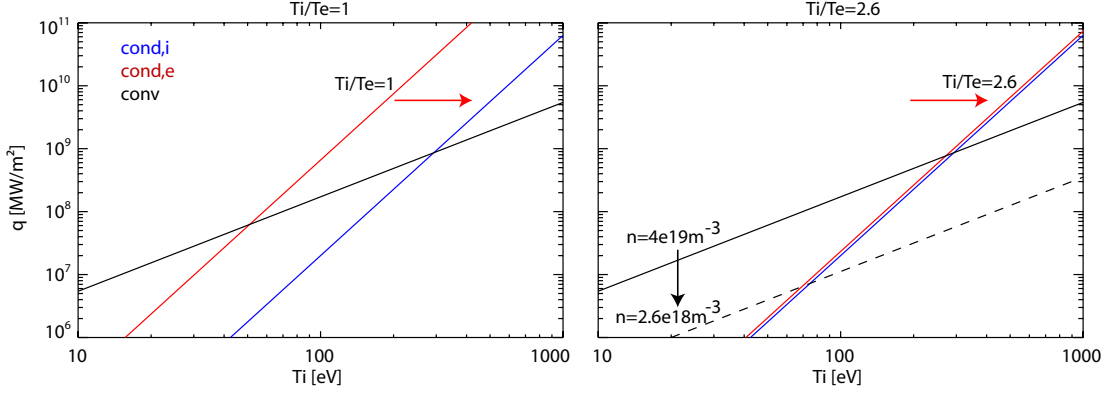


**Figure 7.4:** Heat fluxes from eqns. (7.7) for  $T_i/T_e = 1$  (left) and  $T_i/T_e = 2.6$  (right) with  $l_{\parallel} = 30$  m. For high temperatures, heat conduction by electrons is the dominant loss mechanism. The electron contribution decreases with decreasing electron temperature until electron and ion contribution become equal at  $T_i/T_e \approx 2.7$  (right). For smaller temperatures, convection becomes the dominant loss mechanism, but decreases with decreasing density.

The filaments are therefore expected to lose their energy by heat conduction in the initial phase, and by heat convection in a later stage. The detailed partition between the different loss channels depends on the detailed parameters in each phase (heat convection decreases with decreasing density, etc.). In [37], numerical calculations have been carried out based on both fluid and kinetic codes. The calculations are performed in the filament frame of reference, hence neglecting radial motion of the filament. Similar to the simple approach above, the electrons are lost much faster than the ions with a transport time ratio of  $\tau_{\parallel i}/\tau_{\parallel e} \approx 60$ . With regards to charge neutrality, a weak quasi-neutrality constraint has been imposed in the calculations, permitting violations of ambipolar flow of particles in the initial phase  $\tau < \tau_{\parallel i}$ , and requiring quasi-neutrality in later stages, forcing the fluxes to converge as shown in fig. 7.5. The calculations

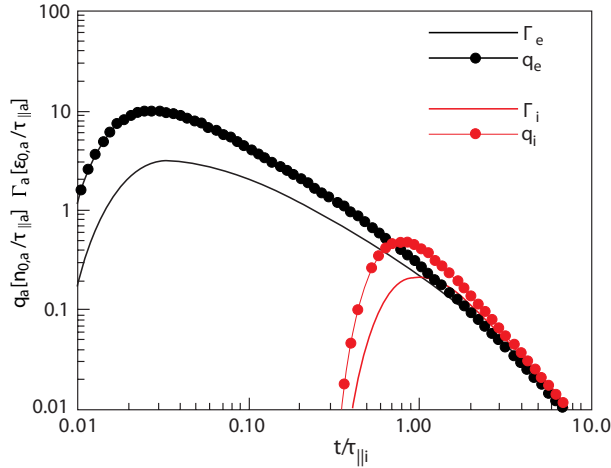


**Figure 7.5:** Heat and particle fluxes from a filament to the target tiles [37]. A weak quasi-neutrality constraint allows for violation in the initial phase ( $\tau < \tau_{\parallel i}$ ), but forces the fluxes to converge afterwards. This leads to a electron heat flux in the initial phase.

suggest that inertial effects govern the arrival times of the particles, whereas sheath effects determine the magnitudes. Secondary electron emission has been neglected in these studies but has been found in [99] to increase the initial heat transport, which is due to the fast electrons.

Comparing the decay lengths of ion saturation current and temperature allows to characterize the importance of the different heat loss mechanisms experimentally. In [68], we could already show that the decay lengths of heat flux and density are equal and in the order of 2.5 cm, see fig. 7.6. According to eqns. (7.7), identical decay lengths for

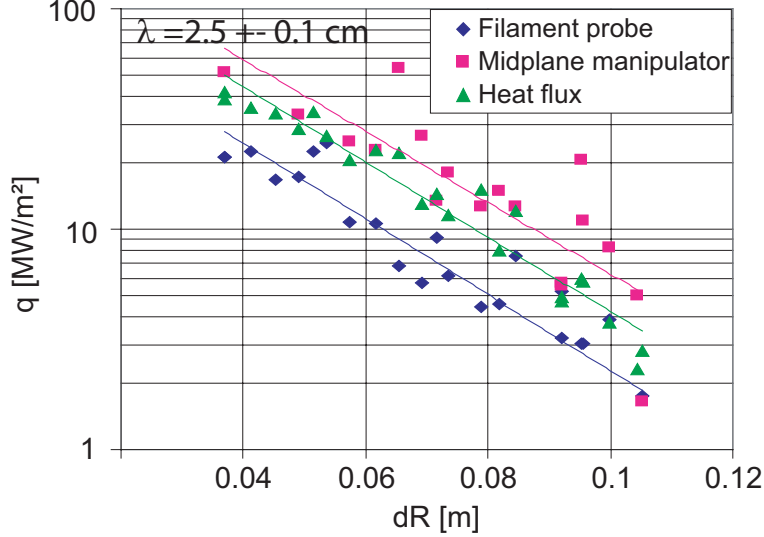


**Figure 7.6:** Heat load decay lengths as measured by Langmuir probes (assuming  $\gamma_s T_e = 100$  eV) and infrared thermography. The resulting decay lengths are about 2.5 cm.

heat flux and ion saturation current indicate that the heat loss is mainly due to a loss of density. Temperature losses seem to be secondary ( $\lambda_n < \lambda_{T_i}$ ), so that heat conduction ( $\propto T_e^{7/2}$ ) has to be much smaller than heat convection ( $\propto nT^{3/2}$ ), which is exactly what is expected for small temperatures as described before (fig. 7.4).

The decay length measurements have been repeated in 2007 in a tungsten machine and seem to confirm the 2006 results, but are far more difficult to evaluate because the achievable ELM size was lower in the tungsten machine. It seems that the number of filaments per ELM increases for smaller ELMs and that the size of the filaments decreases. This makes it more difficult to resolve and separate the filaments in the heat flux measurements.

### 7.3 Triple-Probe Measurements

During short events such as filaments, it is not possible to derive detailed information on temperature or density from single Langmuir probes alone, as this would require lengthy measurements of the complete voltage-current characteristic. A combination of 3 probes, a so-called triple probe, however, reveals the most important parameters at full time resolution (2 MHz in our case). Drawbacks are possible misinterpretations of the data, when certain assumptions necessary for triple probe evaluation are violated.

These problems could, of course, be recognised from the complete voltage-current characteristic, but do not appear on the triple probe measurements alone [100].

Technically, a voltage  $U_B$  is applied between two adjacent electrodes, and the floating potential is measured by a third electrode. The probe bias self-arranges in a way such that the currents through both electrodes add to zero. Fig. 7.7 shows the measurement

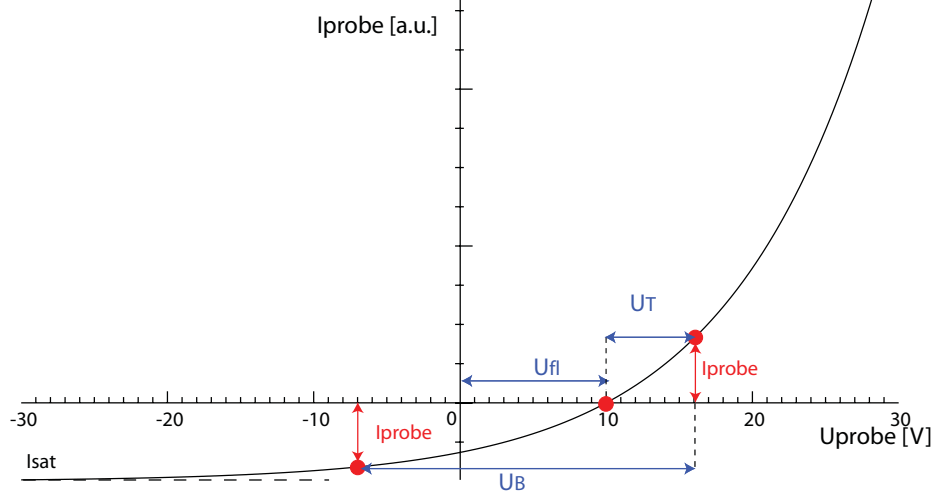


**Figure 7.7:** Measuring scheme for a triple probe: a voltage is applied between two adjacent electrodes; the floating potential is measured by a third electrode. The voltages distribute in a way that the current through both electrodes becomes equal. Using  $U_B$ ,  $U_T$  and  $U_{fl}$  allows to calculate the electron temperature  $T_e$  at the probe tip with full time resolution (2 MHz).

points in the voltage-current characteristic.

Care has to be taken with respect to the voltage  $U_B$ : On the one hand, the values should not be too high in order to prevent arcs, but on the other hand should not be too low in order to keep the evaluation simple. In general, the total current balance through the 2 pins,

$$1 + e^{U_T - U_B/kT_e} + 1 - e^{U_T/kT_e} = 0, \quad (7.8)$$

has to be solved [100] to calculate the electron temperatures. For high  $U_B$ , the ion saturation current is reached, so that eq. (7.8) simplifies to

$$kT_e = U_T / \ln 2. \quad (7.9)$$

In [100], it has been shown that this assumption is valid for  $U_B > 5U_T$ . For values below that point, i.e. for low  $U_B$  or for high temperatures, the approximation

$$e^{U_T/kT_e} = 2 \frac{\alpha^{2.1}}{1 + \alpha^{2.1}}, \quad \alpha = \frac{U_B}{U_T} - 1 \quad (7.10)$$

can be used.

A triple probe setup has been developed for the new 2 MHz data acquisition system. The setup has been tested against routinely operated triple probes in the divertor and has afterwards been applied to the midplane manipulator probe. A battery voltage  $U_B$  of about 105 V has been used. The resulting timetraces are shown in fig. 7.8. The sig-



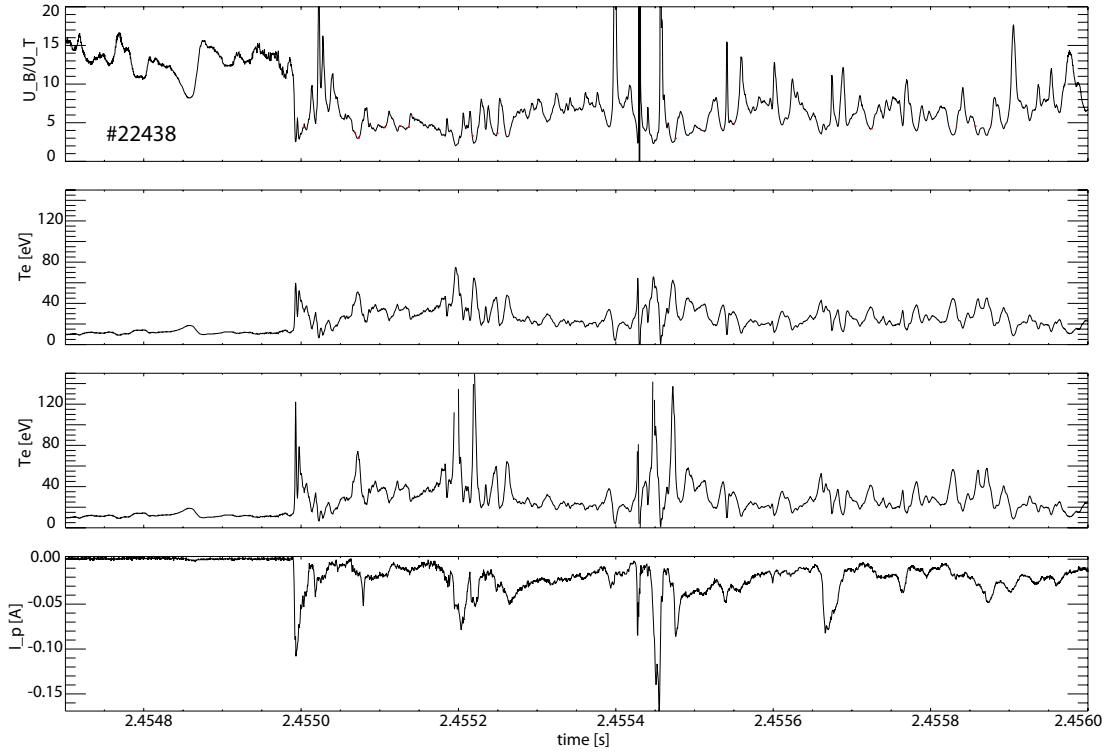


**Figure 7.8:** Timetraces of the triple probe measurements during a type-I ELM. The signals are (from top to bottom): voltage ratio  $U_B/U_T$ , electron temperature  $T_e$  based on eq. (7.9) (valid for  $U_B > 5U_T$ ),  $T_e$  based on the simple analytical expression from eq. (7.10) and the current through one of the two current probe tips. The latter signal serves to detect the filaments. The obtained electron temperatures are surprisingly high, ranging between 80 and 140 eV.

nals are (from top to bottom): the voltage ratio  $U_B/U_T$ , electron temperature  $T_e$  based on eq. (7.9) and on eq. (7.10), and the current through one of the two current probe tips. The latter can be used to detect impinging filaments, but must not be confused with an ion saturation current measurement. The first signal shows the ratio  $U_B/U_T$ , which during filaments drops below 5, so that the simple approximation from eq. (7.9) is no more valid. The analytic formula gives higher temperatures in these cases, but diverges when  $U_B/U_T$  becomes very small, i.e. when the temperatures go above 150 eV. The electron temperatures obtained from these triple probe measurement are surprisingly high, ranging between 80 and 140 eV and are not in agreement with the results obtained from a Langmuir/thermography comparison. Triple probe measurements in MAST have also shown surprisingly high electron temperatures of 50 – 100 eV[101]. These should, however, yield a more pronounced heat conduction, and accordingly a bigger difference in heat loss decay lengths. With a pin distance much smaller than the filament, geometric effects (i.e. probe tips feeling the ellipticity on the filament) should not play a role. But it might be possible, that the tips measure the internal inhomogeneity of the filament because of an internal fine structure.

## 7.4 Filament Detachment

The energy content of a filament is given by  $W_{fil} = 3/2nk(T_e + T_i) \cdot Vol_{fil}$ . With a length of about 30 m, an extent of  $\Delta_{rad} \times \Delta_{pol} = 2.7 \text{ cm} \times 0.8 \text{ cm}$ , an initial density of  $3.5 \cdot 10^{18} \text{ m}^{-3}$  and initial temperatures  $T_e = 100 \text{ eV}$ ,  $T_i = 500 \text{ eV}$ , the energy content of a single filament right after its formation is in the order of 2 – 5 J. The total energy loss per type-I ELM in ASDEX Upgrade is about 10 – 15 kJ (see sec. 2.1), so that even 10-15 filaments will account for less than 0.5% of the total ELM energy loss.

Apart from this model of a completely detached filament, 2 additional models have been proposed in [59] to explain the total ELM energy loss. The 3 models are (see fig. 7.9 for an illustration):

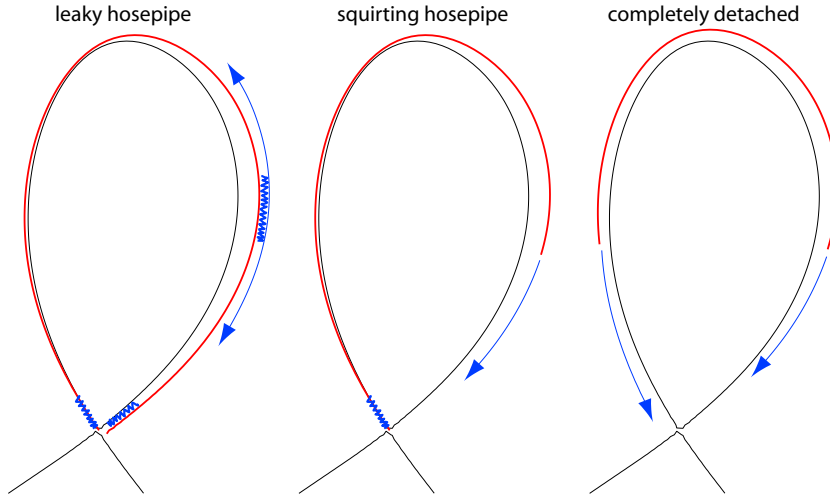


**Figure 7.9:** Illustration of the 3 models for filament detachment: leaky hose pipe (attached to the core plasma at both ends with diffusive transport of heat to the scrape-off layer), squirting hose pipe (1 attached and 1 detached end, acting as a direct conduit for losses) and completely detached filament (no connection to the core plasma).

- **leaky hose pipe**

The filament is ejected at the low-field side near the midplane, but stays connected to the plasma at its ends, where the displacement is small. The strong pressure gradient between the hot filament and the cold, surrounding SOL leads to strong diffusion, and hence to a transport of heat to the SOL. There, the heat flows along the field lines and thus goes to the divertor or other plasma facing components at the end of the open field lines. Because the filament remains connected to the core plasma, much more energy than its energy content can be released.

In brief, the filament acts as a conduit for losses with a diffusive passage, i.e. as a leaky hose-pipe.

- **squirting hose pipe**

The filament detaches from the plasma close to the lower X-point, separating it from the plasma at only one end, serving as a direct conduit for losses from the core plasma to the SOL.

- **completely separated**

If the filament separates at both ends, it will lose its particle content by parallel losses, the lost energy being equal to the energy content of the filament.

As discussed before, filaments are expected to lose most of their energy directly after their formation. This implies that the filaments have already lost most of their energy when being observed by most edge diagnostics. In MAST, filaments have been found not to move radially within the first  $50\mu\text{s}$  from their generation [41]. This can be explained by the time the filament takes to lose enough temperature, so that it can move outwards by magnetic reconnection (e.g. at the ends) through finite resistivity [31]. Unfortunately, the energy deposition of single filaments in the initial phase can not be resolved by infrared thermography, as the filament deposition falls very close to the separatrix strike-line [20], where its footprint is smeared out due to X-point effects. In [41], the energy content of travelling filaments has been estimated to be  $< 2.5\%$  of the total ELM energy loss with further reduction by parallel transport as the filament moves outwards. From the measurements presented here, the energy content of filaments is far from the total energy loss per ELM, even if they lose most of their energy right after the formation process. Therefore, it seems mandatory that filaments are somewhat connected to the core plasma and act as a conduit for losses. First attempts have been made in MAST to resolve a detachment process near the X-points, but so far without positive evidence [87]. It is thus not possible to say what happens close to the X-point, in particular, whether the filaments are attached to the core. The MAST data show at least, that the filaments do not detach directly at the X-point.



## Chapter 8

# Summary and Outlook

The aim of this thesis was to characterize type-I ELM induced filaments on ASDEX Upgrade. This is necessary for understanding the ELM cycle (with the ELM crash being initiated by the explosive growth of a peeling-ballooning mode), filamentary transport in the scrape-off layer (SOL), and the energy deposition due to filamentary transport. Extrapolations to future fusion devices are necessary to calculate the consequences of filamentary transport for these machines, which becomes important because several remote surfaces that are hit by filaments are not designed to withstand high heat loads. The heat deposition to non-divertor components depends crucially on the radial velocity of the filaments, i.e. on the time the filaments have to lose energy by parallel transport before reaching the plasma facing components. Available models give different predictions with respect to the velocity scaling, in particular the dependency on filament size: The sheath damped model predicts parallel currents in the filaments and a damping of large scale structures, saying that smaller filaments move faster. The polarization current model does not assume parallel currents and damps small scale structures, saying that larger filaments move faster.

A magnetically driven filament probe has been built for experimental investigations of the filament motion. The probe carries 9 Langmuir pins which allow for highly time resolved measurements of the radial and poloidal/toroidal filament velocities.

The analysis of the radial velocity shows that bigger filaments move faster, the radial velocities being in the range of few km/s. This is in clear contradiction with the sheath damping model, but agrees quite good with the polarization current model, so that one can clearly exclude the first one. This is to some extent bad news, as bigger filaments carry a higher energy content, and – if they move faster and thus have less time to lose their energy by parallel transport – deposit far more heat on the plasma facing components than smaller filaments.

Poloidal rotation velocities have been found to be in the range of up to the pedestal rotation velocity, indicating that the filaments start off with a rotation equal to the plasma edge and then slow down on their way out.

The Langmuir measurements have allowed to measure size and density of filaments, as well as their temporal evolution: Filaments broaden with time due to diffusion and lose particles parallel to the field lines with a rate similar to a free flow of particles along the field line. Extrapolation shows that they are formed with densities close to separatrix densities, indicating that filaments are formed near the separatrix.

With the filament probe, together with a set of 3D magnetic coils on the midplane manipulator, the magnetic signature of ELMs and filaments has also been studied. The

aim was, on the one hand, to study which role filaments play for the magnetic structure, and on the other hand to study if the parallel currents predicted by the sheath damped model could be verified. By means of numerical calculations (based on information on filament velocity and size from the Langmuir measurements), it has been found that the magnetic signal is reproduced by a bi-directional current distribution (which would be in agreement with the sheath damped model), but the required currents exceed the possible filament currents by at least one order of magnitude. Also, no good time correlation between the density signal on the Langmuir measurements and the magnetic signal could be achieved. Instead, it has been found that the magnetic signature is reproduced very well by rotating mode structures in the pedestal region. These mode structures might be remnants of the peeling-ballooning modes, which lead to the splitting-off of filaments.

Infrared thermography measurements have been performed to measure the heat deposition due to filaments and, hence, their energy content. Filament temperatures have been derived and the heat transport mechanisms have been studied. The total energy content of all the filaments during an ELM has been found to be much smaller than the total energy loss per ELM. This might be caused by some incoherent (e.g. diffusive) transport over the separatrix, or by filaments that are still attached to the core plasma in a first stage, and act as a conduit for losses from the core to the scrape-off layer, with the core plasma providing a large reservoir of energy for the filament to tap.

The fraction of energy that is deposited close to the separatrix depends on the time at which the filament detaches from the core plasma: In the initial stage, when the filament is still attached, the deposited energy can exceed the energy content of the filament by far. The filaments are expected to lose most of their energy in the very first period right after their formation, when fast (and thus energetic) particles are lost preferentially. As soon as the filament is detached, it can only deposit its energy content onto remote areas of the divertor or to first wall structures, with bigger filaments leading to higher energy deposition to the wall.

## 8.1 Current View of an ELM Crash

This section will give a brief description of the events during an ELM crash from the present point of view.

Right before the ELM crash, the pedestal parameters are close to the peeling-ballooning stability limit. A peeling-ballooning mode grows – first linearly, then explosively – and leads to the formation of  $>10$  filaments. The magnetic mode decays rapidly after the filament formation, but its remnants can be observed by magnetic coils and rotate poloidally upwards (i.e. in electron drift direction). The filaments are formed as structures of enhanced density and temperature that are equally distributed toroidally around the torus and stretch along the field lines by parallel transport. As the energy content of the filaments is much smaller than the total ELM energy loss, there must be some connection of the filaments to the core plasma, so that the filaments act as a conduit for losses from the core to the scrape-off layer. In the initial phase, the heat transport is high, and the filaments (as well as the edge of the core plasma, which acts as their heat reservoir) cool off rapidly. With decreasing temperature, finite resistivity allows for reconnection of field lines, so that the filament can detach from the core plasma. The filament is polarized due to particle drifts and, with less tight binding to the core plasma, starts to move radially outwards due to  $E \times B$  drift. The radial

motion is damped by the polarization current and gives a constant velocity in the order of few km/s with bigger filaments moving faster than smaller ones. Parallel currents and sheath damping are negligible, so that the sheath damping model does not play a role. The poloidal velocity of the filaments is initially determined by the poloidal rotation of the pedestal, but can decrease substantially during the outwards motion of the filament, resulting in a broad velocity distribution at limiters and probes.

The radially moving filaments lose density and heat by parallel transport. They can only deposit their energy content to the target plates or plasma facing components. Measurements suggest that the filaments broaden with time as they move outwards. Fragmentation of filaments has often been proposed, but has so far not been observed in the experiment.

## 8.2 Outlook

Future work that has to be done to fully reveal the physics behind filaments would be to investigate the correlation between the formation of filaments and the peeling-ballooning framework. An important point for understanding the heat deposition is the detachment process, which should be studied at both ends of the filament, i.e. at the low- and at the high-field side. A correlation of the detachment at the two ends would help to see to which extent filaments act as conduit for losses.

For the extrapolation to ITER and other next step fusion devices, further measurements of filament parameters on other machines are necessary. The extrapolation requires an understanding of what governs the filament size. Numerical calculations have to be extended to take heat flux, radial propagation, finite resistivity, sheath interaction etc. into account. They have to be tested against measurements in various machines and can then be applied to future fusion devices.





## Appendix A

# ASDEX Upgrade

ASDEX Upgrade [102] is the successor of the axial symmetric divertor experiment (ASDEX), which was the first experiment with a magnetic divertor configuration. Divertor plasmas are characterized by the formation of an X-point (typically above and/or below the core plasma), in which the poloidal magnetic field is 0, i.e. the field lines there are essentially toroidal. Particles reach the private flux region in the divertor by collisions, and strong pumping prevents the particles to get back to the core plasma again. The magnetic separation of the plasma-wall-interaction region from the core plasma in a tokamak leads to greatly reduced impurity influx compared to limiter plasmas. The divertor concept was the prerequisite to establish the H-mode regime, which allows for higher fusion power for a given machine size because of the formation of a transport barrier close to the plasma edge.

In ASDEX Upgrade, the divertor concept has been adapted to the requirements of a fusion reactor: the poloidal field coils have to be outside the vacuum vessel, and, enlarged to reactor size, there has to be enough space for the installation of blankets for tritium breeding and heat extraction. The key parameters of ASDEX Upgrade are summarized in table A.1, the sign convention for toroidal magnetic field  $B_{tor}$  and plasma current  $I_p$  is shown in fig. A.1 together with a view into the vacuum vessel.

ASDEX Upgrade serves in particular for the study of plasma-wall interactions under reactor-like SOL conditions and for studies of core plasma behaviour and confinement. The closeness to reactor requirements becomes obvious when comparing the poloidal cross section of ASDEX Upgrade, JET, and ITER, the next generation machine that should demonstrate operation under reactor-like conditions: the three experiments form a step ladder with relative dimensions of AUG : JET : ITER  $\simeq 1 : 2 : 4$  (see fig. A.2). This step ladder allows for a good extrapolation to ITER parameters. With regards to filaments, measurements in machines like ASDEX Upgrade allow for extrapolations to ITER after consensus has been achieved on the nature of filaments and after detailed measurements have been carried out on other experiments as well.

In the last years, ASDEX Upgrade has gradually been converted from a carbon machine into a tungsten machine, i.e. the plasma facing components are now covered with tungsten instead of carbon [103]. The final step in this process has been the installation of a tungsten coated divertor. This has led to a reduction in ELM size, so that very large type-I ELMs (or very low ELM frequencies,  $f_{ELM} < 50$  Hz) could not be achieved any more. This would have been useful, because a low ELM frequency allows for a better separation of ELM events on the magnetic measurements. There are several discharges which could not be analysed because the ELM frequency was so high that

$B_{tor}$ coils	16
$B_{pol}$ coils	12
Major/minor plasma radius	1.65 m/0.5 m = 3.3
Plasma volume/surface	14 m <sup>3</sup> /42 m <sup>2</sup>
Maximum average triangularity	0.5
Maximum plasma current (SN)	1.6 MA
Maximum toroidal field	3.9 T
Maximum OH flux swing	9 Vs
Discharge duration	< 10 s
Discharge sequence	15 – 20 min
Vessel volume/surface	32 m <sup>3</sup> /72 m <sup>2</sup>
Plasma heating	
- ohmic	1 MW
- NBI	2 · 10 MW
- ICRH	8 MW
- ECRH	4 · 0.5 MW

**Table A.1:** Technical data of ASDEX Upgrade [102]

the different ELM events could not be separated any more. It is the authors opinion that large ELMs give fewer filaments (or at least more pronounced filament signals), whereas smaller ELMs give more and smaller filaments, so that the small ELMs led to a more noisy signal. This made it more difficult to analyse the filaments, as many of them could not be separated from the other events during the ELM.

The damage of one of the flywheel generators, which provide the power for ASDEX Upgrade during the plasma pulse, has further tightened the operational space and imposed limitations on magnetic field, plasma current and shaping capabilities in the 2007 experiments.

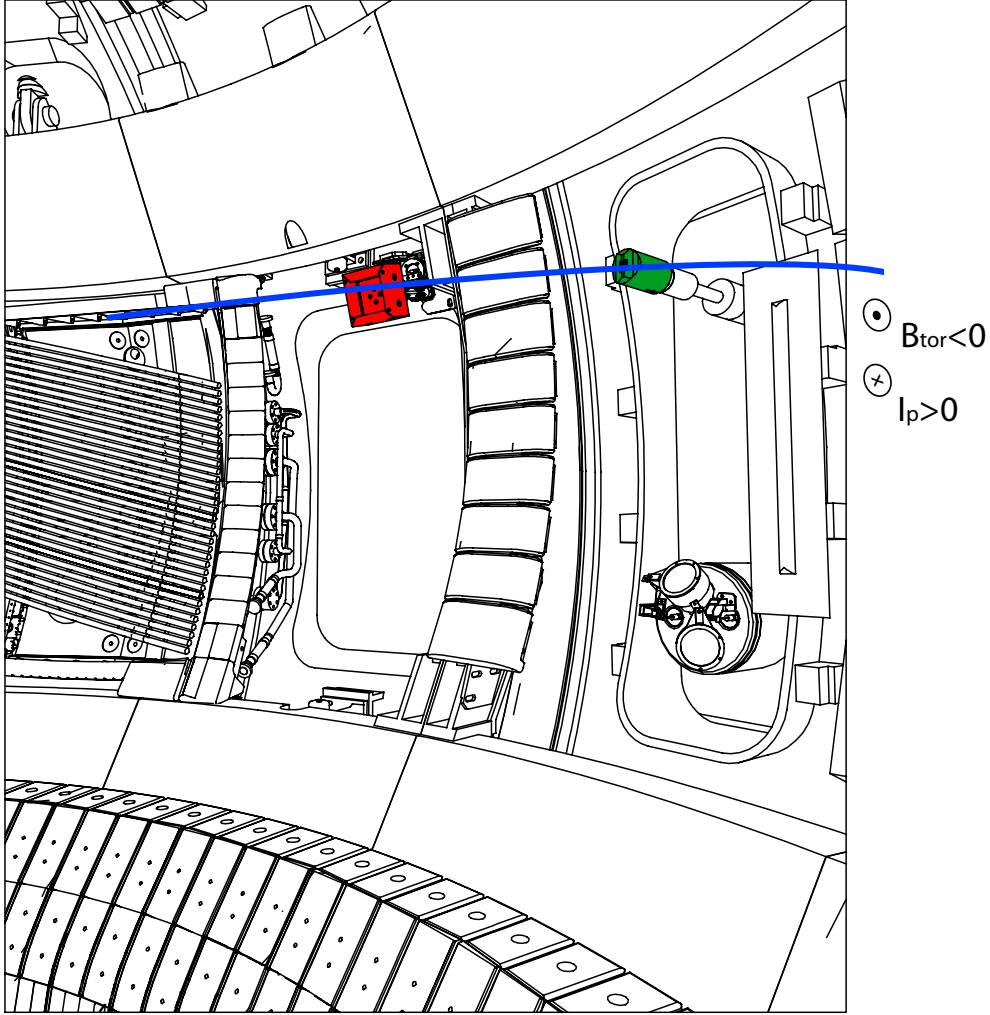


**Figure A.1:** CAD view into the ASDEX Upgrade vessel. For a left hand helicity magnetic field, filament probe and midplane manipulator are connected along a field line. The orientations shown here are for the ASDEX Upgrade standard setup  $B_{tor} < 0$  and  $I_p > 0$ , which means left hand helicity and co-injection. Left hand helicity is obtained for  $\text{sgn}(B_{tor}I_p) < 0$ , and is required for operation of the lower divertor, as the divertor tiles are inclined to the magnetic field to reduce hot edges. The particle drifts (3.1) and (3.2) for the ions point towards the lower divertor in this case.

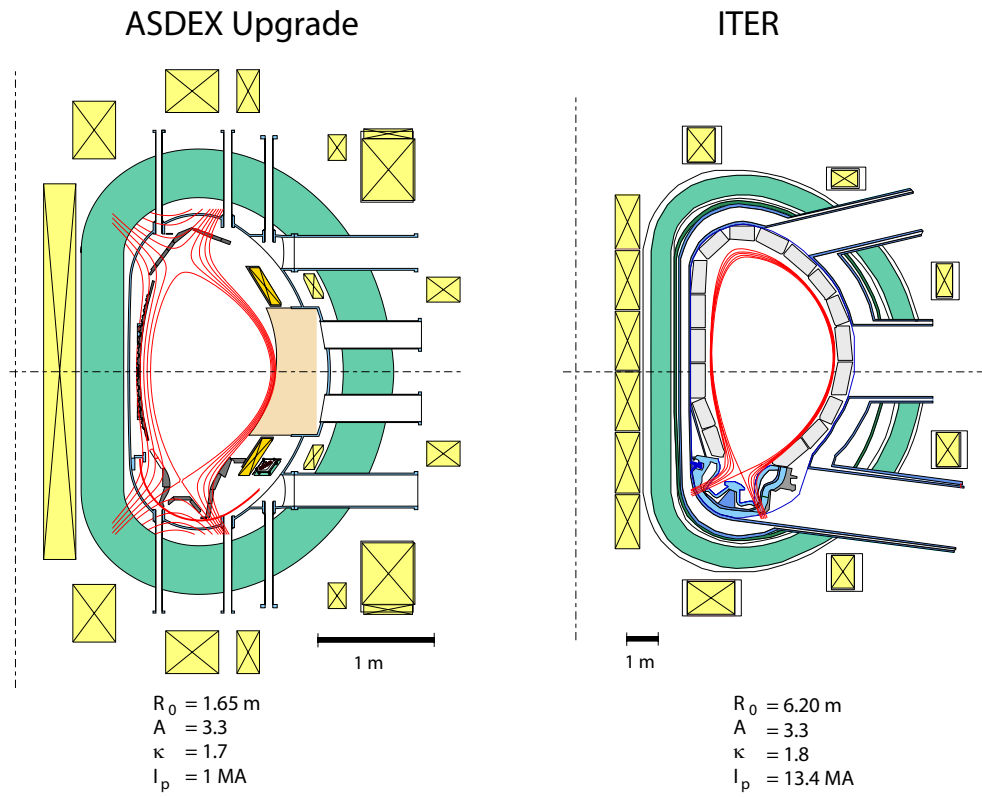


**Figure A.2:** Schematic view of a the poloidal cross section of ASDEX Upgrade and ITER. The plasma shape is comparable and allows for good extrapolations to ITER.

## Appendix B

### MAST

MAST (Mega Ampere Spherical Tokamak) is a spherical tokamak with an aspect ratio  $R/a = 1.38$ , which is achieved by a very thin central column as shown in fig. B.1. The H-mode plasma edge has been widely described in [23, 104], identifying ELMs in

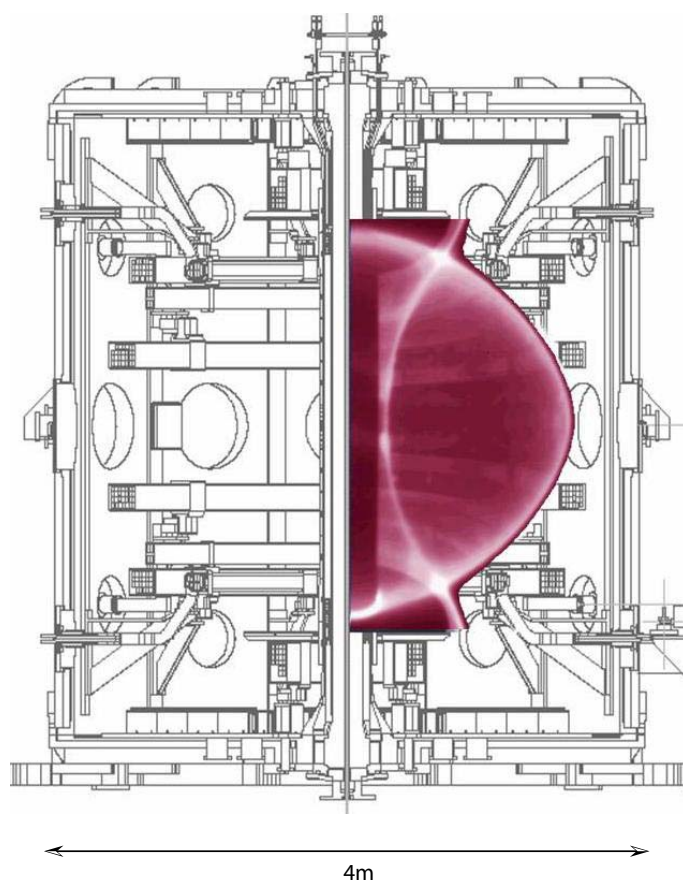


**Figure B.1:** Schematic view of the MAST vessel and a typical MAST plasma configuration. MAST is a spherical tokamak, i.e., it has a large aspect ratio  $a/R$  and a slim central column for the generation of the toroidal magnetic field. A spherical tokamak makes more efficient use of magnetic fields, but has limitations for the energy exhaust due to a smaller surface/volume ratio.

Major/minor plasma radius	0.85 m/0.65 m = 1.31
Maximum plasma current	1.35 MA
Maximum toroidal field (inboard)	1.7 T
Discharge duration	< 1 s
Discharge sequence	15 – 20 min
Plasma heating - NBI	2.9 MW

**Table B.1:** Technical data of the MAST Tokamak

MAST as type-III ELMs and type-I ELMs [105]. MAST is especially suitable for studies of the ELM propagation as its vessel does not follow reactor requirements and has a more cylindric shape, so that there is a distance of up to 50 cm between separatrix and limiters. Therefore, filaments can propagate freely and undisturbed in the MAST vessel and thus could be observed at distances of up to 20 cm from the separatrix.

The large gap allows to use cameras with a large field of view, covering the whole plasma. Even though spherical tokamaks offer good insight in edge physics, they do not seem to be ideally suited for a fusion reactor, as they have a reduced wetted area and may not be capable to withstand ELMs in reactor conditions.

The common operating mode for MAST is the disconnected double-null (DDN) in which the two X-points lie on different flux surfaces with the gap between these flux surfaces being of the order of the ion gyroradius.

# Appendix C

## Sheath Physics

### C.1 Floating Walls

Plasma sheaths form where plasma interacts with solid state material [65]. The basic principle behind sheath formation is the quasi-neutrality of a plasma: electrons have a higher mobility than the heavier ions,

$$\mu_e = \frac{e}{m_e v_e} \gg \mu_i = \frac{e}{m_i v_i}, \quad (\text{C.1})$$

so that electrons tend to leave a plasma surface ahead of the ions, charging the wall negatively. This leads to an electron repelling potential between plasma and surface that slows the electron loss rate and increases the ion loss rate. Eventually, the loss rates become equal and an ambipolar flow of electrons and ions is achieved:

$$\Gamma_w^e = \Gamma_w^i. \quad (\text{C.2})$$

In this state, the wall has a negative electric potential  $V_w \simeq -3kT_e/e$ , whereas the plasma edge has a so-called Debye sheath with a net positive charge. The ambipolar flow is achieved by an acceleration of the ions by the electrons. At the wall, both species have a fluid speed equal to the ion sound speed

$$c_s = \sqrt{\frac{k(T_e + \gamma T_i)}{m_i}} \quad (\text{C.3})$$

with the adiabatic coefficient  $\gamma$ . The Debye sheath has an extent in the order of the Debye length

$$\lambda_D = \sqrt{\frac{\epsilon_0 k T_e}{n_e e^2}}. \quad (\text{C.4})$$

The Debye length for typical SOL values ( $T_e = 20 \text{ eV}$ ,  $n_e = 10^{19} \text{ m}^{-3}$ ) is in the order of  $10^{-5} \text{ m}$ , meaning that the sheath is extremely thin.

The Debye sheath shields the plasma inside the sheath from the negative wall potential. This shielding is, however, not perfect and leaves a potential of about  $0.7kT_e/e$  and, consequently, an adjacent pre-sheath with an extent in the order of  $10\lambda_D$ .

The left hand side of fig. C.1 shows a plasma flux tube that is aligned parallel to the magnetic field and connected to walls on both sides. The same geometry applies to filaments as well, as these are also field aligned structures.

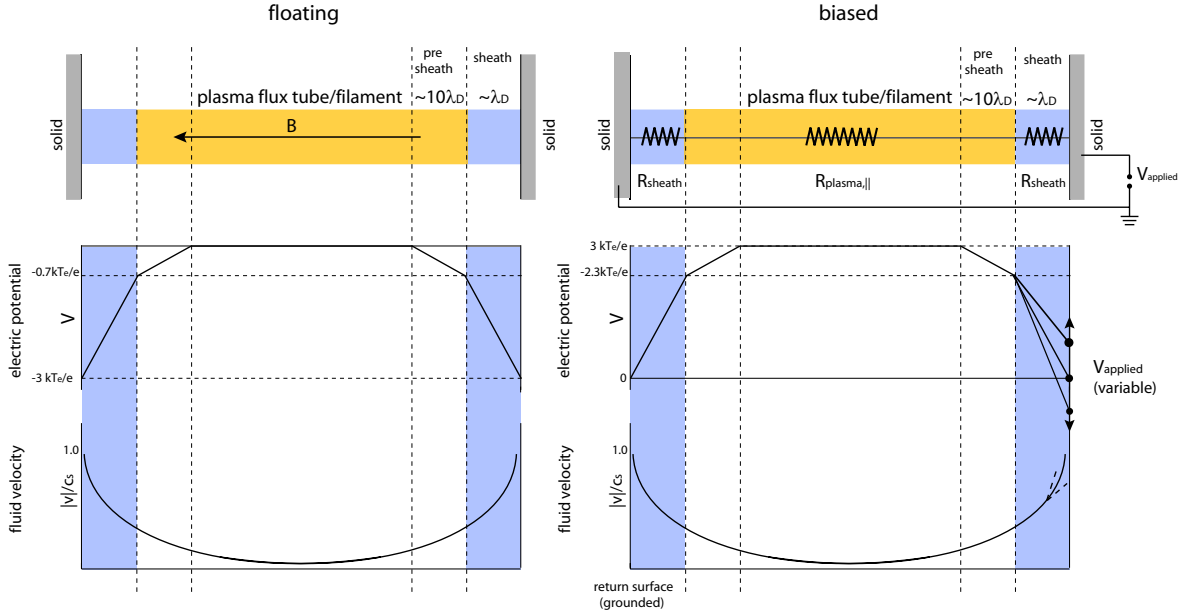


**Figure C.1:** Formation of sheaths at walls. Quasi-neutrality leads to an electron repelling potential of  $3kT_e/e$  at the wall and the formation of thin sheaths ( $\lambda_D \simeq 10^{-5}$  m), in which the ions are accelerated to ion sound speed. The sheath screens most of the wall potential, even if an external potential is applied to the wall (right part). An external potential thus changes only the electron flow, not the ion flow.

## C.2 Biased Walls

In the case, where an external voltage is applied to the wall (e.g. for Langmuir probe measurements),  $\Gamma_w^i = n_{se}c_s$  with the density at the sheath edge,  $n_{se}$ , still holds. The change in potential is entirely taken up by the (now different) voltage drop in the sheath, whereas the pre-sheath still has a voltage drop of  $0.7kT_e/e$  (see right half of fig. C.1). The voltage drop changes the particle flow to the wall, i.e. relation (C.2) is no more valid. Instead, we have

$$\Gamma_w^e \neq \Gamma_w^i \quad (\text{C.5})$$

with  $\Gamma_w^i$  equal to the floating case, and with  $\Gamma_w^e$  determined by the applied voltage. The difference between the two fluxes gives a net current through wall or probe, respectively:

$$I_{\parallel}(\phi) = \frac{A_1 + A_2}{2} j_{i,sat} \left[ \tanh\left(\frac{e\phi}{kT_e} - 0.5 \ln \frac{A_1}{A_2}\right) - \frac{A_1 - A_2}{A_1 + A_2} \right] \quad (\text{C.6})$$

$$= A j_{i,sat} \tanh \frac{e\phi}{2kT_e}, \quad (\text{C.7})$$

with  $A = A_1 = A_2$  for identical probe size or constant flux tube width. The ion saturation current

$$I_{\parallel,sat} = A j_{i,sat} = A \Gamma_w^i = A n_{se} c_s \quad (\text{C.8})$$

is reached at high negative potential, where all electrons are repelled, so that only the ions reach the probe surface. According to eq. (C.7) and fig. 3.3, the ion saturation can be reached to about 76% for voltages in the order of  $2kT$ . The required voltage thus depends on the temperatures of the impinging particles. Temperatures in the order of



30 – 60 eV thus require a voltage of about 60 – 120 V, for example. Higher voltages, however, lead to arcing and, consequently, to high wear of the probe pins or even destruction of the pins.

The ratio  $d\phi/dI$  gives the sheath resistivity, which is used in sec. 3.1 to calculate the polarization current in a filament.

We will now try to estimate the time until a plasma sheath forms: With a thermal electron velocity  $v_e \approx \sqrt{kT_e/m_e}$  and typical SOL parameters ( $T_e = 20$  eV,  $n_e = 10^{19} \text{ m}^{-3}$ ), the electrons take about  $5 \cdot 10^{-12}$  s to travel through the Debeye sheath. The sheath is fully established, when ions reach the wall. For a rough estimate, we assume  $T_e \approx T_i$  and neglect any acceleration by the electrons, resulting in a travel time of about 0.2 ns. Even if we include the pre-sheath in our treatment, the time to establish the full sheath is in the nanosecond range and as such much faster than the filament motion. Therefore, even when working with moving density blobs, we do not expect substantial deviations from standard Langmuir theory.



# Bibliography

- [1] Intergovernmental Panel on Climate Change. Contribution of working group i to the fourth assessment report of the intergovernmental panel on climate change, 2007. <http://www.ipcc.ch>.
- [2] P. H. Rebut. From jet to the reactor. 48(12B):B1–B13, 2006.
- [3] S. Atzeni and J. Meyer-ter Vehn. *The physics of inertial fusion*. Clarendon Press, 2004.
- [4] J. A. Wesson. *Tokamaks*. Clarendon Press, third edition, 2004.
- [5] J. P. Freidberg. *Ideal magnetohydrodynamics*. Plenum Press, 1987.
- [6] F. Wagner, et al. Regime of improved confinement and high beta in neutral-beam-heated divertor discharges of the ASDEX tokamak. 49(19):1408–1412, 1982.
- [7] F. Wagner. A quarter century of h-mode studies. 49(12), 2007.
- [8] H. Zohm. The physics of edge localized modes (ELMs) and their role in power and particle exhaust. 38(8):1213–1223, 1996.
- [9] H. Zohm. Edge Localized Modes (ELMs). 38(2):105–128, 1996.
- [10] W. Suttrop. The physics of large and small edge localized modes. 42(5A):A1–A14, 2000.
- [11] *H-mode threshold power dependences in ITPA threshold database*, 2004. 20th IAEA Fusion Energy Conference, Vilamoura, Portugal, November 2004.
- [12] T. Kass, S. Günter, M. Maraschek, W. Suttrop, H. Zohm, and the ASDEX Upgrade Team. Characteristics of type-i and type-iii ELM precursors in ASDEX Upgrade. 38(1):111–116, 1998.
- [13] A. Herrmann. Overview on stationary and transient divertor heat loads. 44(6):883–904, 2002.
- [14] A. Herrmann, T. Eich, S. Jachmich, M. Laux, P. Andrew, A. Bergmann, A. Loarte, G. Matthews, J. Neuhauser, the ASDEX Upgrade Team, and Contributors to EFDA-JET work Programme. Stationary and transient divertor heat flux profiles and extrapolation to iter. 313–316:759–767, 2003.
- [15] G. M. Fishpool. Loss of confinement due to reduction of the edge pedestal in jet. 38(9):1373–1380, 1998.

- [16] A. Loarte, M. Becoulet, G. Saibene, R. Sartori, D.J. Campbell, T. Eich, A. Herrmann, M. Laux, W. Suttrop, B. Alper, P.J. Lomas, G. Matthews, S. Jachmich, J. Ongena, P. Innocente, and EFDA-JET Workprogramme Collaborators. Characteristics and scaling of energy and particle losses during type i elms in jet h-modes. 44(9):1815–1844, 2002.
- [17] A. Loarte, G. Saibene, R. Sartori, M. Becoulet, L. Horton, T. Eich, A. Herrmann, M. Laux, G. Matthews, S. Jachmich, N. Asakura, A. Chankin, A. Leonard, G. Porter, G. Federici, M. Shimada, M. Sugihara, and G. Janeschitz. Elm energy and particle losses and their extrapolation to burning plasma experiments. 313–316:962–966, 2003.
- [18] M. Becoulet, et al. Edge localized modes control: experiment and theory. 337–339:677–683, 2005.
- [19] J. Neuhauser. Private communication, 1 2007.
- [20] T. Eich, A. Herrmann, J. Neuhauser, R. Dux, J. C. Fuchs, S. Günter, L. D. Horton, A. Kallenbach, P. T. Lang, C. F. Maggi, M. Maraschek, V. Rohde, W. Schneider, and the ASDEX Upgrade Team. Type-i ELM substructure on the divertor target plates in ASDEX Upgrade. 47(6):815–842, 2005.
- [21] M. Bécoulet, et al. Edge localized mode physics and operational aspects in tokamaks. 45(12A):A93–A113, 2003.
- [22] J. Neuhauser, et al. Transport into and across the scrape-off layer in the ASDEX Upgrade divertor tokamak. 44(6):855–870, 2002.
- [23] G. Counsell, A. Kirk, J-W Ahn, and Y. Yang. Boundary plasma and divertor phenomena in MAST. 44(6):827–843, 2002.
- [24] T. Eich, A. Herrmann, G. Pautasso, P. Andrew, N. Asakura, J. A. Boedo, Y. Corre, M. E. Fenstermacher, J. C. Fuchs, W. Fundamenski, G. Federici, E. Gauthier, B. Goncalves, O. Gruber, A. Kirk, A. W. Leonard, A. Loarte, G. F. Matthews, J. Neuhauser, R. A. Pitts, V. Riccardo, and C. Silva. Power deposition onto plasma facing components in poloidal divertor tokamaks during type-i ELMS and disruptions. 337–339:669–676, 2005.
- [25] T. Eich, A. Herrmann, P. Andrew, A. Loarte, and Contributors to the EFDA-JET Program. Power deposition measurements in deuterium and helium discharges in jet mkiigb divertor by ir-thermography. 313–316:919–924, 2003.
- [26] G. Federici, P. Andrew, P. Barabaschi, J. Brooks, R. Doerner, A. Geier, A. Herrmann, G. Janeschitz, K. Krieger, A. Kukushkin, A. Loarte, R. Neu, G. Saibene, M. Shimada, G. Strohmayer, and M. Sugihara. Key iter plasma edge and plasma-material interaction issues. 313–316:11–22, 2003.
- [27] A. Herrmann, T. Eich, V. Rohde, C. J. Fuchs, J. Neuhauser, and the ASDEX Upgrade Team. Power deposition outside the divertor in ASDEX Upgrade. 46(6):971–980, 2004.

- [28] A. Herrmann, J. Neuhauser, G. Pautasso, V. Bobkov, R. Dux, T. Eich, C. J. Fuchs, O. Gruber, C. Maggi, H. W. Müller, V. Rohde, M. Y. Ye, and the ASDEX Upgrade Team. Wall and divertor load during elmy h-mode and disruptions in ASDEX Upgrade. In *20th IAEA Fusion Energy Conference, Vilamoura, Portugal, November 2004*, volume IAEA-CSP-25/CD, pages IAEA-CN-116/EX/2-4Rb, 2005.
- [29] A. Herrmann, J. Neuhauser, V. Rohde, R. Dux, T. Eich, C. J. Fuchs, M. Y. Ye, and the ASDEX Upgrade Team. Interaction of elms and fast particles with in-vessel components in ASDEX upgrade. 337-339:697-701, 2005.
- [30] A. Kirk, T. Eich, A. Herrmann, H. W. Müller, L. D. Horton, G. F. Counsell, M. Price, V. Rohde, V. Bobkov, B. Kurzan, J. Neuhauser, H. Wilson, and the ASDEX Upgrade and MAST Teams. The spatial structure of type-i elms at the mid-plane in asdex upgrade and a comparison with data from mast. 47(7):995-1013, 2005.
- [31] A. Kirk, H. R. Wilson, R. Akers, N. J. Conway, G. F. Counsell, S. C. Cowley, J. Dowling, B. Dudson, A. Field, F. Lott, B. Lloyd, R. Martin, H. Meyer, M. Price, D. Taylor, M. Walsh, and the MAST Team. Structure of elms in mast and the implications for energy deposition. 47(2):315-333, 2005.
- [32] B. Kurzan, H. D. Murmann, J. Neuhauser, and the ASDEX Upgrade Team. Fine structure of type-i edge-localized modes in the steep gradient region. 95(14):145001-1, 2005.
- [33] M. Endler, I. García-Cortés, C. Hidalgo, G. F. Matthews, and the ASDEX Team and Jet Team. The fine structure of elms in the scrape-off layer. 47(2):219-240, 2005.
- [34] A. Kirk, G. F. Counsell, H. R. Wilson, J-W Ahn, R. Akers, E. R. Arends, J. Dowling, R. Martin, H. Meyer, M. Hole, M. Price, P. B. Snyder, D. Taylor, M. J. Walsh, Y. Yang, and the MAST Team. Elm characteristics in MAST. 46(3):551-572, 2004.
- [35] A. Kirk, H. R. Wilson, G. F. Counsell, R. Akers, E. Arends, S. C. Cowley, J. Dowling, B. Lloyd, M. Price, M. Walsh, and the MAST Team. Spatial and temporal structure of edge-localized modes. 92(24):245002, 2004.
- [36] W. Fundamenski, W. Sailer, and JET EFDA contributors. Radial propagation of type-i elms on jet. 46(1):233-259, 2004.
- [37] W. Fundamenski, R.A. Pitts, and JET EFDA contributors. A model of elm filament energy evolution due to parallel losses. 48(1):109-156, 2006.
- [38] S.J. Zweben, J.A. Boedo, O. Grulke, C. Hidalgo, B. LaBombard, R.J. Maqueda, P. Scarin, and J.L. Terry. Edge turbulence measurements in toroidal fusion devices. 49(7):S1-S23, 2007.
- [39] N. Ben Ayed, B. Dudson, A. Kirk, R.G.L. Vann, H.R. Wilson, and the MAST team. Structure and motion of inter-elm filaments in mast. In *34th EPS Conference on Plasma Physics, Warsaw, Poland, July 2007*, 2007.

- [40] A. Schmid. Charakterisierung von plasmafluktuationen mit einer kombinierten mirnov-langmuir-sonde am tokamak asdex upgrade. Diplomarbeit, TU München, 2005.
- [41] A. Kirk, B. Koch, R. Scannell, H. R. Wilson, G. F. Counsell, J. Dowling, A. Herrmann, R. Martin, M. Walsch, and the MAST Team. Evolution of filament structures during edge-localized modes in the mast tokamak. 96(18):185001, 2006.
- [42] A. Kirk, N. Ben Ayed, G. Counsell, B. Dudson, T. Eich, A. Herrmann, B. Koch, R. Martin, A. Meakins, S. Saarelms, R. Scannell, S. Tallents, M. Walsh, H. R. Wilson, and the MAST Team. Filament structures at the plasma edge on MAST. 48(12B):B433–B441, 2006.
- [43] P.B. Snyder, K.H. Burrell, H.R. Wilson, M.S. Chu, M.E. Fenstermacher, A.W. Leonard, R.A. Moyer, T.H. Osborne, M. Umansky, W.P. West, and X.Q. Xu. Stability and dynamics of the edge pedestal in the low collisionality regime: physics mechanisms for steady-state elm-free operation. 47(8):961–968, 2007.
- [44] G.T.A. Huysmans. Elms: Mhd instabilities at the transport barrier. 47(12B):B165–178, 2005.
- [45] S. Günter. Einführung in die plasmaphysik. Vorlesungsskript, TU München.
- [46] H.R. Wilson and R.L. Miller. Access to second stability region for coupled peeling-ballooning modes in tokamaks. *Phys. Plasmas*, 6(3):873–876, 1999.
- [47] H.R. Wilson, J.W. Connor, A.R. Field, S.J. Fielding, R.L. Miller, L.L. Lao, J.R. Ferron, and A.D. Turnbull. Ideal magnetohydrodynamic stability of the tokamak high-confinement-mode edge region. *Phys. Plasmas*, 6(5):1925–1934, 1999.
- [48] ELITE edge plasma stability code. <http://fusion.gat.com/THEORY/elite/>.
- [49] G.T.A. Huysmans, S.E. Sharapov, A.B. Mikhailovskii, and W. Kerner. Modeling of diamagnetic stabilization of ideal magnetohydrodynamic instabilities associated with the transport barrier. *Phys. Plasmas*, 8(10):4292–4305, 2001.
- [50] S. Saarelma, S. Günter, T. Kurki-Suono, and H. P. Zehrfeld. Elm phenomenon as an interaction between bootstrap-current driven peeling modes and pressure-driven ballooning modes. 42(5A):A139–A145, 2000.
- [51] P.B. Snyder, H. R. Wildon, J.R. Ferron, L.L. Lao, A.W. Leonard, D. Mossessian, M. Murakami, T.H. Osborne, A.D. Turnbull, and X.Q. Xu. Elms and constraints on the h-mode pedestal: peeling-ballooning stability calculation and comparison with experiment. 44(2):320–328, 2004.
- [52] S.C. Cowley, H. Wilsown, O. Hurricane, and B. Fong. Explosive instabilities: from solar flares to edge localized modes in tokamaks. 45(12A):A31–38, 2003.
- [53] H. R. Wilson and S. C. Cowley. Theory for explosive ideal magnetohydrodynamic instabilities in plasmas. 92(17):175006–1, 2004.
- [54] W. Fundamenski, V. Naulin, T. Neukirch, O.E. Garcia, and J. Juul Rasmussen. On the relationship between elm filaments and solar flares. 49(5):R43–86, 2007.

- [55] G.T.A. Huysmans. External kink (peeling) modes in x-point geometry. 47(12):2107–2121, 2005.
- [56] X.Q. Xu and R.H. Cohen. Scrape-off layer turbulence theory and simulations. 38(1-2):158–170, 1998.
- [57] X.Q. Xu, R.H. Cohen, W.M. Nevins, G.D. Porter, M.E. Rensink, T.D. Rognlien, J.R. Myra, D.A. D'Ippolito, R.A. Moyer, P.B. Snyder, and T.N. Carlstrom. Turbulence simulations of x point physics in the l-h transition. 42(1):21–27, 2002.
- [58] P.B. Snyder, H.R. Wilson, and X.Q. Xu. Progress in the peeling-ballooning model of edge localized modes: Numerical studies of nonlinear dynamics. 12(5):056115, 2005.
- [59] H.R. Wilson, S.C. Cowley, a. Kirk, and P.B. Snyder. Magneto-hydrodynamic stability of the h-mode transport barrier as a model for edge localized modes: an overview. 48(5A):A71–A84, 2006.
- [60] B.D. Scott. Free-energy conservation in local gyrofluid models. *Phys. Plasmas*, page 102307, 2005.
- [61] B.D. Scott. Studies of the tokamak edge with self consistent turbulence, equilibrium, and flows. 2006. IAEA Fusion Energy Conference, Chengu, China, October 2006.
- [62] O.E. Garcia, N.H. Bian, and W. Fundamenski. Radial interchange motions of plasma filaments. 13(8):082309, 2006.
- [63] V. Rozhansky, I. Veselova, and S. Voskoboynikov. Evolution and stratification of a plasma cloud surrounding a pellet. 37(4):399–414, 1995.
- [64] V. Rozhansky, I. Senichenkov, I. Veselova, and R. Schneider. Mass deposition after pellet injection into a tokamak. 46(4):575–591, 2004.
- [65] P. C. Stangeby. *The plasma boundary of magnetic fusion devices*. Institute of Physics Publishing, 2000.
- [66] R. Schneider. Plasma edge physics for tokamaks. Technical Report 12/1, IPP, Garching, Germany, February 2001.
- [67] M. Weinlich and A. Carlson. Flush mounted langmuir probes in an oblique magnetic field. *Phys. Plasmas*, 4(6):2151–2160, 1997.
- [68] A. Herrmann, A. Kirk, A. Schmid, B. Koch, M. Laux, M. Maraschek, H. W. Müller, J. Neuhauser, V. Rohde, E. Wolfrum, and the ASDEX Upgrade Team. The filamentary structure of elms in the scrape-off layer in asdex upgrade. 363-365:528–533, 2007.
- [69] H. W. Müller, K. Büchl, M. Kaufmann, P. T. Lang, R. S. Lang, A. Lorenz, M. Maraschek, V. Mertens, J. Neuhauser, and the ASDEX Upgrade Team. High  $\beta$  plasmoid drift during pellet injection into tokamaks. 83(11):2199–2202, 1999.
- [70] R. H. Cohen and D. D. Ryutov. Dynamics of an isolated blob in the presence of the x-point. 46(7-9):678–684, 2006.

- [71] V. Rozhanski and A. Kirk. Possible mechanism for filament motion in the sol of a tokamak. In *34th EPS Conference on Plasma Physics, Warsaw, Poland, July 2007*, 2007.
- [72] S. I. Krasheninnikov. On scrape off layer transport. *Physics Letters A*, 283:368–370, 2001.
- [73] D. A. D’Ippolito, J. R. Myra, and S. I. Krasheninnikov. Cross-field blob transport in tokamak scrape-off-layer plasmas. 9(1):222–233, 2002.
- [74] D. A. D’Ippolito and J. R. Myra. Blob stability and transport in the scrape-off-layer. 10(10):4029–4039, 2003.
- [75] G. Q. Yu and S. I. Krasheninnikov. Dynamics of blobs in scrape-off-layer/shadow regions of tokamaks and linear devices. 10(11):4413–4418, 2003.
- [76] D. A. D’Ippolito, J. R. Myra, S. I. Krasheninnikov, G. Q. Yu, and A. Yu. Pigarov. Blob transport in the tokamak scrape-off-layer. 44(1–3):205–216, 2004.
- [77] O.E. Garcia, N.H. Bian, V. Naulin, A. H. Nielsen, and J. Juul Rasmussen. Mechanism for scaling of convection of isolated structures in nonuniformly magnetized plasmas. 12(9):090701, 2005.
- [78] Andreas Schmid, Albrecht Herrmann, Volker Rohde, Marc Maraschek, H. W. Müller, and the ASDEX Upgrade Team. Magnetically driven filament probe. 78(5):053502, 2007.
- [79] J. Gernhardt. Magnetic diagnostic on ASDEX Upgrade with internal and external pick-up coils. Technical Report 1/262, IPP, Garching, Germany, November 1992.
- [80] D. Desideri, G. Serianni, V. Antoni, M. Bagatin, C. S. Pitcher, and L. Tramontin. A fast moving diagnostic system on the rfx experiment. 70(1):403–406, 1999.
- [81] A. Carlson, V. Rohde, M. Weinlich, and the ASDEX Upgrade Team. The separation of angle and size effects on langmuir characteristics. 241–243:722–727, 1997.
- [82] R. Neu, Ch. Hopf, A. Kallenbach, T. P"utterich, R. Dux, H. Greuner, O. gruber, A. Herrmann, K. Krieger, H. Maier, V. Rohde, and the ASDEX Upgrade Team. Operational conditions in a w-clad tokamak. 367-370(2):1497–1502, 2007.
- [83] R. Neu and the ASDEX Upgrade Team. Plasma wall interaction and its implication in an all tungsten divertor tokamak. 49(12B):B59–B70, 2007.
- [84] H. W. Müller, V. Bobkov, A. Herrmann, M. Maraschek, J. Neuhauser, V. Rohde, A. Schmid, M. Tsalias, and the ASDEX Upgrade Team. Deuterium plasma flow in the scrape-off layer of ASDEX upgrade. 363-365:605–610, 2006.
- [85] A. Herrmann, W. Junker, K. Günther, S. Bosch, M. Kaufmann, J. Neuhauser, G. Pautasso, Th. Richter, R. Schneider, and the ASDEX Upgrade Team. Energy flux to the ASDEX Upgrade divertor plates determined by thermography and calorimetry. 37(1):17–29, 1995.



- [86] A. Herrmann and the ASDEX Upgrade Team. Limitations for divertor heat flux calculations of fast events in tokamaks. In *28th EPS Conference on Plasma Physics, Madeira, Portugal, June 2001*, volume 25A, pages 2109–2112, 2001.
- [87] A. Kirk, G. F. Counsell, G. Cunningham, J. Dowling, M. Dunstan, H. Meyer, M. Price, S. Saarelma, R. Scannell, M. Walsh, H. R. Wilson, and the MAST Team. Evolution of the pedestal on mast and the implications for elm power loadings. 49(8):1259–1275, 2007.
- [88] T. Pütterich. Private communication, to be published, 09 2007.
- [89] T. Bolzonella, H. Zohm, M. Maraschek, E. Martines, S. Saarelma, S. Günter, and the ASDEX Upgrade Team. High frequency mhd activity related to type i elms in asdex upgrade. 46(5A):A143–A149, 2004.
- [90] M. Maraschek, S. Günter, T. Kass, S. Saarelma, H. P. Zehrfeld, H. Zohm, and the ASDEX Upgrade Team. MHD characteristics of ELMs and their precursors. In *25th EPS Conference on Plasma Physics, Praha, Czech republic, June 1998*, volume 22C, pages 492–495, 1998.
- [91] H. Reimerdes, A. Pochelon, and W. Suttrop. Toroidally asymmetric elm precursors in tcv. 38(3):319–323, 1998.
- [92] S.J. Fielding, J. D. Ashall, p. D. Carolan, A. Colton, D. Gates, J. Hugill, A. W. Morris, M. Valovic, and the COMPASS and ECRH Teams. The h-mode in compass-d. 38(8):1091–1102, 1996.
- [93] H. Zohm. Untersuchung magnetischer moden am tokamak asdex. Dissertation, Universität Heidelberg, 1990.
- [94] M. Schittenhelm and H. Zohm. Analysis of coupled mhd modes with mirnov probes in asdex upgrade. 37(9):1255–1270, 1997.
- [95] M. Reich. Private communication, 09 2007.
- [96] J. Neuhauser, V. Bobkov, G.D. Conway, R. Dux, T. Eich, M. Garcia-Munoz, A. Herrmann, L. D. Hortyon, A. Kallenbach, S. Kalvin, G. Kocsis, B. Kurzan, P. Lang, M. Maraschek, H.W. Müller, H. D. Murmann, R. Neu, A.G. Peeters, M. Reich, V. Rohde, A. Schmid, W. Suttrop, M. Tsalas, E. Wolfrum, and the ASDEX Upgrade Team. Structure and dynamics of spontaneous and induced elms on asdex upgrade. 2007.
- [97] R.L. Petry. Secondary electron emission from tungsten, copper and gold. *Physical Review*, 28:362–366, 1926.
- [98] J.M. Pedgley, G.M. McCracken, H. Farhang, and B.H. Blott. Measurements of secondary electron emission for fusion related materials. 196-198:1053–1058, 1992.
- [99] A. Bergmann. Transport of edge-localized mode energy in a scrape-off layer in the presence of collisionless fast electrons. 42(9):1162–1167, 2002.
- [100] M. Laux. How to interpret triple probe measurements when none of the tips saturates. 44(7–8):695–699, 2004.

- [101] A. Kirk. Private communication, 10 2007.
- [102] ASDEX Upgrade Team. Special issue on asdex upgrade. *Fusion Science and Technology*, 44(3), 2003.
- [103] R. Neu, V. Bobkov, R. Dux, A. Kallenbach, T. P"utterich, H. Greuner, O. Gruber, A. Herrmann, C. Hopf, K. Krieger, C.F. Maggi, H. Maier, M. Mayer, V. Rohde, K. Schmid, W. Suttrop, and the ASDEX Upgrade Team. Final steps to an all tungsten divertor tokamak. 363-365:52–59, 2007.
- [104] A. Kirk, G.F. Counsell, E. Arends, H. Meyer, D. Taylor, M. Valovic, M. Walsh, H. Wilson, and the MAST team. H-mode pedestal characteristics on MAST. 46(5A):A187–A194, 2004.
- [105] A. Kirk. Private communication, 02 2007.

# Acknowledgements

An dieser Stelle möchte ich mich beim gesamten ASDEX Upgrade Team herzlich für die gute Zusammenarbeit bedanken. Insbesondere möchte ich mich bedanken bei

- Frau Prof. Dr. Sibylle Günter für die Gelegenheit, am Max-Planck-Institut für Plasmaphysik und der TU München meine Doktorarbeit anfertigen zu dürfen.
- Herrn Dr. Albrecht Herrmann für die ausgezeichnete Betreuung während der Doktorarbeit
- Herrn Dr. Josef Neuhauser für die zahlreichen Diskussionen, die mir für das Verständnis der Physik der Filamente sowie vielen weiteren Punkten der Plasmaphysik von unschätzbarem Wert waren.
- Herrn Dr. Hans Werner Müller für seine Hilfen zum Betrieb der Langmuirsonden und des Mittelebenenmanipulators, sowie für die Bereitstellung seiner Kepco-Spannungsquellen während meiner Messungen.
- Herrn Dr. Marc Maraschek für seine Hilfen zur Magnetik und bei der Verkabelung der Hotlink-ADCs.
- Herrn Horst-Bodo Schilling für seine Arbeit an der Langmuir-Elektronik.
- Herrn Hans Scholz und Herrn Peter Leitenstern für Konstruktion, Aufbau und Wartung der Filamentsonde, sowie Herrn Stefan Eder für seine Unterstützung beim Aufbau der Thermografiekameras.
- Herrn Helmut Blank, der die Timersteuerung für die Filamentsonde programmiert und die Anbindung an das Schussfilesystem durchgeführt hat.
- Herrn Dr. Andrew Kirk (UKAEA, Culham Science Centre, Abingdon) für die gute Zusammenarbeit an ASDEX Upgrade und die Gelegenheit, Experimente an MAST durchführen zu dürfen.
- Besonderer Dank gebührt meiner Promotionskollegin Frau Carolin Tröster, MA, sowie meinem Promotionskollegen Herrn Dr. Dr. Timo Kubach.